Means and Variability of Some Aspects of the Hydrological Cycle

by

Cecelia DeLuca

Submitted to the Department of Earth, Atmospheric and Planetary Sciences
in partial fulfillment of the requirements for the degree of

Master of Science in Meteorology

at the

MASSACHUSETTS INSTITUTE OF TECHNOLOGY

August 1996
[September 1996]

Author .....
Department of Earth, Atmospheric and Planetary Sciences
August 31, 1996

Certified by .....
Peter H. Stone
Professor
Thesis Supervisor

Accepted by .....
Thomas H. Jordan
Department Head

Means and Variability of Some Aspects of the Hydrological Cycle

by

Cecelia DeLuca

Submitted to the Department of Earth, Atmospheric and Planetary Sciences
on August 31, 1996, in partial fulfillment of the
requirements for the degree of
Master of Science in Meteorology

Abstract

Means and interannual variability of moisture flux divergence and precipitable water are calculated for the years 1965 through 1989 from a GFDL global atmospheric dataset. An empirical orthogonal function (EOF) analysis assesses portions of the variability due to long-term trends, the effect of the El Nino Southern Oscillation, and other factors. Apparent long term trends are discussed in light of the deficiencies of the dataset, other studies, and statistical significance tests. Little conclusive evidence that the trends reflect physical phenomena is found, with a convergent trend in northern high-latitudes a possible exception. In the latter part of the thesis, the monthly-mean moisture flux divergence is equated with runoff and is used to drive a GISS river model, which routes moisture collected on land to oceans. Based on the results of the model and divergence data over land and ocean regions, the annual mean and interannual variability of the freshwater flux into the Atlantic is computed for 4° latitude strips and for the northern, mid- and southern Atlantic. For the northern Atlantic, mean fluxes are in good agreement with models and observational studies. For the mid- and southern Atlantic there are inconsistencies between this and other studies that reflect the scarcity of radiosonde data over tropical oceans and the southern hemisphere. A possible application of the computed fluxes and their variances is the validation and forcing of atmosphere, ocean or coupled models. This may be feasible with the results obtained for high northern latitudes, but is not likely to yield meaningful results south of about 40° N.

Included in an appendix is a catalogue of graphical statistics, with seasonal and annual means, interannual variability (including EOF analyses), and zonal means of a number of hydrological fields, including moisture fluxes.

Thesis Supervisor: Peter H. Stone
Title: Professor

Acknowledgments

Thanks to Drs. Rick Rosen and Dara Entekahbi for their comments and guidance. Special thanks to my advisor, Dr. Peter Stone, for his patience and unflagging enthusiasm.

Contents

List of Appendices

Chapter 1

Overview

The hydrological cycle impacts climate in a number of critical ways. Atmospheric water vapor is the principle greenhouse gas, and water vapor feedback sensitizes climate to increases in CO_2 and other greenhouse gases. The distribution and quantity of atmospheric moisture is correlated with cloud feedback, and, through the impact of freshwater fluxes on the overturning ocean circulation, ice-albedo feedback. The oceanic branch of the hydrological cycle stores and redistributes sensible and latent heat, impacting both the global heat balance and regional climates. Over land, the balance of precipitation and evaporation of moisture, and the corresponding routing of runoff, influences the strength and direction of circulations in ocean basins.

This paper includes a catalogue of graphic statistics relating to atmospheric water vapor, based on 25 years of observational data from the Geophysical Fluid Dynamics Laboratory (GFDL) Atmospheric Circulation Tape Library. These figures provide an overview of the mean state and interannual variability of the global distribution of atmospheric water vapor. The variability of vertically integrated moisture fluxes, their divergences, and precipitable water is examined in more detail through a principal component or empirical orthogonal function (EOF) analysis, and the results are discussed in light of the deficiencies of the GFDL dataset. Lastly, the moisture flux divergences computed with the GFDL data are used to drive a Goddard Institute of Space Studies (GISS) river model, and thus to estimate the annual mean and interannual variability of the outflows

for 44 major rivers.

The goal is a comprehensive, self-consistent description of the hydrological cycle which may be used for the validation of coupled ocean-atmosphere models. Until recently, computational constraints dictated that general circulation models of the atmosphere and ocean had to be run independently, with boundary conditions at the interface necessarily crude. A current and critical challenge in climate modeling is the development of physically realistic heat and moisture fluxes at the ocean/atmosphere boundary for models which include both fluid components. This effort is hindered by the inherent difficult in simply quantifying observed moisture fluxes between land, atmosphere and ocean and in assessing ocean transports (e.g., Dickson *et al.* 1994). The analysis described in this paper bypasses problems with surface observations and current measurements by enforcing a simple moisture balance.

The EOF and regression analyses performed suggest an increase in precipitable water in the tropics over the last 25 years. Although the trend exceeds a confidence level of 95%, no firm conclusion can yet be drawn due to confounding factors. Changes in instrumentation and reporting practices in moisture observations are discussed. Little conclusive evidence of a trend is found in the tropical moisture flux divergence field over the same period, though there does appear to be a significant convergent trend at high northern latitudes.

One aim of the current study is to provide reasonable values for the mean annual freshwater input into the northern, mid-, and southern Atlantic basin which are derived from the GFDL atmospheric dataset. The values obtained for the northern Atlantic are in good agreement with a variety of sources, including both observational data and models, while results for the tropical and southern Atlantic display inconsistencies with other studies. A more elusive aim is to identify the interannual variability of freshwater fluxes into the Atlantic. For the northern Atlantic, the extensive and stable sampling network and consistency with other sources supports the contention that computed variabilities are physically meaningful. For lower latitudes, the statistics obtained probably are not.

Chapter 2

Data

2.1 Moisture-related Fields

The zonal and meridional components of the monthly-mean vertically integrated moisture flux, $\overline{Q}$, are defined as (respectively)

$$\overline{Q_\lambda} = \int_{p_{top}}^{p_{sfc}} \overline{qu} \frac{dp}{g}$$

$$\overline{Q_\phi} = \int_{p_{top}}^{p_{sfc}} \overline{qv} \frac{dp}{g}$$

where p_{sfc} is surface pressure, p_{top} is the pressure at the "top" of the atmosphere, here taken as 300 mb, q is specific humidity, u eastward velocity, v northward velocity, g the acceleration due to gravity, and an overbar indicates the time mean.

Also of interest is monthly-mean, vertically integrated water vapor (precipitable water), defined as

$$\overline{W} = \int_{p_{top}}^{p_{sfc}} \overline{q} \frac{dp}{g}$$

The product $\overline{qu}$ may be written as

$$\overline{qu} = \overline{q}\,\overline{u} + \overline{q'u'}$$

where the prime indicates a departure from the monthly mean. The product $\overline{qv}$ may be expanded

the same way. The fields $\overline{u}$, $\overline{v}$, $\overline{u'q'}$ and $\overline{v'q'}$ were obtained from the GFDL Atmospheric Circulation Tape Library, which contains monthly-mean gridded analyses spanning the period from May 1958 through December 1989. The network of rawinsonde stations on which the analyses are based is shown in Figure 1. It includes about 1100 stations, though approximately half that reported on average each day (Peixoto and Oort 1992).

The objective analysis technique used to screen and interpolate the data onto a grid for an abbreviated version of this data set (spanning 1963 to 1973) is described in the Peixoto and Oort text. Notable features of the analysis scheme are that isolated data points tend to have a large radius of influence, and that extreme values in small regions tend to be reduced in absolute magnitude.

The gridded data fields have 72 divisions evenly spaced in latitude (2.5°increment) and 72 in longitude (5°increment), with a vertical resolution of 11 pressure levels (1000, 950, 900, 850, 700, 500, 400, 300, 200, 100 and 50 mb). Since the dataset has coverage south of 15°S only from 1964 on, the period included in annually averaged fields is January 1965 through December 1989. Before this, measurements in the southern hemisphere were too sparse to create a representative grid.

2.2 Surface Pressure

Surface pressures for computing vertical integrals of moisture fluxes and specific humidity are from NMC analyses, and represent monthly mean surface pressure averaged over 10 years, 1980-1989. Though a surface pressure dataset which is time dependent may provide more accurate integrals, the difference in integrated values is not likely to be large.

Chapter 3

Empirical Orthogonal Function (EOF) Analysis

A principal component, or empirical orthogonal function (EOF), analysis can be used to identify the preferred spatial patterns of variability in meteorological fields and the time scales with which they are associated. Since every EOF pattern is an orthogonal eigenvector, EOFs may generally be considered to be independent of each other, and therefore due to different underlying physical mechanisms. Exceptions may occur when the eigenvalues associated with two or more EOFs are very close in value; testing for this is discussed in the next section. For the moisture-related fields described here, an EOF analysis splits variability roughly into portions due to linear trends, the El Nino Southern Oscillation, and other causes, which may include particularly severe problems with spatial and/or temporal gaps in the observational network.

3.1 Procedure

3.1.1 Formulation of Eigenquantities

Specific humidity and moisture fluxes were vertically integrated by trapezoidal rule. The divergence of the monthly-mean moisture flux, $\nabla \cdot \overline{Q}$, was computed for each month with a centered difference method modified to take earth's curvature partially into account (see Appendix A).

The quantities $\overline{W}$ and $\nabla \cdot \overline{Q}$ were averaged annually. Each annual mean divergence field was smoothed using a 1-2-1 filter in both the meridional and zonal directions. The Oort dataset includes values for both 180E and 180W; for each latitude, the two values were averaged and treated as a single gridpoint when smoothing.

As unequal weighting of gridpoints by area in an empirical orthogonal function (EOF) analysis can cause pattern distortion (Karl *et al.*, 1982), data on the latitude-longitude grid were projected onto a grid of 800 "almost equidistant" (AE) points, generated with an iterative routine (Fig. 2). Average spacing between each pair of nearest-neighbor AE gridpoints is 7.22°; the standard deviation is 0.14°. Latitude-longitude gridpoints within 10°of an AE gridpoint contribute to the value at that gridpoint. This value is approximately the mean distance between AE gridpoints increased by a factor of $\sqrt{2}$, which insures that every point on the latitude-longitude grid is represented on the AE projection. The latitude-longitude gridpoints were linearly weighted based on their distance from the AE gridpoint subtracted from the 10°radius. The weighting scheme did slightly smooth the data; Fig. 3 shows sample data on the 73 x 73 latitude-longitude grid, and Fig. 4 shows the same data projected onto the the 800 point AE grid. The plots show that the AE grid can resolve scales greater than about 1000 km (corresponding to its 10°resolution), though peak values are reduced by about 25% (for example, the peak just off of the northeastern coast of South America). Figures which show the AE grid in latitude-longitude coordinates were produced with NCAR Graphic's bivariate interpolation scheme.

An empirical orthogonal function analysis was performed on the AE gridded annual mean fields

as described in Salstein *et al.* (1983). (Their notation is adopted here.) The starting point is a two dimensional matrix **D** which contains the time series of perturbations from the 25-year mean for each of the 800 gridpoints. The covariance matrix **R** is

$$R_{ik} = 1/25 \sum_{j=1}^{25} D_{ij} D_{kj}$$

where $1 \leq i \leq 800$ gridpoints, and $1 \leq j \leq 25$ years. A singular value decomposition (SVD) analysis reduces this matrix to a set of 24 positive eigenvalues (λ_l) and 25 normalized orthogonal eigenvectors or EOFs, ($\mathbf{e}_l$). Each EOF is associated with a 25-yr time series of coefficients ($\mathbf{c}_l$), with $\mathbf{c}_l$=$\mathbf{D}\mathbf{e}_l$. When the eigenvectors are multiplied by their associated time series and summed, **D** is recovered:

$$D_{ij} = \sum_{l=1}^{25} c_{lj} e_{il}$$

3.1.2 Significance Testing

Assessing Noise Level

A significance test for EOFs is outlined in Salstein *et al.* (1983), as follows. The interannual variance in the data explained by the l_{th} EOF is given by

$$V_l = \frac{\lambda_l}{\sum_{j=1}^{25} \lambda_j}$$

so the magnitude of V_l is a measure of how much each eigenvector contributes to total variability. To sort out what part of the EOF might be due to noise, the EOF analysis was performed on datasets in which the time series at each AE gridpoint was randomly permuted. The largest V_l obtained in 20 tests became V_l^{sig}. Eigenvectors with V_l larger than V_l^{sig} can reasonably be considered representive of coherent physical processes (Preisendorfer and Barnett, 1977).

Separation of Eigenvalues (North Criterion)

When two eigenvalues are close in value, their EOFs are not well defined - any linear combination of the different eigenvector patterns is also an EOF with the same eigenvalue. A rule-of-thumb for distinguishing adequate spacing between eigenvalues is:

$$\Delta\lambda_j > \lambda_j(2/N)^{1/2}$$

where N is the number of realizations of the data set, here 25 years. (North *et al.* 1982).

Student t Test

To test for a dependency relation between two series of variables x_i and y_i, i=1 through n, the correlation coefficient r is found using the standard formula:

$$r = \frac{\sum x_i' y_i'}{\sqrt{\sum x_i'^2 \sum y_i'^2}}$$

where $x_i' = x_i - \overline{x}$ and $y_i' = y_i - \overline{y}$.

The correlation coefficent alone does not provide sufficient information to determine whether a correlation is significant. To do this, a null hypothesis is formed (i.e., that $r = 0$) and tested against its antithesis ($r \neq 0$). Assuming that x_i and y_i have a bivariate normal joint pdf, the relevant statistic is the Student t distribution with $n - 2$ degrees of freedom, which in this case is:

$$T = \frac{r\sqrt{n-2}}{\sqrt{1-r^2}}$$

If $|T|$ exceeds the critical value of the Student t distribution for $n-2$, t_{n-2}, then the null hypothesis - that the variables are uncorrelated - is rejected (e.g., Larsen *et al.* 1981).[1]

This technique can be used to test for significance of a linear trend by letting either x_i or y_i be

[1] Values for the Student t distribution are tabulated for standard significance levels in statistical tables.

the independent variable (year, for example) (Green *et al.* 1977).

Please note...

For the remainder of the thesis the overbar on $\overline{W}$ and $\overline{\nabla \cdot Q}$ will refer to an *annual* mean.

3.2 Results

3.2.1 Results of EOF Analysis

EOF_1 (the notation EOF_n for the nth EOF pattern will be adopted) for the water vapor flux divergence and its time series are shown in Fig 5. V_1 is 23.2%, well above $V_1^{sig} = 6.0\%$, and there is adequate separation between the eigenvalues of EOF_1 and EOF_2 based on the North criterion. The time series suggests a roughly linear trend spanning the 25 year period, characterized generally by increasing divergence in the tropics. This band is flanked by regions of increasing convergence to the north and south; the southern hemisphere is dominated by a strongly increasing convergence off the southeastern coast of Brazil. The significance of the apparent trend is discussed in Section 3.2.2.

EOF_2 and EOF_3 for moisture flux divergence and their time series are shown in Figs. 6 and 7, respectively; both are above the significance level V_1^{sig}. Though their eigenvalues are inadequately spaced based on the North test, their patterns are quite different and suggest distinct causes. EOF_2 appears to be dominated by stations around the southern part of Africa and northeastern South America. The stations near southern Africa reported for only three of the years between 1963 and 1973, an intermittency which, given the large radius of influence of isolated stations inherent in Oort's objective analysis scheme, would have a major impact on variability. Questions concerning which years in particular were reported, and why there is a large perturbation around 1978 in EOF_2's time series, remain unanswered.

The strong Pacific feature in the third EOF suggests an El Nino signal. In Fig. 7, the Southern Oscillation Index (SOI) from the NCEP Climate Prediction Center is plotted for the same years as

the times series of EOF_3 coefficients. (See Appendix B for a brief description of this dataset and the method for calculating the SOI.) A Student t test shows that indeed the EOF_3 coefficients and SOI are correlated at a 99% confidence level ($r^2 = 0.62$, $T = 6.18$ and $t_{23} = 2.81$). Coefficients of EOF_2 did not correlate significantly with the SOI.

The time series coefficients of EOF_1 for precipitable water (Fig. 8), like those of the flux divergence, show a linear trend. At 40.1%, V_1 is much larger than V_1^{sig}, which is 6.5%, and there is sufficient separation between the eigenvalues of EOF_1 and EOF_2 for them to be distinct. There is an overall rise in $\overline{W}$ in the tropics, with maxima over the western Pacific, Brazil and the Guiana Basin. An anomalous decrease in the Angola Basin can be attributed to an isolated station near St. Helena Island which dominates the entire region. The coefficients for EOF_2 (Fig. 9) correlate with the SOI at a 99% confidence level. ($r^2 = 0.32$, $T = 3.32, t_{23} = 2.81$.) EOF_3 (Fig. 10) is indistinguishable from EOF_2 based on the North test. Though it does not correlate as well as EOF_2 with the SOI, the patterns of these two EOFs are similarly structured..

3.2.2 Trend Analysis

Motivation

Rising levels of atmospheric CO_2 and other trace gases may be increasing the temperature of the troposphere. Since, as the Clausius-Clapeyron equation shows, saturation vapor pressure increases exponentially with increasing temperature, heated air holds more moisture. Observational studies show that moisture and temperature are indeed correlated, at least in the tropics, at all tropospheric levels (Sun *et al.* 1995). Hence a long-term rise in atmospheric water vapor would be part of a consistent global climate change signal. Efforts to quantify long-term trends in atmospheric water vapor have been hampered by short time series, interannual variability that is large relative to suspected trends, changes in hygristor design and reporting practices, and relentlessly poor data coverage over the oceans and the Southern hemisphere. At least one study nonetheless indica s

that a net increase in this quantity is occurring (Gaffen *et al.* 1991).

Despite its limitations, the currently available data may well hold information which could contribute to a coherent view of climate change. A reasonable approach in assessing whether or not a trend in atmospheric water vapor exists might be the following: to identify observed quantities which would be related to its increase; to characterize the interannual variability of those quantities; to identify any trend that is distinguishable from the interannual variability and cannot be attributed to some extraneous event; and to look for consistency among different quantities, analyses, and datasets.

Precipitable water calculations assess apparent water vapor trends directly. Changes in the divergence of the moisture flux identify sources of water vapor and suggest the dynamics of its transport.

Results of Linear Regression

EOF_1 for the moisture flux divergence is consistent with a linear regression performed at each of the gridpoints, shown in Fig. 11, in the spatial patterns and magnitude of the apparent trend. Fig. 12 shows the linear trend zonally averaged, with a significance test at the 95% level plotted below it. For most latitudes, including the tropics and midlatitudes, the trend falls below the significance level. Data paucity in the southern hemisphere, particularly south of 60°, is probably enough reason to dismiss the peaks present there. A trend towards convergence at northern high latitudes is the most significant and perhaps most believable feature. This region is well sampled, and the apparent trend exceeds even the 99% confidence level of $t_{23}=2.81$.

Overall the trend in moisture flux divergence is overwhelmed by the interannual standard deviation, which is about an order of magnitude greater than the trend globally. This can be seen by comparing Fig. E-30 (peak about 60 cm/yr^2) with Fig. 11 (peak regions about 6 cm/yr^2).

For precipitable water, the first EOF is also consistent with a linear regression (Fig. 13). The

zonally averaged trend in this case (Fig. 14) exceeds the 95% significance level considerably in the tropics. The annual global increase in precipitable water associated with the apparent trend is $2x10^{13}$ kg/yr. Over 25 years, this amounts to $4.8x10^{14}$ kg of water added to the atmosphere. Here too the trend in $\overline{W}$ on a yearly basis is about an order of magnitude less than the interannual standard deviation (Fig. E-21) in regions of global maxima.

3.3 Discussion

3.3.1 Error Analysis

In interpreting the results presented above it is crucial to assess how changing reporting practices and instruments may affect the results. It is assumed that the mass introduction of the carbon hygristor at U.S.-operated stations, in 1964/65, will not substantially affect the dataset used here. (However, as the new instrument and reporting practice spread world-wide in subsequent years, they could well produce anomalous results, especially at isolated stations.) Perhaps the greatest disruption of the humidity data occurred in 1973, when the practice of reporting all humidities below 20% as 19% was adopted in the U.S. In viewing the results of this paper, it is reassuring to note is that the apparent trends persist after 1973, and that the results obtained agree roughly with those of Gaffen *et al.*, whose analysis starts in 1973. There is currently no systematic, international record which documents reporting practices for humidities less than 20% (Gaffen *et al.* 1991). However, given that consistently reporting 19% for very low humidities biases the data towards moist values, it would be valuable to know how quickly other countries adopted the practice. The last relevant major change in humidity measurement occurred in 1980, when new carbon hygristors were introduced and the equation for conversion from relative humidity to specific humidity changed. Elliot and Gaffen (1991) are unable to characterize its impact on the humidity data, stating, "there was a complicated change in procedures for processing radiosonde signals around 1980 whose effects are difficult to estimate." There is no indication that a major bias was introduced during these years in the first

and second EOFs of annual mean $\overline{W}$ and $\overline{\nabla \cdot Q}$.

Another indication of the robustness of trends in atmospheric moisture is a comparison between the GFDL analyzed fields and a new reanalysis of rawindsonde data (Parker and Cox, 1995). The reanalysis includes correction of a systematic error in wind velocities due to confusion over the units of reported data. The erroneous reports (in m/s instead of the standard knots, leading to a factor of two discrepancy) were submitted primarily by the former USSR, Eastern Europe and China. Values were checked in the reanalysis by calculating local geopotential height gradients, and by comparing monthly average vector wind speeds on opposite sides of national borders. In assessing the physical significance of observed trends in moisture flux divergence, it would be helpful to know the temporal and spatial distribution of erroneous wind velocity data in the GFDL dataset. Recent political upheavals in Eastern Europe have resulted in at least one nation standardizing wind velocity units; East Germany switched after reunification in 1991. However, it is probably a fair assumption that nations which reported in non-standard units did so consistently over the duration of the GFDL dataset, so that misreported units have not influenced the calculation of trends.

Biases associated with reporting relative humidities below 20% are discussed in Parker *et al.*, though the explicit methodology for removing the biases is not provided. A general scheme is described in which includes comparing data to neighboring stations, operational model analyses, and other datasets where available, and modeling the thermodynamics of radiosonde instruments.

It is worth noting that a systematic change in ascent times occurred in 1957. Though the large-scale switch in ascent times precedes the years included in this paper's analyses, sporadic changes in ascent times and changes in their frequency are worth noting as an additional, possibly relevant error source.

Figs. 15 and 16 show annual mean precipitable water determined using the reanalyzed data and the difference between the reanalysis and the GFDL dataset, respectively. The GFDL dataset is systematically wetter in the tropics (by about 10%, or 4 kg m^{-2}). The zonally averaged trend in the tropics computed using GFDL data, as shown in Fig. 14, is at most 0.16 kg m^{-2} yr^{-1}, or 1.6 kg

m^{-2}. The fact that the computed trend is about half the observed discrepancy in the two analyses warrants caution in concluding that the trend is physically significant.

The extent of errors due to spatial gaps in the GFDL dataset are investigated in Oort (1978). Oort compares statistics obtained with the full gridded fields of a GFDL climate model with statistics obtained from the same fields sampled only where there are rawinsonde stations. Examining the zonally and vertically averaged meridional moisture flux in January and July, there is good agreement between the two datasets at all latitudes (Fig. 17). Oort comments that discrepancies in the station-sampled dataset are likely due to difficulties in quantifying the residual meridional circulation and not specific humidity, which is a relatively slowly varying, uniform field. He also notes that errors in the station-sampled meridional circulation create a bias of increased moisture transport to the equator.

3.3.2 Comparison with Other Studies

Salstein *et al.* (1983) performed EOF analyses on water vapor transport and divergence fields on data from the GFDL General Circulation Data Library, the same dataset used in this thesis. However, Salstein *et al.* employ the ungridded form of the data, selecting 91 stations in the northern hemisphere which are roughly equidistant, and which cover a different and shorter time period (1958-1973) than the present study.

The leading pattern for precipitable water does not resemble that obtained from radiosonde data by Salstein (1983), which accounted for 44.1% of the variability of $\overline{W}$ and roughly showed an increase in the tropics from 90°W to 90°E and a decrease elsewhere. As noted by Gaffen *et al.* (1991), the apparent drying trend over the U.S. and the Pacific in Salstein *et al.* could be due to the replacement of lithium chloride hygristors with a newly housed carbon hygristor at U.S.-operated stations in 1964/65. Also at this time, stations began reporting relative humidity measurements below 20%, which were ignored with the older instruments. The longer time period which this thesis

covers would tend to make the influence of the changes in reporting practice and instrumentation less noticeable in the leading EOF for $\overline{W}$.

Gaffen *et al.*(1991) use an ungridded global network of 118 radiosonde stations during the period 1973-1985 to derive EOFs for specific humidity at 4 pressure levels (surface, 850, 700 and 500 mb). The time series for the first EOF shows a rather sharp jump in $\overline{W}$ in 1976/77, and a crudely linear increase thereafter. An increase of about 1 g/kg at 850 mb over 13 years is indicated at 4 stations selected for their large eigenvector amplitude; assuming this increase occurs between 800 and 1000 mb and between $\pm$ 30° latitude, the annual increase is about 4×10^{13} kg/yr, the same order of magnitude as the trend calculated here (2×10^{13}).

3.3.3 Conclusions

The two leading EOFs for precipitable water and moisture flux divergence are at a very basic level consistent with each other in that the tropics, which show the largest increase of water vapor, are implicated as its source. This isn't terribly surprising given that the two quantities are correlated through q. Whether or not the character of the observed trends is consistent with the distribution and magnitude of temperature increases related to greenhouse warming will not be pursued in depth here. Briefly, assuming a 6% change in specific humidity for every degree Centigrade change in temperature, the temperature rise corresponding to the apparent increase in precipitable water is about 0.8° C.[2] The apparent temperature rise during the period 1965-1989 was about 0.4° C. (See Fig. 18, from Hansen and Lebedeff, 1987.)

A Sun and Oort (1995) study provides empirical evidence that fluctuations of humidity with temperature can be detected, since they find that temperature variations correlate with humidity variations at all levels of the troposphere, using the GFDL analyzed gridded data from the period 1963-1989. However, the authors caution against extrapolating their results to long-term changes

[2] Estimated from the Clausius-Clapeyron equation, assuming relative humidity stays constant.

in atmospheric moisture associated with greenhouse warming, citing not only data deficiencies of the sort discussed earlier but additional processes (e.g., changes in ocean circulation) that influence atmospheric moisture content over decadal and longer time scales.

In summary, there is the suggestion of a consistent trend in this paper's analysis and that of Gaffen *et al.*, but the inadequacies of the data set preclude a definitive conclusion concerning its significance to be drawn.

Chapter 4

Atlantic Basin Freshwater Flux Calculations

A self-consistent representation of the hydrological cycle can be achieved by tracking the path of precipitation less evaporation over land, and determining where freshwater is returned to the sea. Freshwater fluxes, particularly at high latitudes, are critical in determining the strength and direction of the overturning circulations in ocean basins. However, it's difficult to ascertain what reasonable values for these fluxes are. Zauker *et al.* (1994) compute freshwater fluxes for the Atlantic, Pacific and Indian ocean basins using three different data sets (an atmospheric GCM, the GFDL climatology used in this study, and ECMWF data), and find very poor agreement. Oki *et al.* (1993) attempt to compute a series of annual river outflows using water vapor flux convergences from the European Centre for Medium-Range Weather Forecasting (ECMWF) and find discrepancies of 100% and more with observations commonplace.

Changes in ocean circulation due to variability of the Atlantic freshwater influx may be important for producing climate fluctuations on annual or decadal time scales. Also, studies have suggested that oceans possess multiple equilibria with transitions prompted by changes in freshwater fluxes (e.g., Marotzke *et al.* 1991). How much of a change in North Atlantic freshwater inflow might cause the direction of overturning to reverse, and whether such a change would fall within the bounds of

natural variability, are questions crucial to the understanding and prediction of long-term climate change.

4.1 GISS River Model

4.1.1 Description

A river flow model courtesy of the Goddard Institute for Space Studies (GISS), provided by Gary Russell, was used to estimate the annual mean and interannual variability of the ouflow of 44 major rivers. A listing of the rivers included in the model is provided in Table 4-1.

The hydrological balance equation for a given region is

$$\langle \overline{R} \rangle + \langle \frac{\overline{\partial S}}{\partial t} \rangle = -\langle \overline{\nabla \cdot Q} \rangle - \langle \frac{\overline{\partial W}}{\partial t} \rangle,$$

where the overlines represent annual mean values, and brackets indicate a space average over an area (here a gridbox). R is the average rate of runoff, S is surface and underground water storage, and W is atmospheric water storage. The rate of change of atmospheric moisture storage is negligible on an annual basis, and annual changes in water storage on land may be neglected to a first approximation. It follows that the rate of runoff can be equated with the convergence of the moisture flux.

The model routes runoff specified at each gridbox of a 4° by 5° latitude-longitude grid to one of the eight nearest or next-nearest neighbor boxes at each timestep, here one day. For each timestep, the amount of water in a given gridbox is:

$$S + F_{P-E} + F_{upstream} - F_{downstream}$$

where S is water remaining in the box from the previous timestep, F_{P-E} is moisture added by the atmosphere, $F_{upstream}$ is any inflow of water from neighboring gridboxes, and $F_{downstream}$ is the

outflow of water into a downstream gridbox. Using the model, a river's basin was defined to include each gridpoint whose contents eventually flow through the river's mouth. Gridpoints that are not associated with one of the river basins in the model are ignored in the calculation. The routing map stays constant throughout the model run and is actually on a finer grid (2° by 2.5°) than the forcing; runoff is interpolated to the higher resolution before integration.

Fig. 19 shows the GISS model's 2° by 2.5° grid. A letter indicates that a gridpoint is associated with a river basin, and circled letters mark the location of a river mouth. The rivers corresponding to each letter are listed in Table 4-1.[3] The solid line in Fig. 19 shows the drainage divide between the Atlantic and Pacific Oceans. It was drawn based on a similar map in Zauker and Broecker (1992) and on paths suggested by the routing scheme in the GISS model.

4.1.2 Impulse-Response

A run was performed in which moisture was evenly distributed in area at initialization of the river model, and there was no forcing during the model run. The results from this experiment indicate the time scales associated with flushing a parcel of water through a river system.

Results are shown in Fig. 20 for five rivers of different sizes. The longest time scale associated with river flow was about 6 months, for the Amazon. Smaller rivers, like the Loire, have flows with time scales closer to a few months. This exercise confirmed that the model rivers had time scales similar to their actual counterparts; for smaller rivers, scales on the order of a month are indicated by Sokolovskii (1968).

[3]The indices in Table 4-1 are those used by the GISS model. An asterisk (*) marks a land or ice gridpoint which does not belong to a river basin. They may be helpful to a reader trying to recreate or investigate the work presented here.

4.1.3 Forcing with Moisture Flux Convergence

Monthly-mean divergence of the moisture flux computed using the GFDL dataset, averaged over the period 1965-1989, was interpolated using simple linear weighting to a 4°by 5°grid. Gridded, unsmoothed flux convergence field were input to the GISS river model as the equivalent of monthly mean runoff over land and glacial ice, based on the hydrological balance equation. A sample input field is presented in Fig 21. Note that there are regions in which evaporation exceeds precipitation in the monthly mean (negative values). The treatment of net evaporation at a gridpoint is straightforward; this quantity is subtracted from the available water at the gridpoint and the remainder is routed forward.

The river model was initialized by running for three years starting in January 1964, beginning with zero storage at all gridpoints. A mean of the end-of-December storage values for these three years was computed, and this mean was used to initialize the first month of a 26-year integration which spanned January 1964 through December 1989. Only the period January 1965 through December 1989 is included in the statistics presented, corresponding to the GFDL atmospheric dataset. Given that the GISS river model time scales are on the order of months, that an additional year was included prior to the "official" 25-year run, and the initial three-year averaging, no transient startup effects are likely to be present in the results.

Annual means and interannual standard deviations for river mouth outflow derived from the GISS model are shown in Table 4-1, along with observed values of annual river outflow based on surface data. Observed values are from Baumgartner and Reichel ("B and R", 1975), and from the Global Data Runoff Centre (GRDC). These datasets are described in Appendix D.

Time series for the 44 rivers in the GISS model are shown in Figs. 22a though 22i, along with GRDC data (dashed lines). GRDC river data are only shown for time series which included 10 or more years. The small figure at the bottom right of each plot indicates approximately how far it is from the river mouth to the observing station at which the GRDC data was collected. These figures,

Table 4.1: **Major River Outflows (km^3/yr)**

River	Letter	(Index)	B and R	GRDC	Mean	Std. Dev.
Amazon	A	(1)	6000	4901	4839	1058
Amur	X	(24)	350	307	-24	182
Brahmaputra-Ganges	B	(2)	1120	1000	445	295
Caspian Sea	c	(29)			-216	72
Colorado	o	(41)			70	72
Columbia	W	(23)			135	73
Congo(Zaire)	C	(3)	1330	1269	-42	636
Danube	D	(4)			-10	55
Elbe	e	(31)			-11	17
Fraser	F	(6)			102	27
Godavari	y	(51)			-103	181
Hsi Chiang	H	(8)			172	116
Indigirka	i	(35)			10	27
Indus	I	(9)			-376	128
Irrawady	R	(18)	440	258	187	112
Kolyma	k	(37)			69	45
LaPlata	P	(16)	615	516	249	714
Lena	L	(12)	515	524	349	109
Limpopo	z	(52)			-132	85
Loire	l	(38)			39	23
Magdalena	G	(7)			519	109
McKenzie	K	(11)		267	206	82
Mekong	V	(22)	500	294	314	214
Mississippi	M	(13)	560	464	120	271
Murray	m	(39)			-310	154
Niger	N	(14)		35	-287	213
Nile	n	(40)		39	49	452
Norton	h	(34)			112	92
Norwegian rivers	j	(36)			110	48
Ob	O	(15)	395	394	455	218
Orange	q	(43)			-289	164
Orinoco	Q	(17)	915	980	1404	326
Rhine	r	(44)			-14	33
Rio Grande	g	(33)			-65	58
Sao Francisco	f	(32)			-827	185
Severnay Dvina	s	(45)			68	45
St. Lawrence	S	(19)	330	250	83	58
Tigris-Euphrates	t	(46)			-524	165
Volga	v	(48)		255	291	108
Yangtze	Y	(25)	1100	789	772	186
Yellow	T	(20)			-198	78
Yenesei	E	(5)	565	558	323	119
Yukon	U	(21)			290	49
Zambesi	Z	(26)		105	279	231

which were estimated by the author using an atlas, may be considered accurate to about 50 km. For some rivers, the distance to the observing station was more than 700 km, and in these cases agreement is generally poor.

4.2 Atlantic Freshwater Fluxes

For this calculation the annual freshwater flux into the Atlantic was divided into three components: river outflows, runoff from land not associated with any river basin, and precipitation less evaporation added directly to the ocean. The calculation was done first for every 4 degree latitude strip in a 4° by 5° grid. A river's outflow was added to the freshwater flux at the latitude of the river's mouth. Runoff from a gridpoint not associated with a river basin (the *'d gridpoints in Fig. 19) was added to the freshwater flux at the gridpoint's latitude. The flux convergence over an ocean gridpoint was also added to the gridpoint's latitude band. Means and standard deviations were computed at each latitude. Results are shown in Table 4-2. The same table is reproduced in Appendix C in units of sverdrups for convenience.

4.2.1 Results

4.2.2 Comparison with Other Studies

A number of of modeling and observational studies have investigated the freshwater flux into the Atlantic. The first line of Table 4-3 summarizes results which were presented in Table 4-2 of the previous section. Listed below are estimates from other studies.

Baumgartner and Reichel ("B and R") present values of the freshwater flux into the Atlantic for 5° latitude bands in their atlas (1975). Their estimates are based on regional maps, compiled over assorted time periods which at best overlap the first decade of the GFDL dataset. (See Appendix

Table 4.2: **Atlantic Freshwater Fluxes (km^3/yr)**

Latitude	River runoff		Land runoff		Ocean P-E		All	
	Mean	Std. Dev.	Mean	Std. Dev.	Mean	Std. Dev.	Mean	Std. Dev.
90	0	0	-3	16	0	0	-3	16
86	0	0	63	93	0	0	63	93
82	0	0	197	101	0	0	197	101
78	0	0	191	73	-15	31	176	79
74	1136	236	157	107	82	36	1376	269
70	275	90	531	104	318	76	1124	157
66	68	44	436	88	506	97	1011	142
62	110	47	507	140	501	130	1118	207
58	320	97	762	182	423	80	1506	198
54	-14	33	612	195	502	67	1100	218
50	83	58	248	279	648	169	980	359
46	39	23	463	288	237	117	739	347
42	0	0	481	393	188	162	669	443
> 40	2018	362	3393	346	4650	875	10061	1068
38	0	0	600	360	-365	243	234	456
34	0	0	624	411	-339	138	284	457
30	120	271	-313	535	-609	238	-803	636
26	-65	54	-1865	517	-555	312	-2486	495
22	0	0	-4229	569	-984	294	-5214	568
18	0	0	-3630	739	-1611	358	-5241	885
14	518	109	-2700	709	-142	311	-2324	722
10	1403	325	63	545	58	276	1525	671
6	0	0	2028	549	2467	495	4496	942
2	4552	1050	1130	539	1505	546	7187	1454
0 to 40	6529	924	-578	1447	-8291	2112	-2340	2289
-2	0	0	-634	670	669	375	34	681
-6	-41	635	-1184	596	-796	355	-2021	795
-10	-827	184	-2714	426	-1751	384	-5293	800
-14	0	0	-3379	598	-252	93	-3631	637
-18	0	0	-2615	555	-813	147	-3428	624
-22	0	0	-1109	491	-1167	178	-2276	591
-26	0	0	-305	635	-1019	195	-1324	772
-30	-289	163	-331	554	-636	256	-1257	662
-34	249	714	-531	329	-216	131	-498	787
-38	0	0	-334	284	150	120	-183	341
-40 to 0	-909	752	-5831	882	-13139	3572	-19880	3977
-40 to 90	7639	1504	-3016	1449	-16780	3421	-12157	3123

D for a brief description of their methodology.) Given the temporal incoherency of B and R data and little temporal coincidence between the B and R and GFDL datasets, the fairly large differences between the results of this thesis and those of B and R are not surprising. Figure 23 shows the the GFDL and B and R analyses as a function of latitude.[4]

Broecker et.al. (1990) employ two approaches, the first a simulation of the atmosphere using the GISS General Circulation Model (described in Hansen *et al.* 1983) and the second a global ocean box model designed for geochemical studies (Broecker and Peng, 1986, 1987). The GISS GCM is on an 8° by 10° grid and uses drainage divides to determine what part of the moisture flux convergence over continents will be routed to a given ocean basin.[5] The GCM was integrated under current climate conditions for three years. The GCM results are in particularly good agreement with the results of this thesis at high northern latitudes, where all quantities (runoff, P-E, and total freshwater flux) are within 10%.

The ocean box model, "Pandora", has 10 boxes representing multiple levels of the global oceans, with the Pacific and the Indian Oceans combined into one box. Pandora iteratively computes implied freshwater fluxes based on observed salinity and other tracer distributions. One of the least realistic features of Pandora is its combined treatment of the Pacific and Indian Oceans, though the effect seems to be mainly an excessive water vapor flux required by the northern Pacific. The model was not calibrated in the interest of maintaining it as a truly independent estimate of fluxes. Agreement with the GCM study and with the results of this thesis are good above 40° north, well within 25%.

Bryan and Oort ("B and O", 1984) estimate P-E for the Atlantic basin for the years 1965 through 1975 based on moisture flux divergences, computed using the same GFDL atmospheric dataset (albeit a truncated version) employed in this thesis. The value they obtain is very close to that obtained here (the difference is about 10%).

Chen *et al.* also estimate P-E for the Atlantic basin based on moisture flux divergences, but they use upper-air data generated by the Global Data Assimilation System (GDAS) at the National

[4] A cubic spline fit was used to interpolate the B and R data.
[5] These drainage divides are comparable to those used in conjunction with the GFDL dataset and GISS river model.

Table 4.3: **Atlantic Freshwater Fluxes: Results from Several Studies (km^3/yr)**

	> 40			0 to 40			-40 to 0			-40 to 90		
	Runoff	P-E	All	Runoff	P-E	All	Runoff	P-E	All	Runoff	P-E	All
This study (GFDL)	5411	4650	10061	5951	-8291	-2340	-6740	-13139	-19880	4623	-16780	-12157
B and R	4634	2152	6786	6771	-19911	-13140	7357	-23816	-16459	18762	-41575	-22813
GISS GCM, 8° x 10°	4730	5050	9780	3470	-14510	-11040	3470	-17340	-13880	11670	-26810	-15140
Pandora			7880									-17340
B and O (GFDL)											-15000	
GDAS/NMC											-21900	

Meteorological Center (NMC) from the period 1979-1992. Their values are within 25% of those obtained in this study.

4.2.3 Conclusions

All studies listed in Table 4-3 show a net loss of freshwater for the Atlantic, which implies a net gain of freshwater for the Pacific. This is consistent with observations of the Pacific being about $2^o/_{oo}$ fresher than the Atlantic on average (Levitus, 1982), and confirms that all the studies possess a crude measure of validity.

South of 40° north, it appears that this study was unable to capture the basic features of the circulation. The net flux for the GFDL dataset in the tropics is about a quarter that obtained by B and R and the GISS GCM. Runoff results derived from the GFDL dataset in the southern Atlantic are oppositely signed from the other studies. Though B and R and the GISS model are certainly not infallible, they are fairly consistent with each other in sign and magnitude in the mid- and southern Atlantic. It is likely that the sparse sampling network at low and southern latitudes produced erroneous results for the radiosonde-based calculations.

However, at latitudes north of 40°, all datasets are in fairly good agreement. This coherency is likely due to the relatively stable and extensive sampling network in this region, which produced

sensible values for this study's P-E. Here contributions from runoff and P-E over the ocean contribute approximately evenly to the freshwater flux, so it is also important for the rivers that disgorge at these latitudes to be adequately modeled. The five largest rivers with mouths north of 40° are the Lena, McKenzie, Ob, St. Lawrence, and the Yenesei. Together they comprise about 70% of the total river runoff for the region. Looking at Figures 22a-22i, the time series obtained using the GISS river model are in fairly good agreement with GRDC surface observations. The GRDC annual mean estimates are within two standard deviations of the results of this study except for the St. Lawrence; this is the smallest of the five rivers. In all cases the signs and orders of magnitude are correct.

Results for P-E for the north Atlantic are fairly consistent with the GISS and B and R studies as well. As P-E is a residual which is typically about 20% of precipitation alone, the calculation is somewhat prone to error. Though B and R obtain a value which is about half that of this study and the GISS GCM, the order of magnitude is consistent. Total fluxes (P-E plus runoff) agree to within 40%.

Based on these results, it seems feasible that the GFDL dataset in conjunction with the results of the GISS river model north of 40° N could be used as a supplement to other datasets in validating or driving an atmosphere, ocean or coupled model. South of this region, the results of this study are simply too uncertain.

Figures

Figure 1. Network of upper-air stations used to as the basis of the GFDL/Oort dataset. Plotted values indicate the number of years of wind and temperature observations available at 500 mb for January for the period 1963-1973. "A" means that data was available for all years. From Peixoto and Oort, 1992.

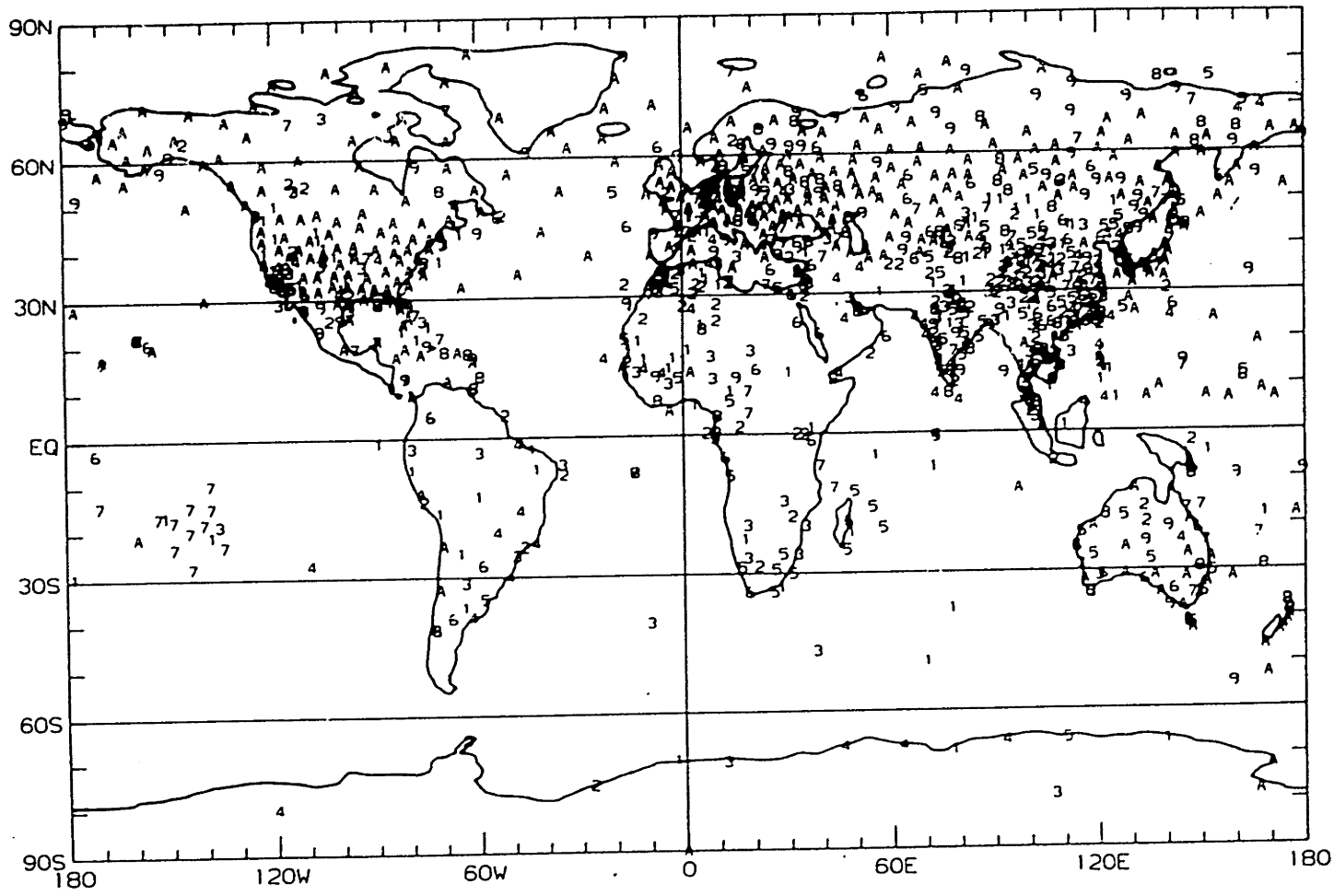

Figure 2. "Almost Equidistant" (AE) grid.

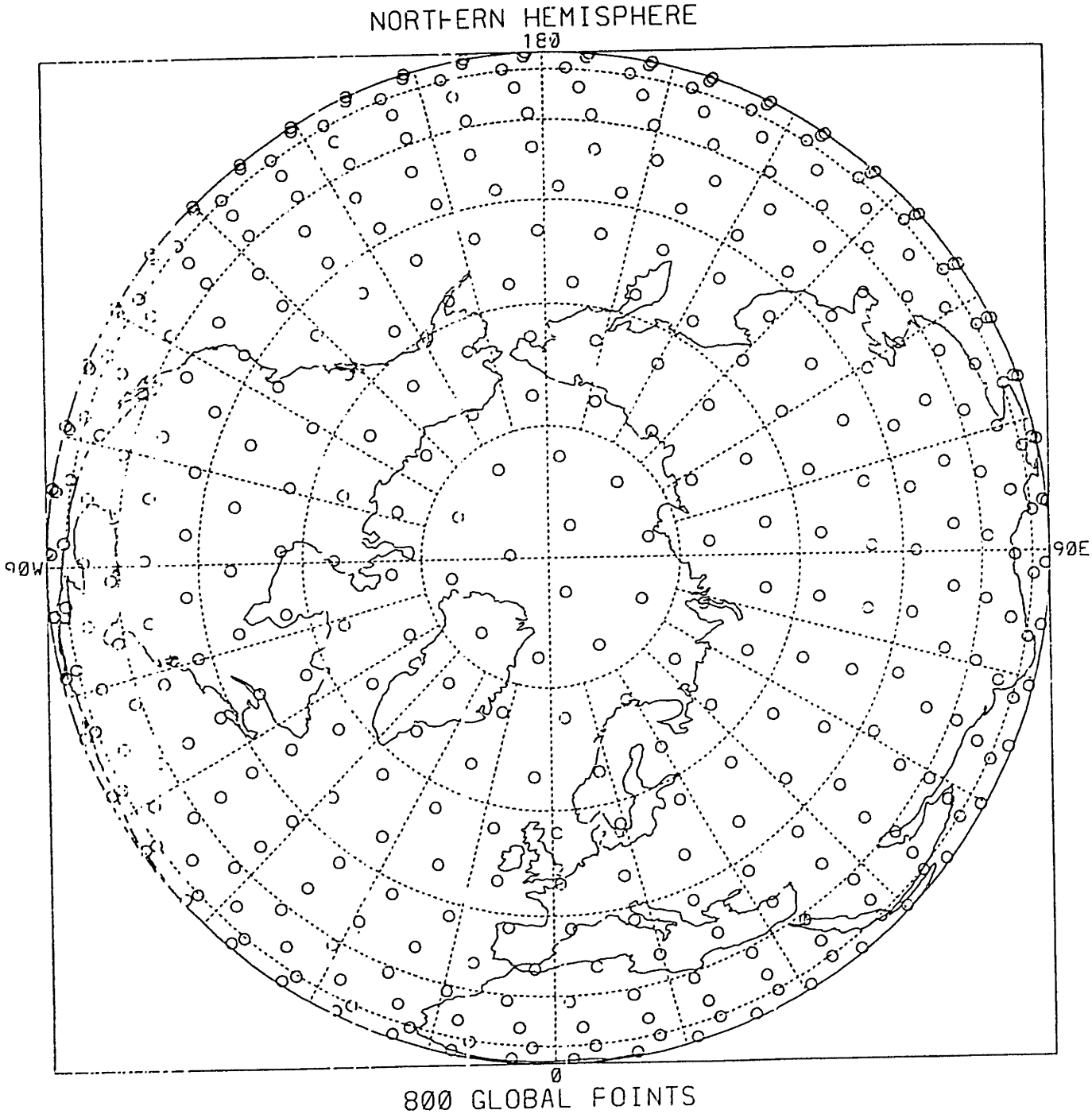

Figure 3. Sample data on the GFDL grid, which is 2.5° in latitude, 5° in longitude. The contour interval is 10.

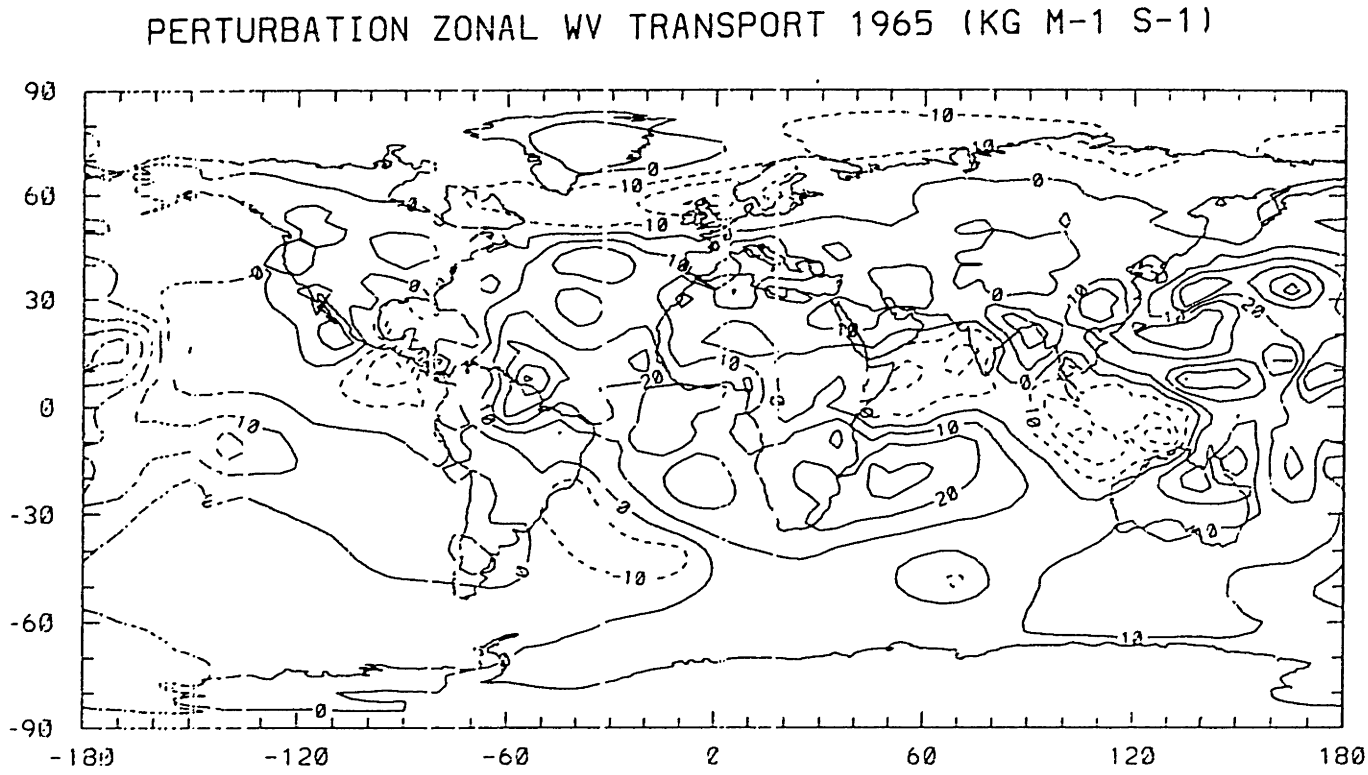

Figure 4. Sample data on AE grid. The contour interval is 10.

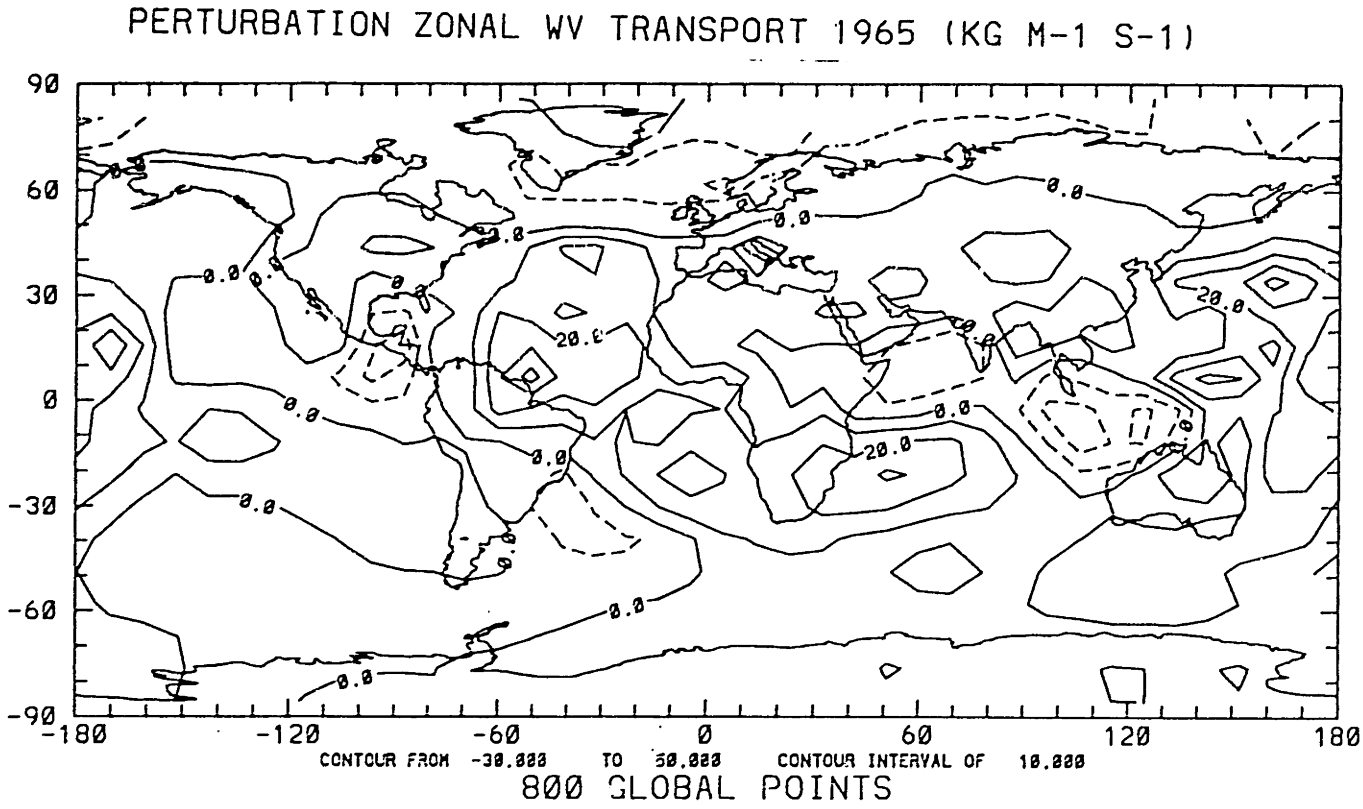

Figure 5.

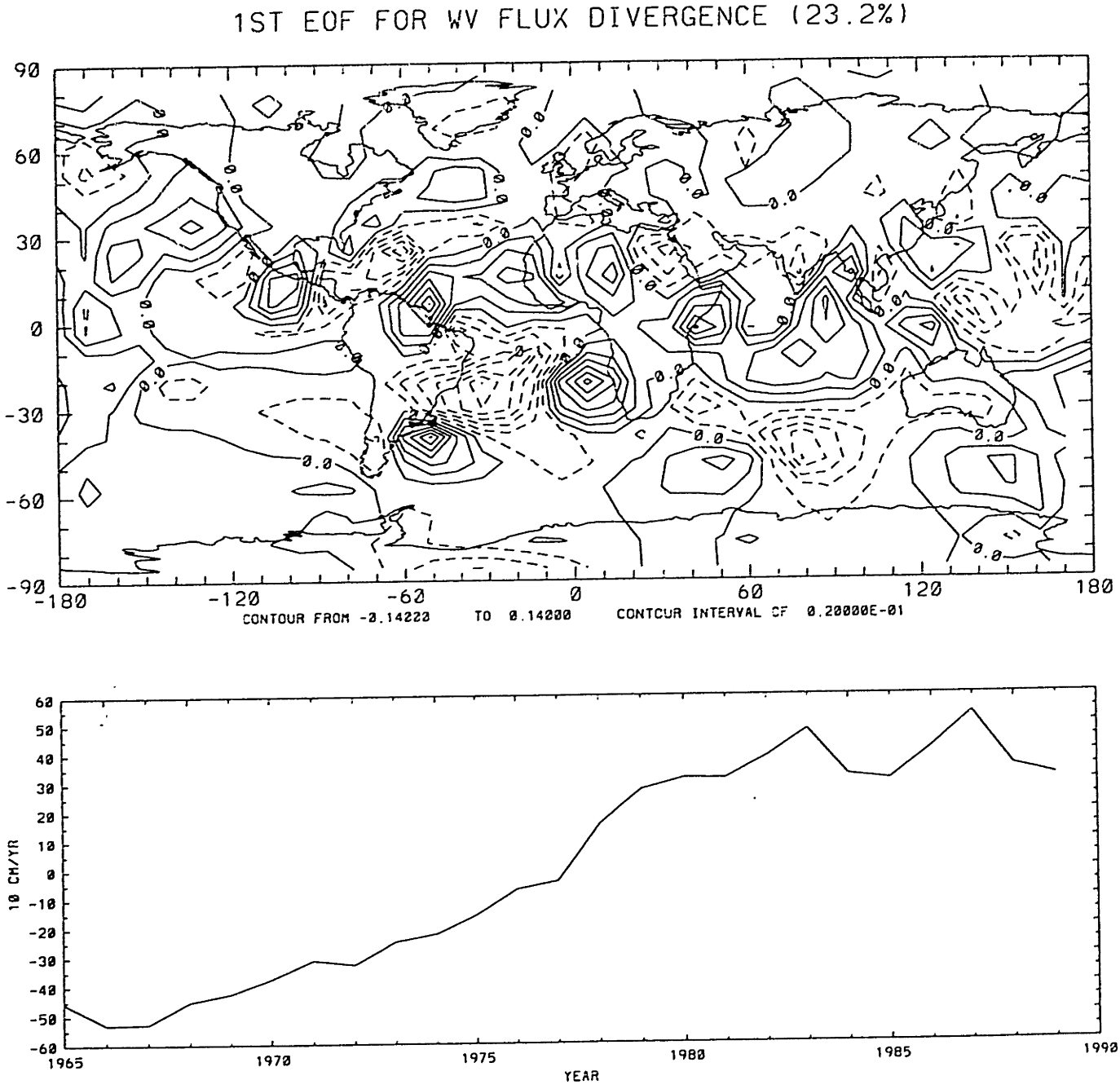
1ST EOF FOR WV FLUX DIVERGENCE (23.2%)
90
60
30
0
-30
-60
-90
-180
-120
-60
0
60
120
180
CONTOUR FROM -0.14220 TO 0.14200 CONTOUR INTERVAL OF 0.20000E-01
10 CM/YR
60
50
40
30
20
10
0
-10
-20
-30
-40
-50
-60
1965
1970
1975
1980
1985
1990
YEAR

Figure 6.

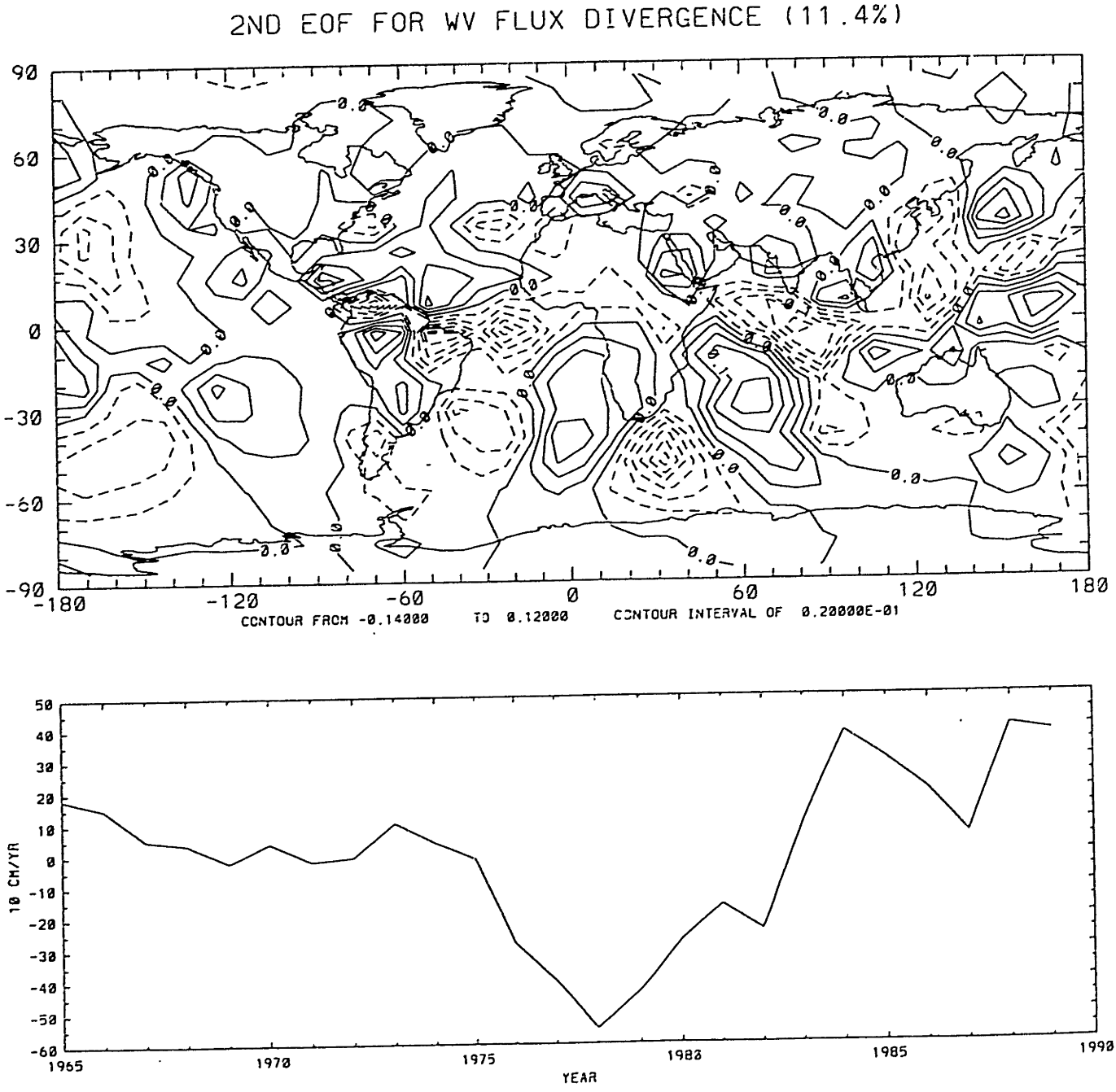
2ND EOF FOR WV FLUX DIVERGENCE (11.4%)
90
60
30
0
-30
-60
-90
-180
-120
-60
0
60
120
180
CONTOUR FROM -0.14000 TO 0.12000 CONTOUR INTERVAL OF 0.20000E-01
50
40
30
20
10
0
-10
-20
-30
-40
-50
-60
10 CM/YR
1965
1970
1975
1980
1985
1990
YEAR

Figure 7. Bottom plot shows Southern Oscillation Index (SOI).

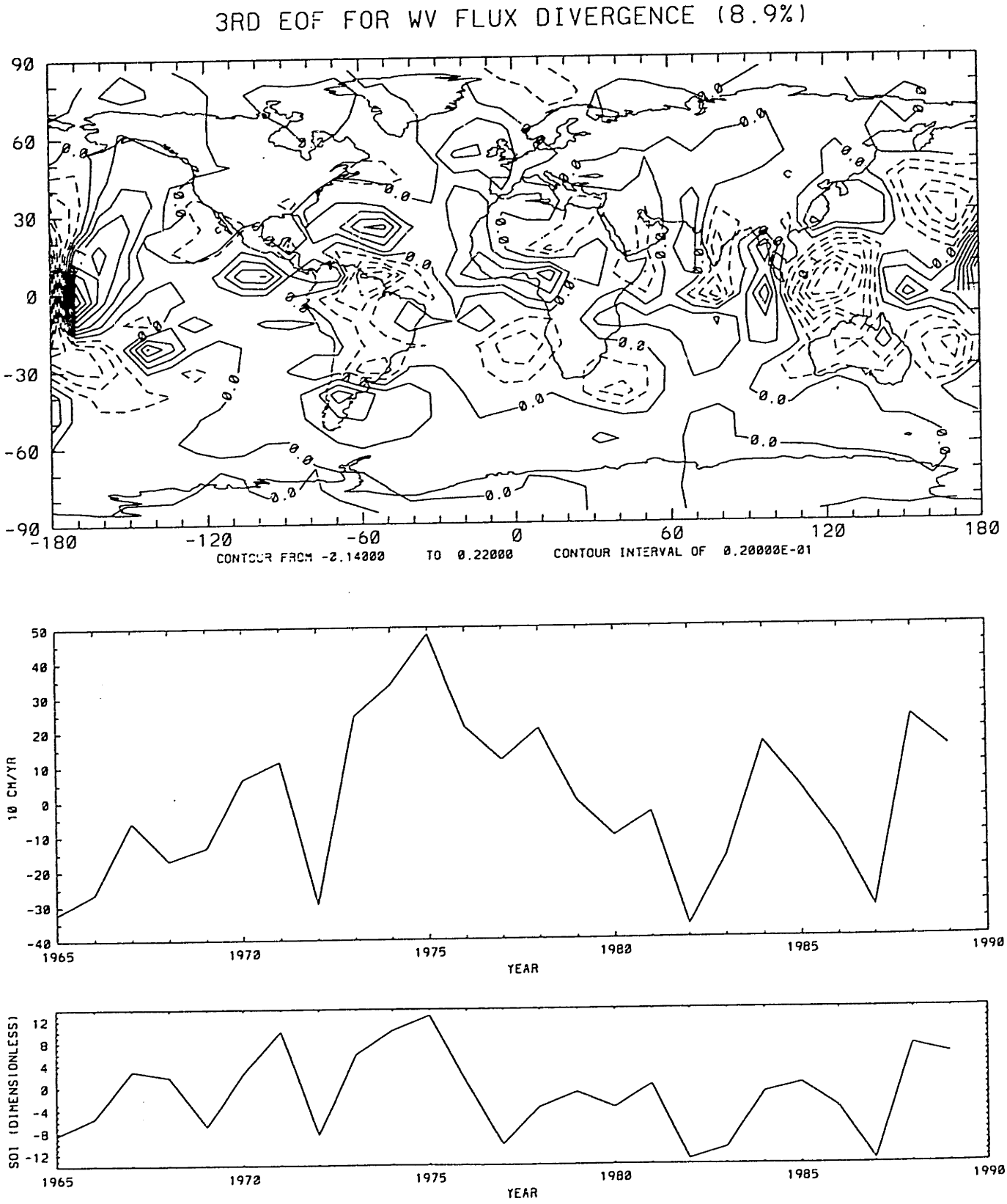

Figure 8.

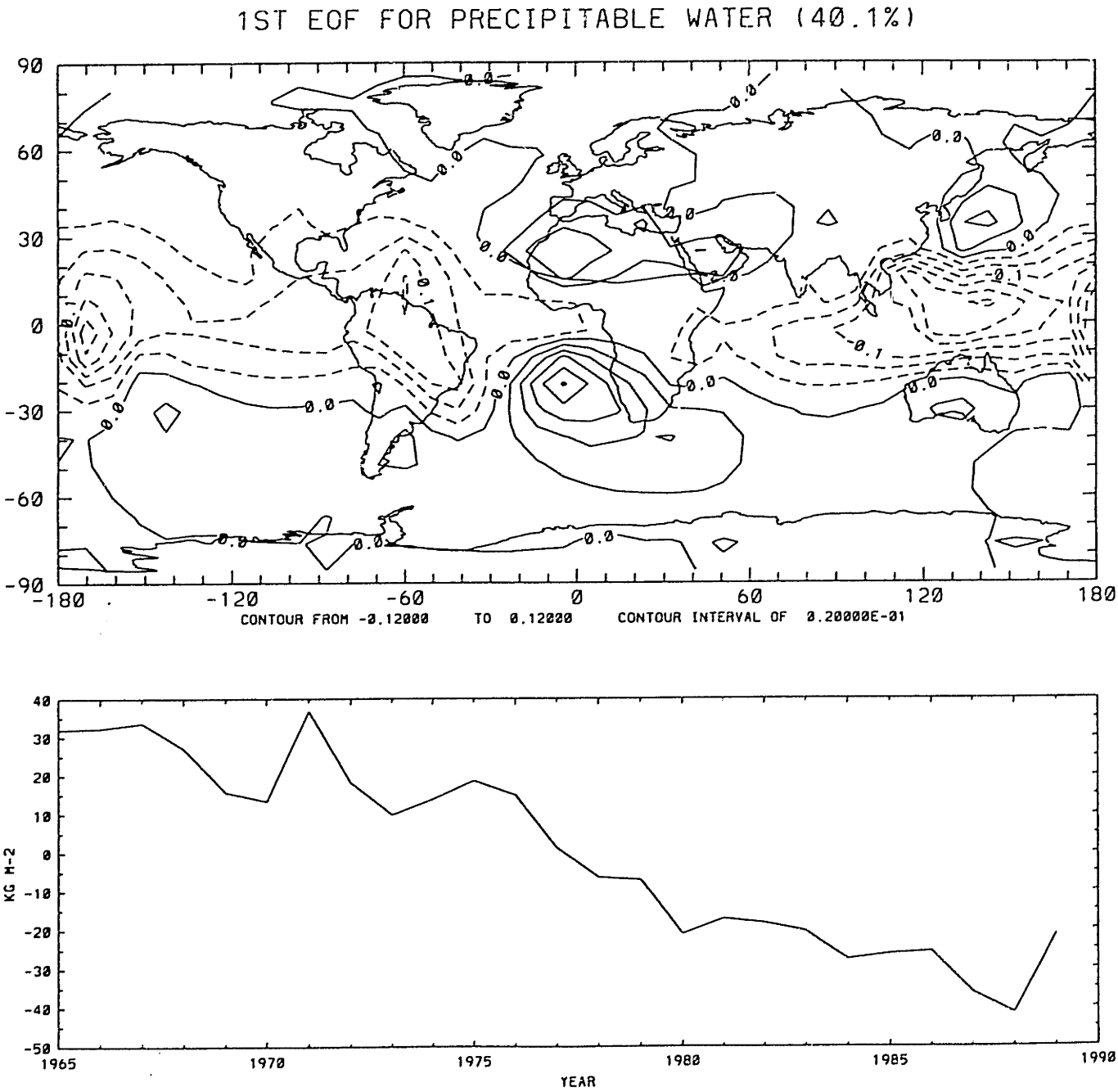
1ST EOF FOR PRECIPITABLE WATER (40.1%)
90
60
30
0
-30
-60
-90
-180
-120
-60
0
60
120
180
CONTOUR FROM -0.12000 TO 0.12000 CONTOUR INTERVAL OF 0.20000E-01
KG M-2
40
30
20
10
0
-10
-20
-30
-40
-50
1965
1970
1975
1980
1985
1990
YEAR

Figure 9.

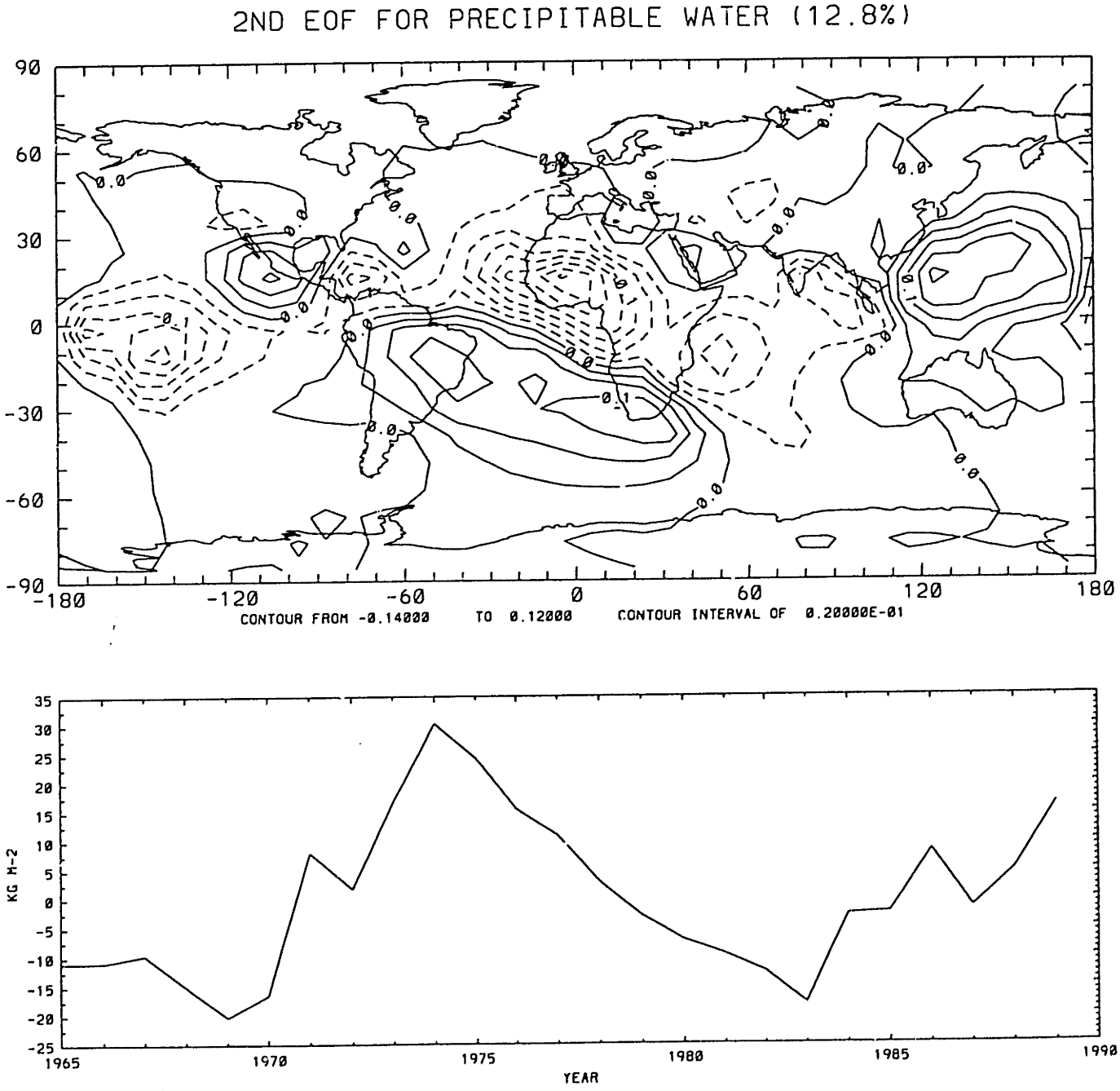
2ND EOF FOR PRECIPITABLE WATER (12.8%)
90
60
30
0
-30
-60
-90
-180
-120
-60
0
60
120
180
CONTOUR FROM -0.14000 TO 0.12000 CONTOUR INTERVAL OF 0.20000E-01
KG M-2
35
30
25
20
15
10
5
0
-5
-10
-15
-20
-25
1965
1970
1975
1980
1985
1990
YEAR

Figure 10.

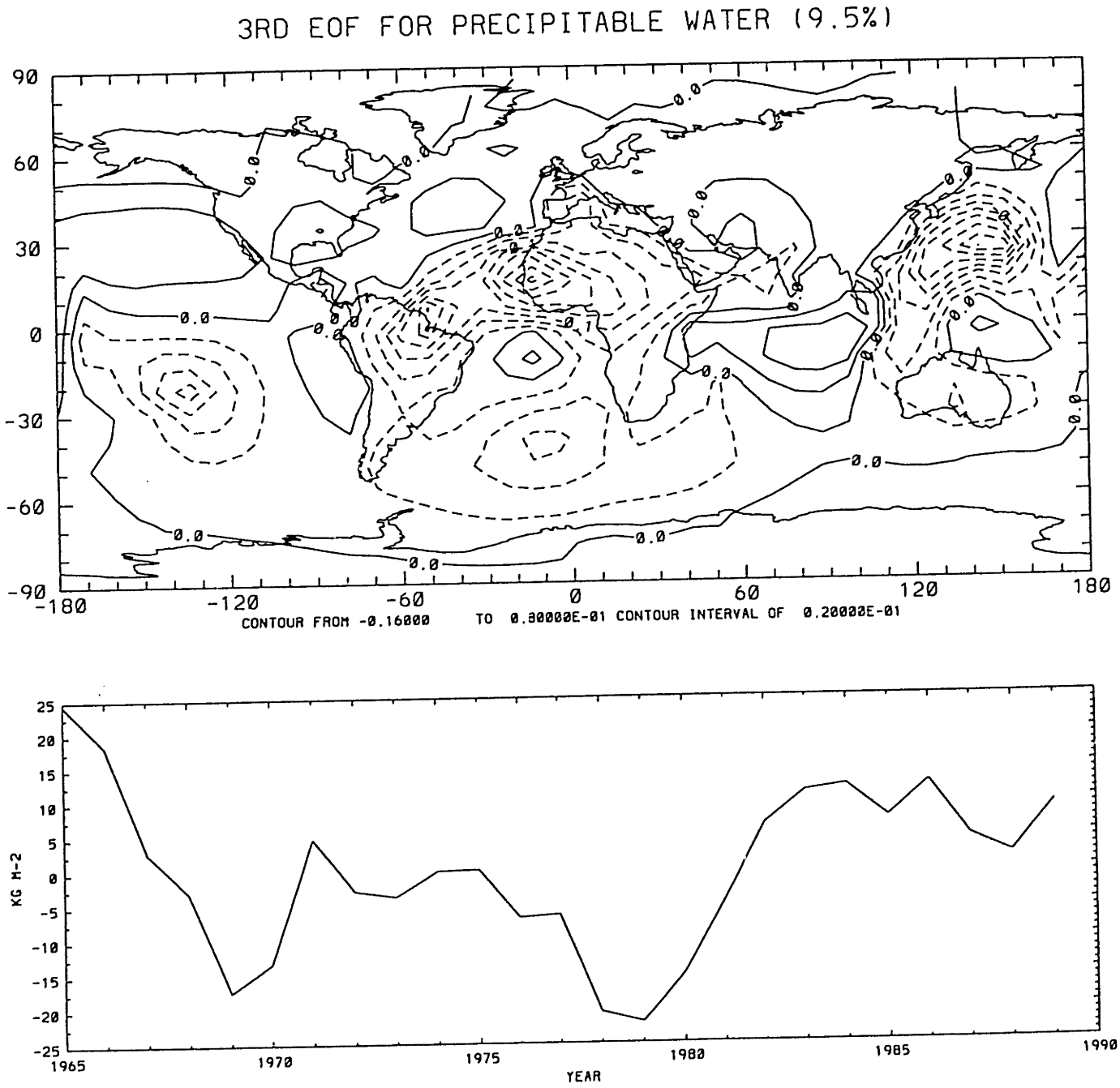
3RD EOF FOR PRECIPITABLE WATER (9.5%)
90
60
30
0
-30
-60
-90
-180
-120
-60
0
60
120
180
0.0
CONTOUR FROM -0.16000 TO 0.80000E-01 CONTOUR INTERVAL OF 0.20000E-01
KG M-2
25
20
15
10
5
0
-5
-10
-15
-20
-25
1965
1970
1975
1980
1985
1990
YEAR

Figure 11.

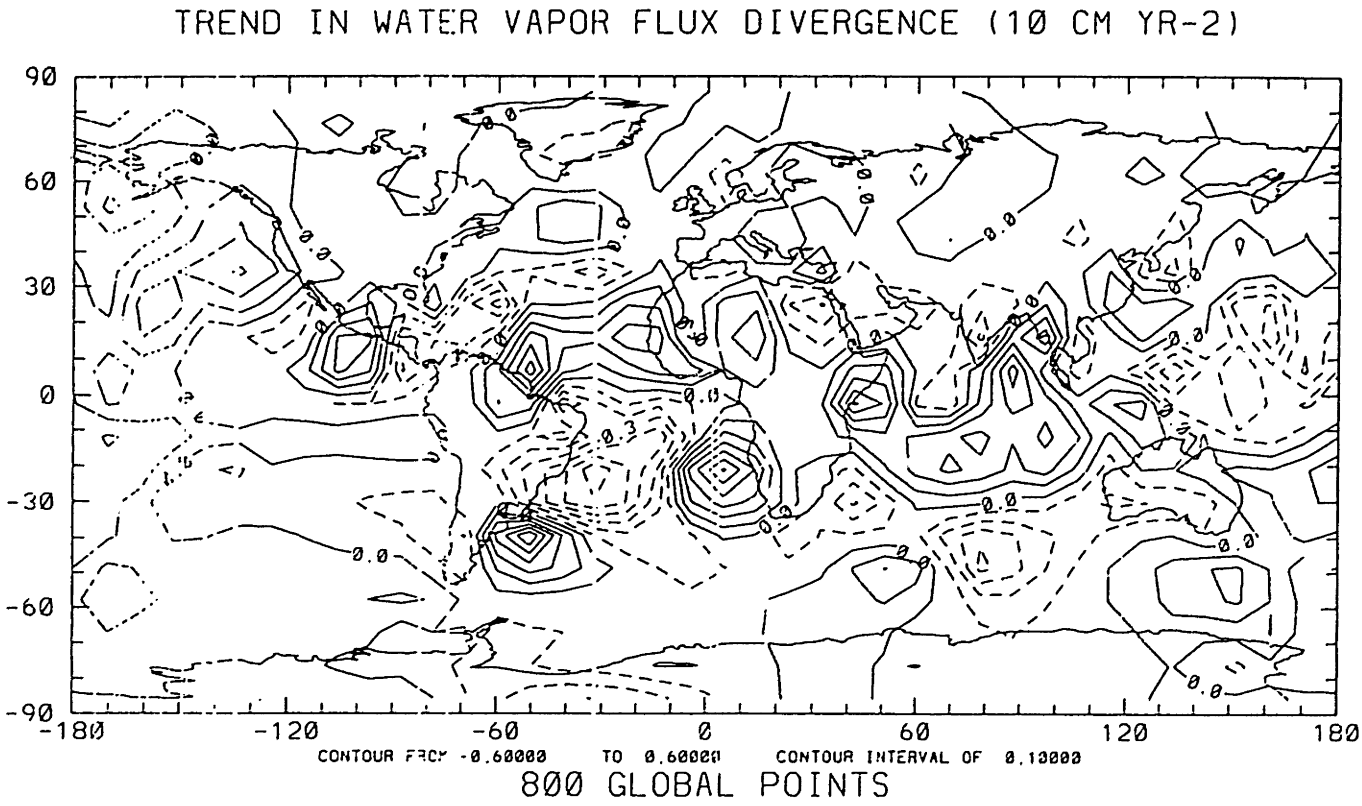
TREND IN WATER VAPOR FLUX DIVERGENCE (10 CM YR-2)
90
60
30
0
-30
-60
-90
-180
-120
-60
0
60
120
180
CONTOUR FROM -0.60000 TO 0.60000 CONTOUR INTERVAL OF 0.10000
800 GLOBAL POINTS

Figure 12.

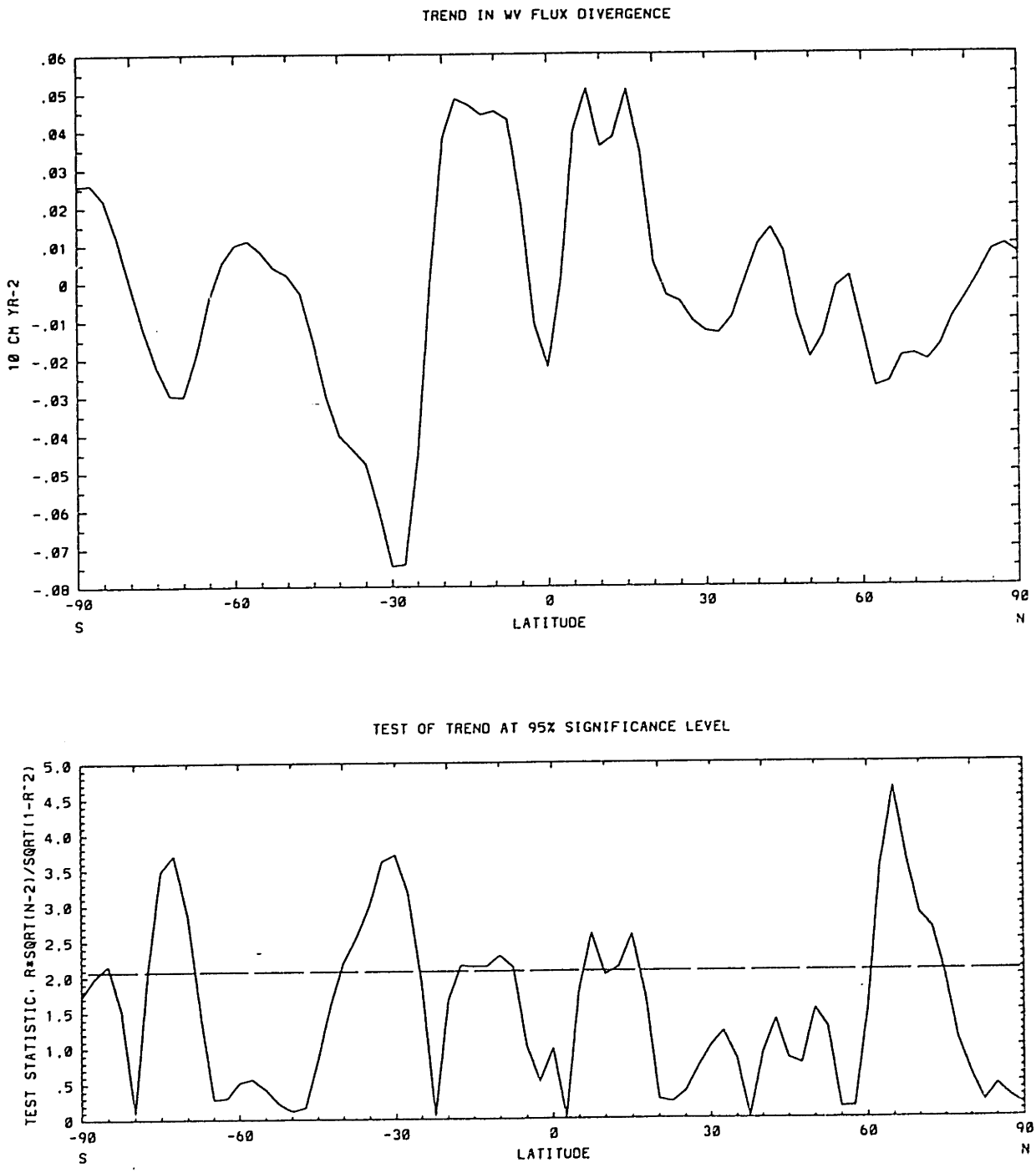
TREND IN WV FLUX DIVERGENCE
10 CM YR-2
.06
.05
.04
.03
.02
.01
0
-.01
-.02
-.03
-.04
-.05
-.06
-.07
-.08
-90
S
-60
-30
0
30
60
90
N
LATITUDE
TEST OF TREND AT 95% SIGNIFICANCE LEVEL
TEST STATISTIC, R*SQRT(N-2)/SQRT(1-R^2)
5.0
4.5
4.0
3.5
3.0
2.5
2.0
1.5
1.0
.5
0
-90
S
-60
-30
0
30
60
90
N
LATITUDE

Figure 13.

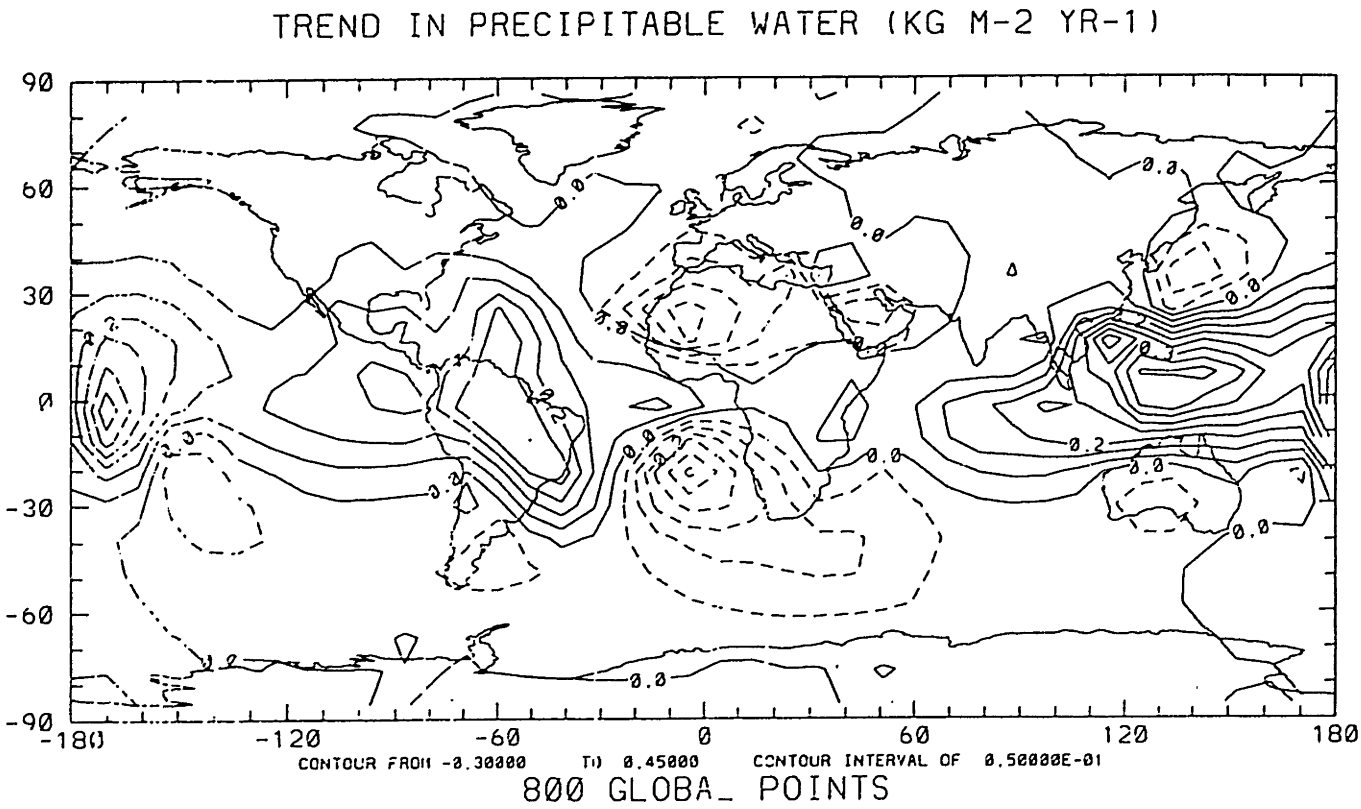
TREND IN PRECIPITABLE WATER (KG M-2 YR-1)
90
60
30
0
-30
-60
-90
-180
-120
-60
0
60
120
180
CONTOUR FROM -0.30000 TO 0.45000 CONTOUR INTERVAL OF 0.50000E-01
800 GLOBAL POINTS

Figure 14.

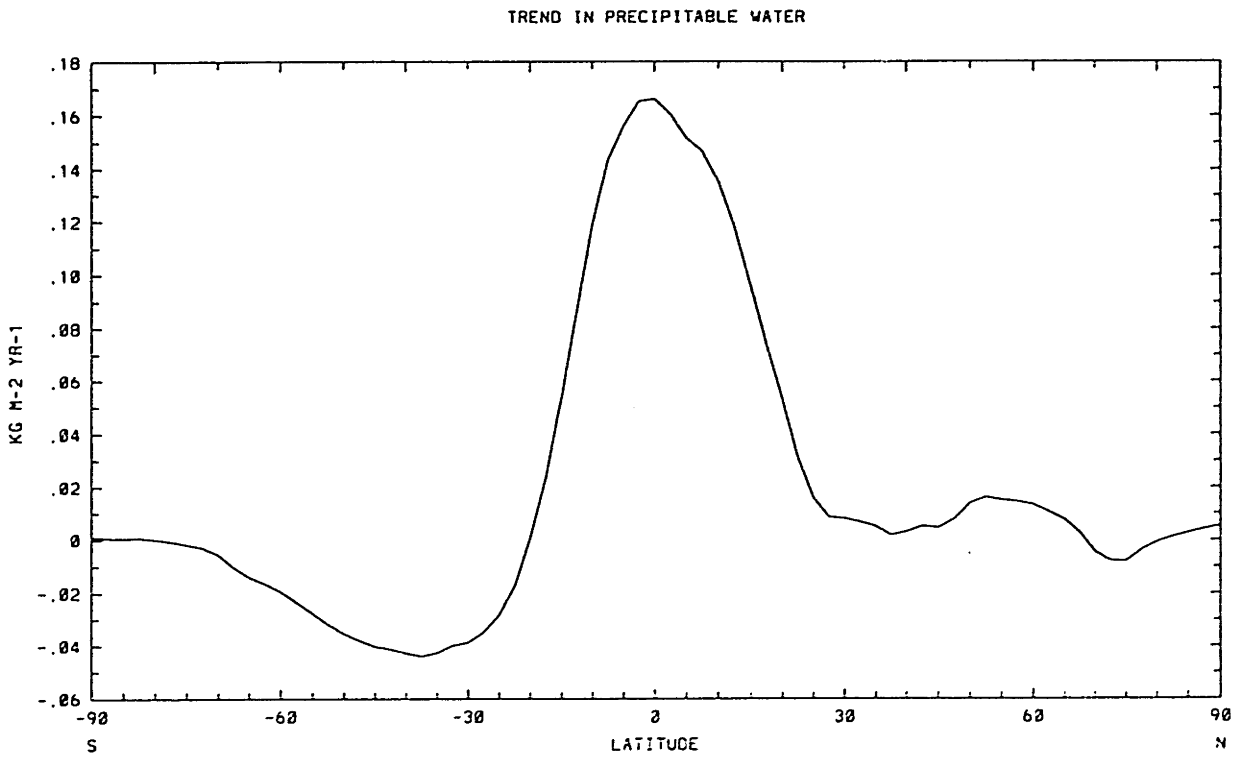
TREND IN PRECIPITABLE WATER
KG M-2 YR-1
.18
.16
.14
.12
.10
.08
.06
.04
.02
0
-.02
-.04
-.06
-90
-60
-30
0
30
60
90
S
LATITUDE
N

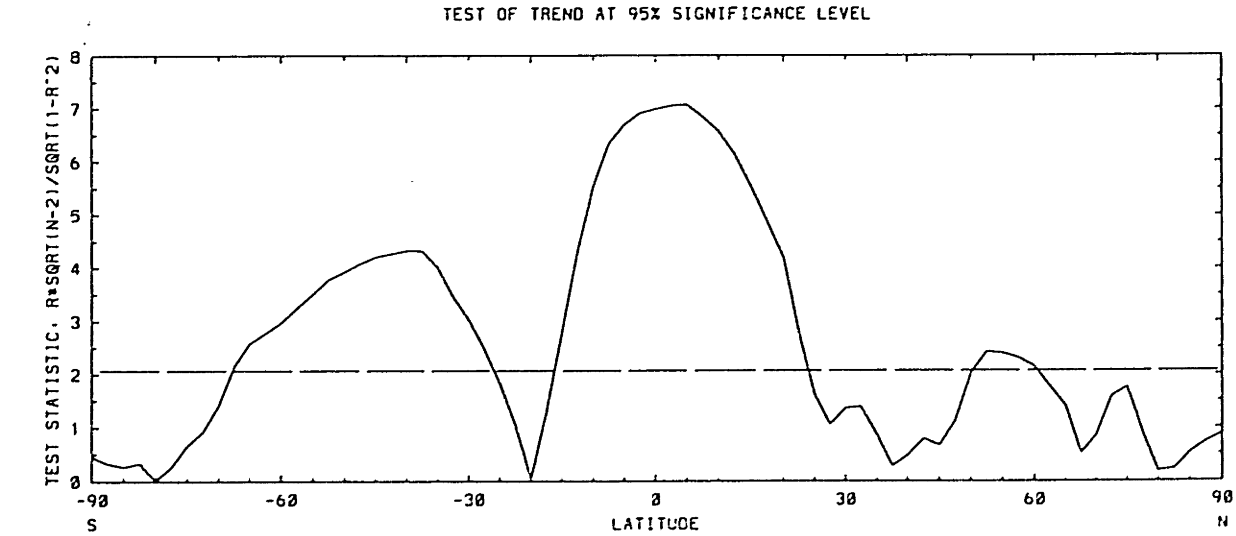
TEST OF TREND AT 95% SIGNIFICANCE LEVEL
TEST STATISTIC, R*SQRT(N-2)/SQRT(1-R^2)
8
7
6
5
4
3
2
1
0
-90
-60
-30
0
30
60
90
S
LATITUDE
N

Figure 15.

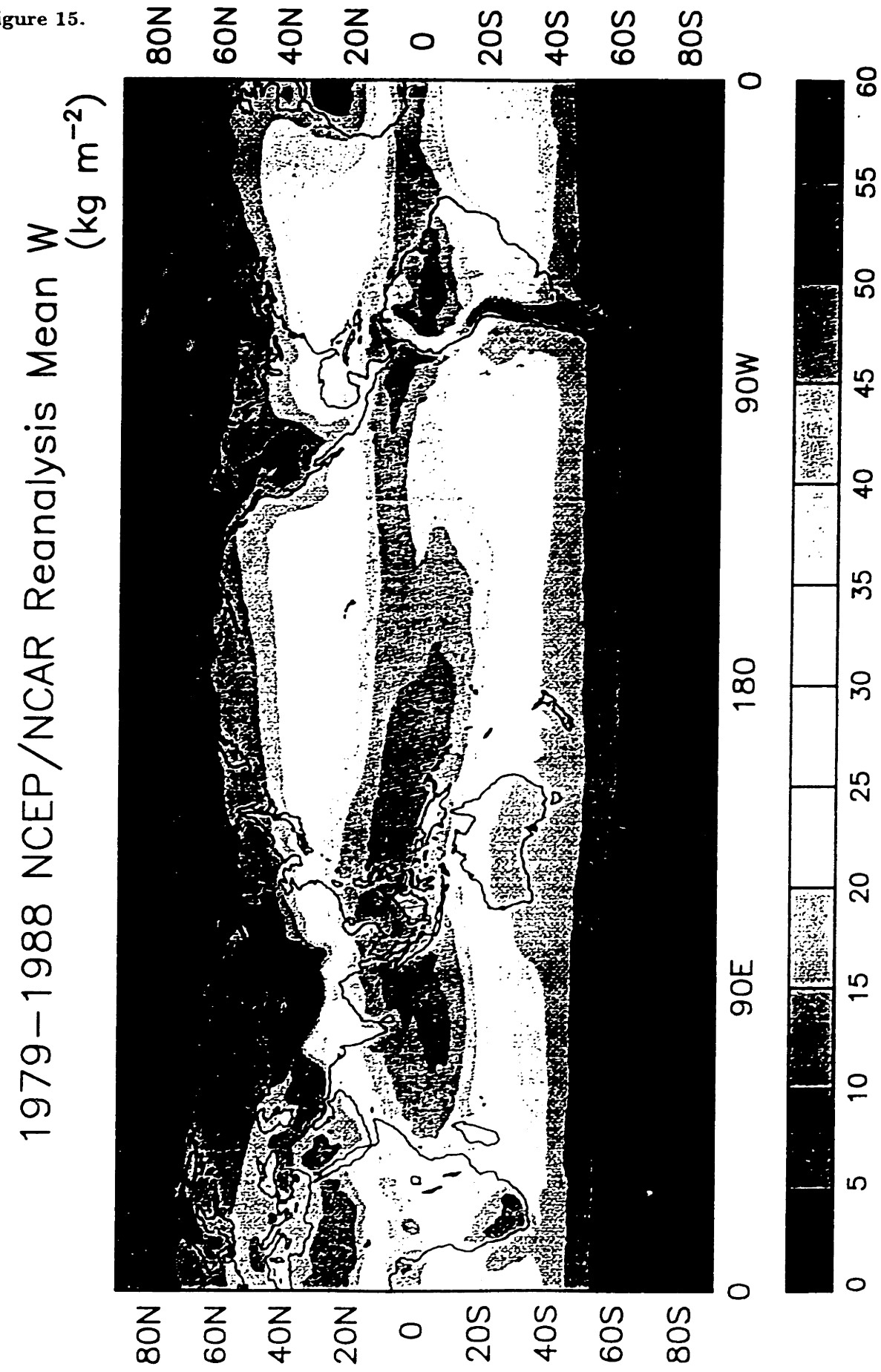
1979–1988 NCEP/NCAR Reanalysis Mean W
(kg m^{-2})
80N
60N
40N
20N
0
20S
40S
60S
80S
0
90E
180
90W
0
0
5
10
15
20
25
30
35
40
45
50
55
60

Figure 16.

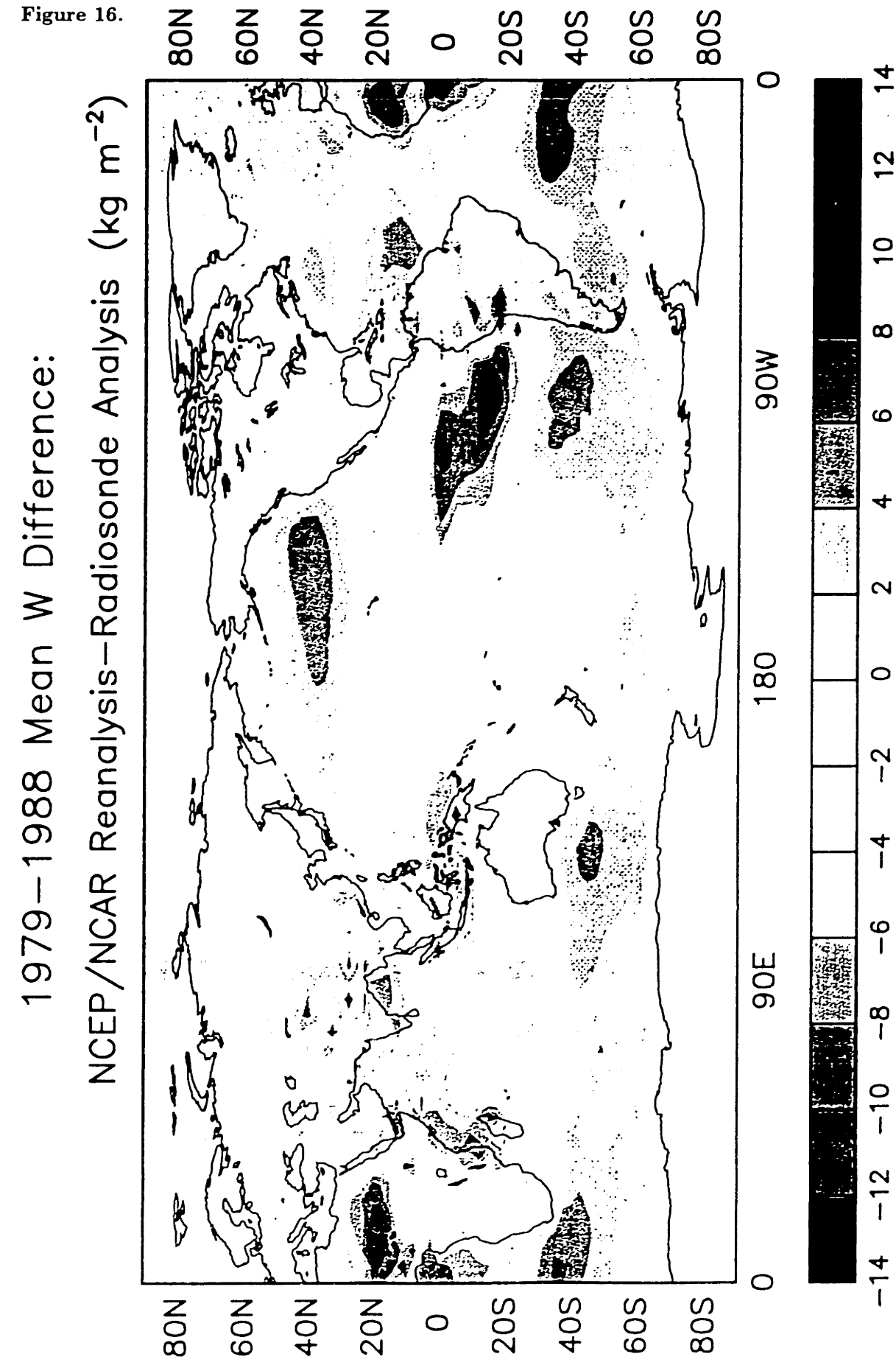
1979–1988 Mean W Difference:
NCEP/NCAR Reanalysis–Radiosonde Analysis (kg m^{-2})
80N
60N
40N
20N
0
20S
40S
60S
80S
0
90E
180
90W
0
−14
−12
−10
−8
−6
−4
−2
0
2
4
6
8
10
12
14

Figure 17. From Oort, 1978.

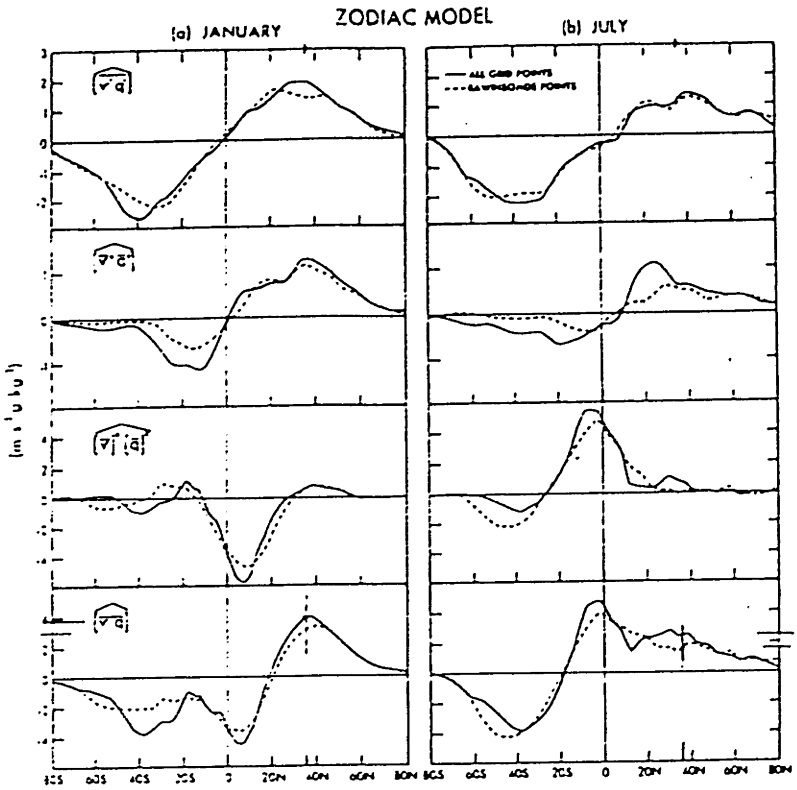

FIG. 13. Meridional profiles of the vertical- and zonal-mean water vapor flux due to transient eddies, due to stationary eddies, due to mean meridional circulations, and due to all types of motions for the full ZODIAC model fields (solid) and for the rawinsonde simulated ZODIAC model fields (dashed) for January (a) and July (b). Units are in m s^{-1} g kg^{-1}.

Figure 18. Globally averaged surface temperature change. From Hansen and Lebedeff, 1987.

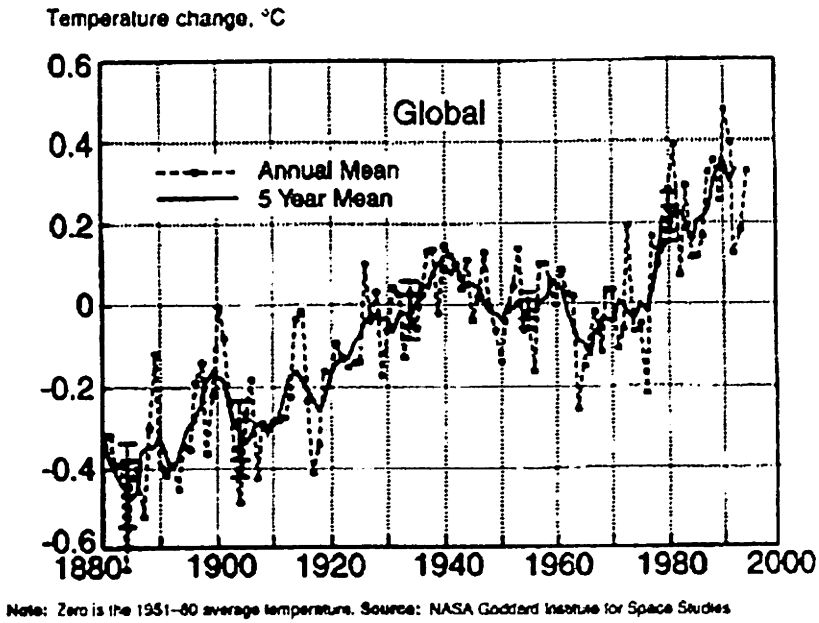

Figure 19.

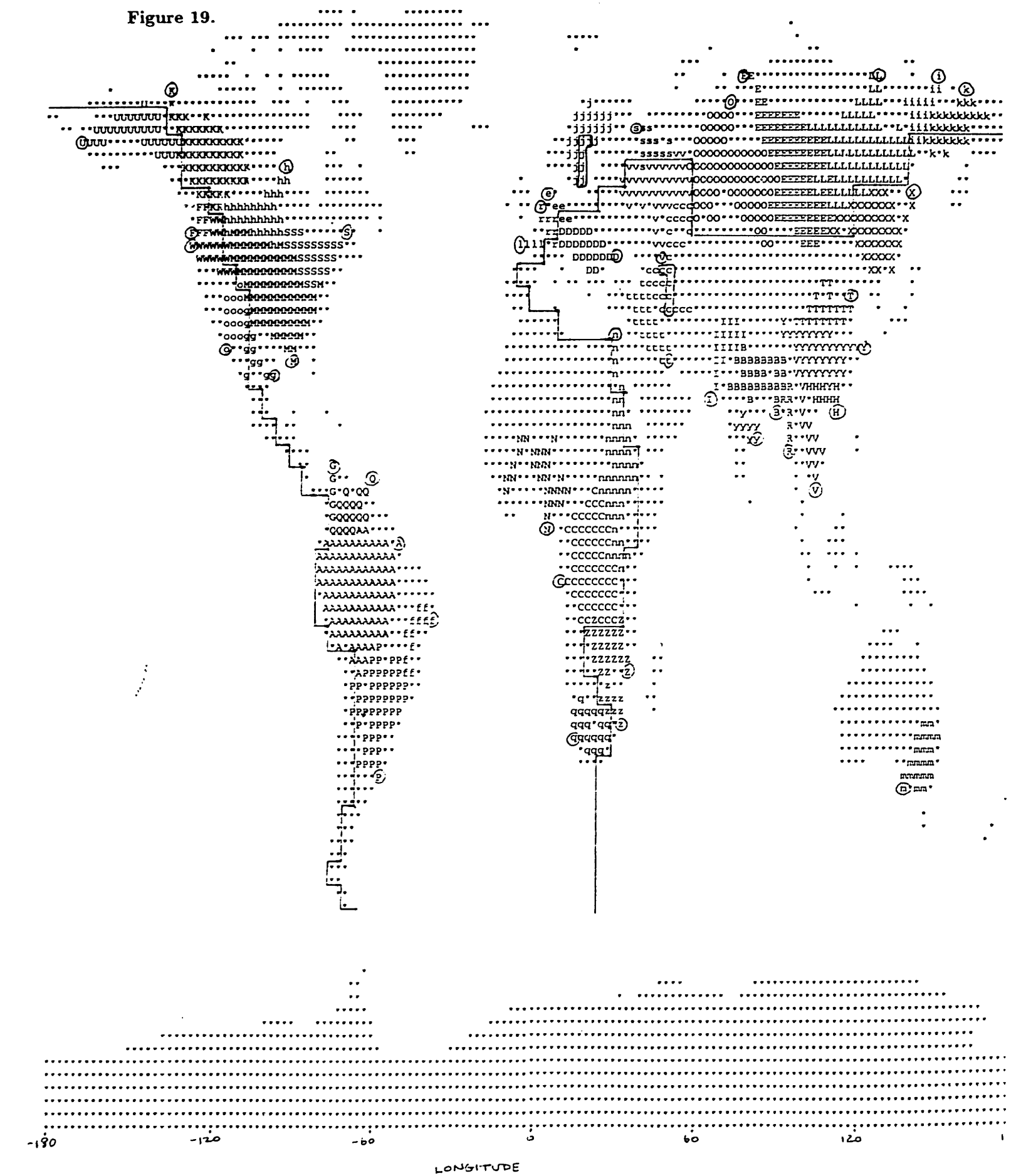

Figure 20.

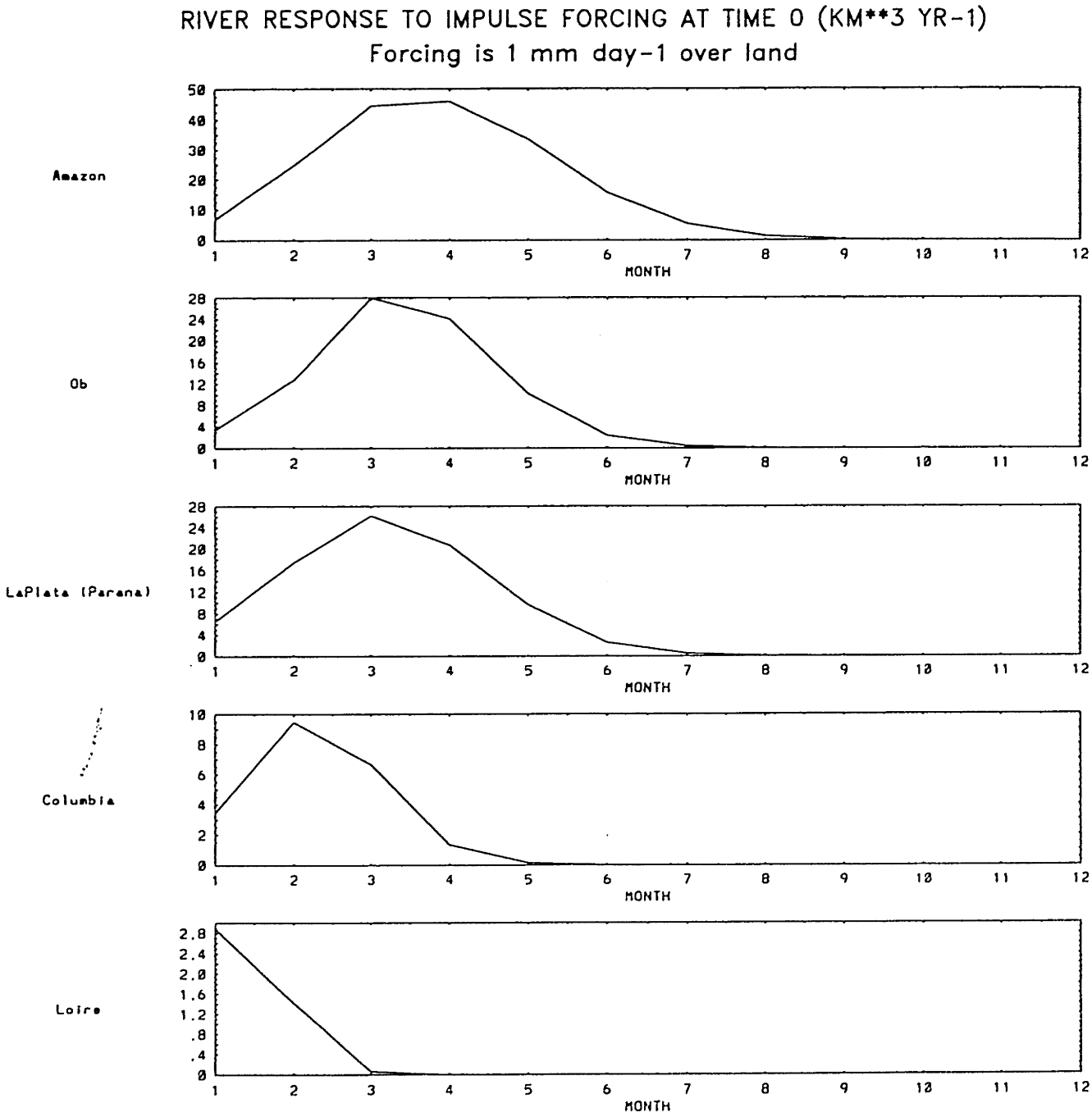
RIVER RESPONSE TO IMPULSE FORCING AT TIME 0 (KM**3 YR-1)
Forcing is 1 mm day-1 over land
Amazon
Ob
LaPlata (Parana)
Columbia
Loire
MONTH

Figure 21. Contour interval is 0.1.

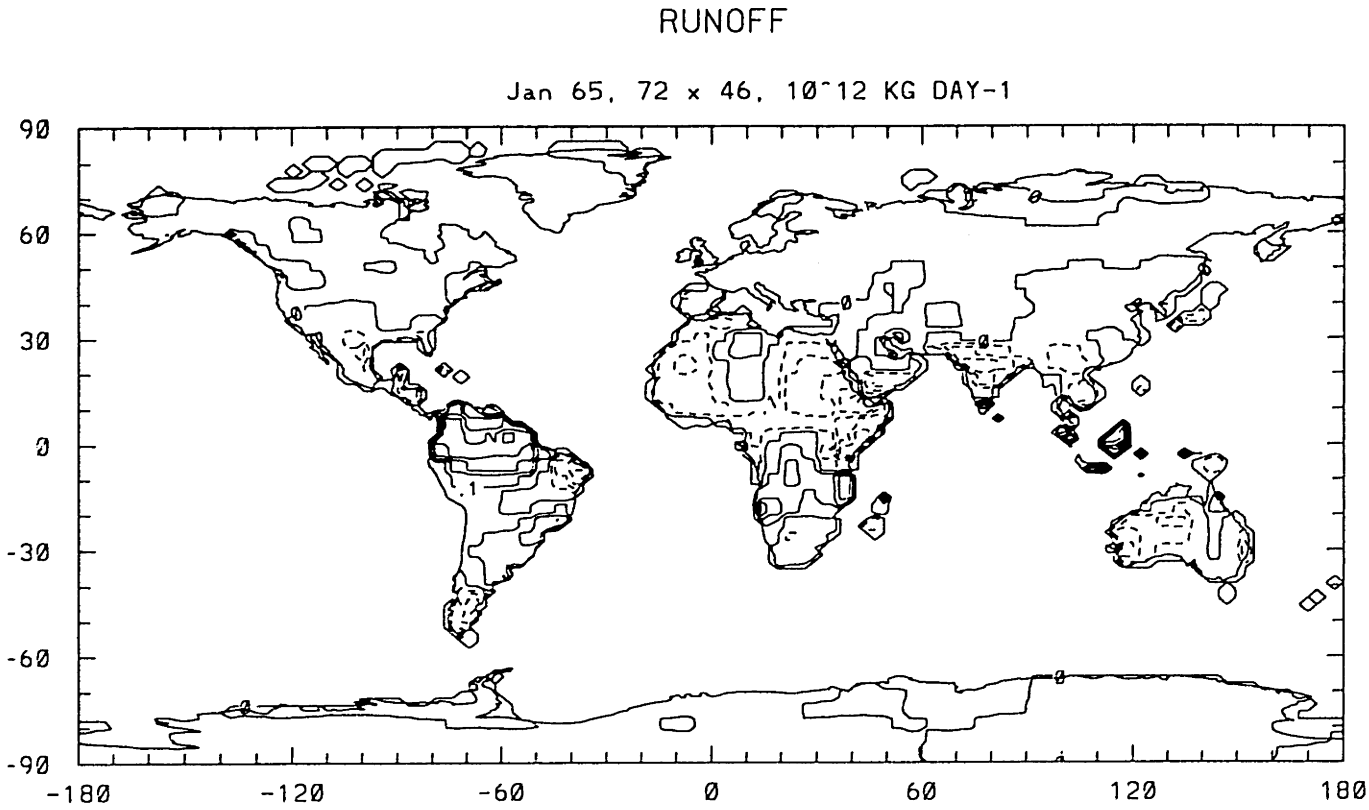

Figure 22a.

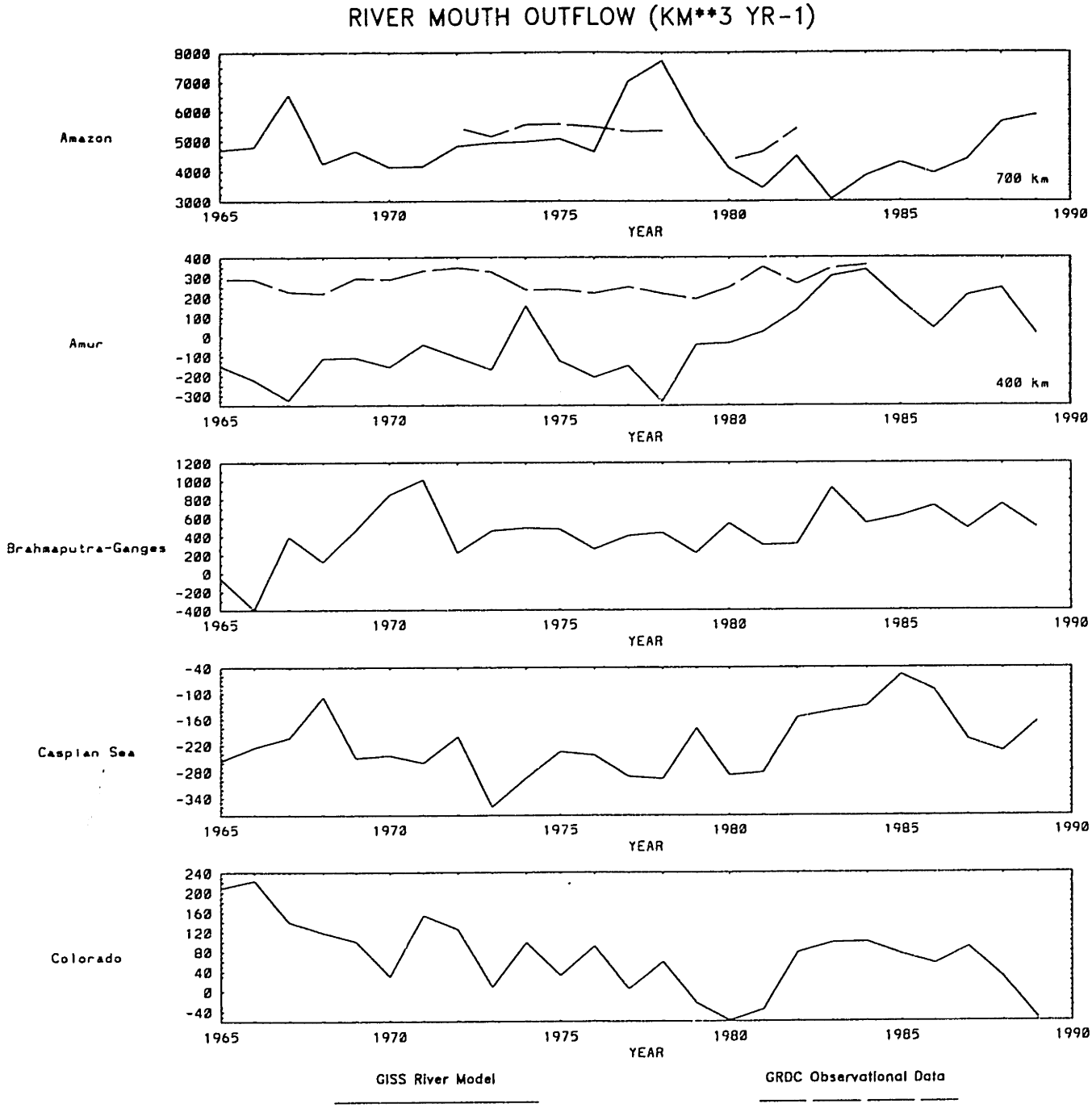
RIVER MOUTH OUTFLOW (KM**3 YR-1)
Amazon
8000
7000
6000
5000
4000
3000
700 km
1965
1970
1975
1980
1985
1990
YEAR
Amur
400
300
200
100
0
-100
-200
-300
400 km
1965
1970
1975
1980
1985
1990
YEAR
Brahmaputra-Ganges
1200
1000
800
600
400
200
0
-200
-400
1965
1970
1975
1980
1985
1990
YEAR
Caspian Sea
-40
-100
-160
-220
-280
-340
1965
1970
1975
1980
1985
1990
YEAR
Colorado
240
200
160
120
80
40
0
-40
1965
1970
1975
1980
1985
1990
YEAR
GISS River Model
GRDC Observational Data

Figure 22b.

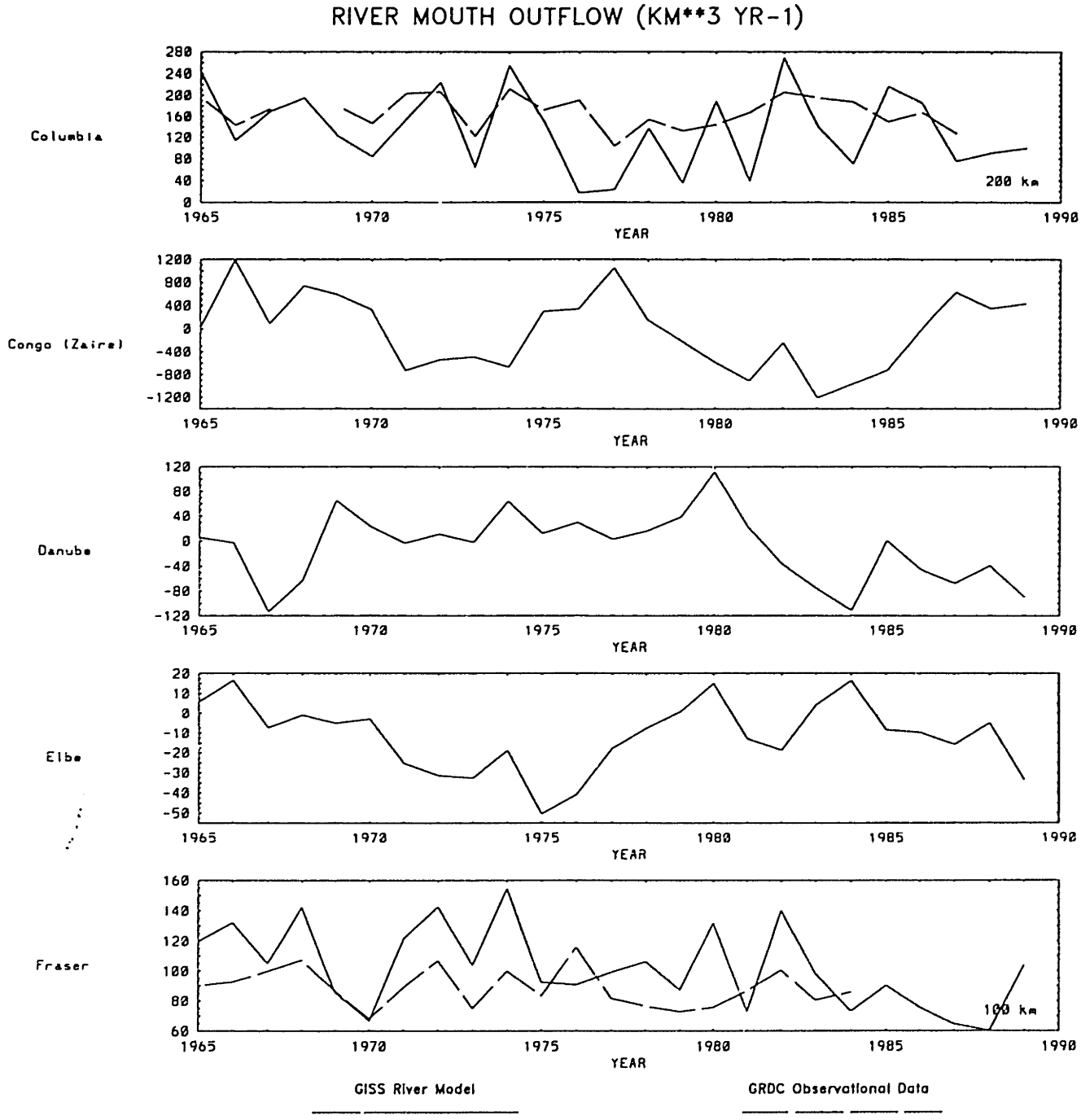
RIVER MOUTH OUTFLOW (KM**3 YR-1)
Columbia
280
240
200
160
120
80
40
0
200 km
1965
1970
1975
1980
1985
1990
YEAR
Congo (Zaire)
1200
800
400
0
-400
-800
-1200
1965
1970
1975
1980
1985
1990
YEAR
Danube
120
80
40
0
-40
-80
-120
1965
1970
1975
1980
1985
1990
YEAR
Elbe
20
10
0
-10
-20
-30
-40
-50
1965
1970
1975
1980
1985
1990
YEAR
Fraser
160
140
120
100
80
60
100 km
1965
1970
1975
1980
1985
1990
YEAR
GISS River Model
GRDC Observational Data

Figure 22c.

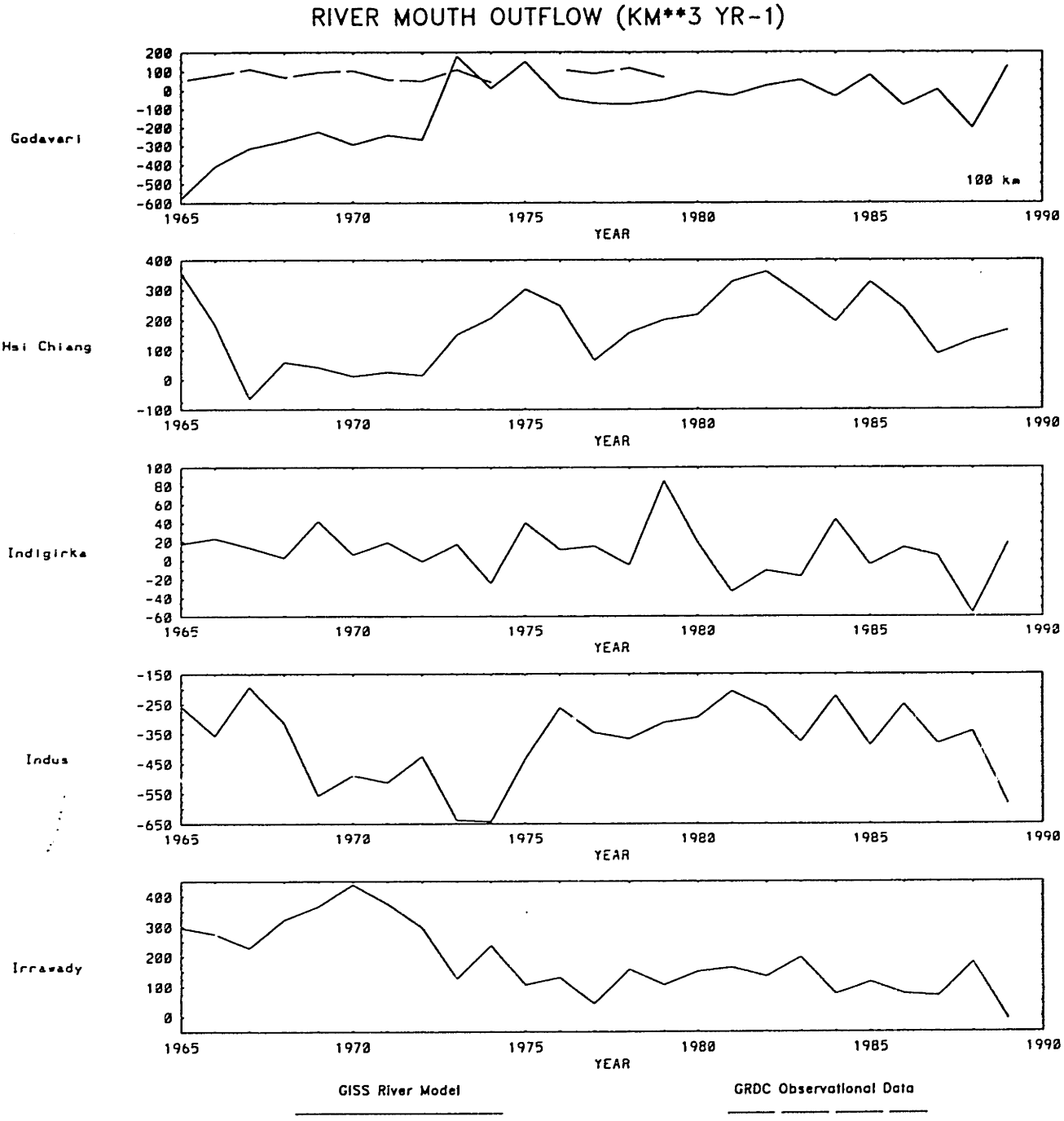
RIVER MOUTH OUTFLOW (KM**3 YR-1)
Godavari
Hsi Chiang
Indigirka
Indus
Irrawady
100 km
YEAR
1965
1970
1975
1980
1985
1990
GISS River Model
GRDC Observational Data

Figure 22d.

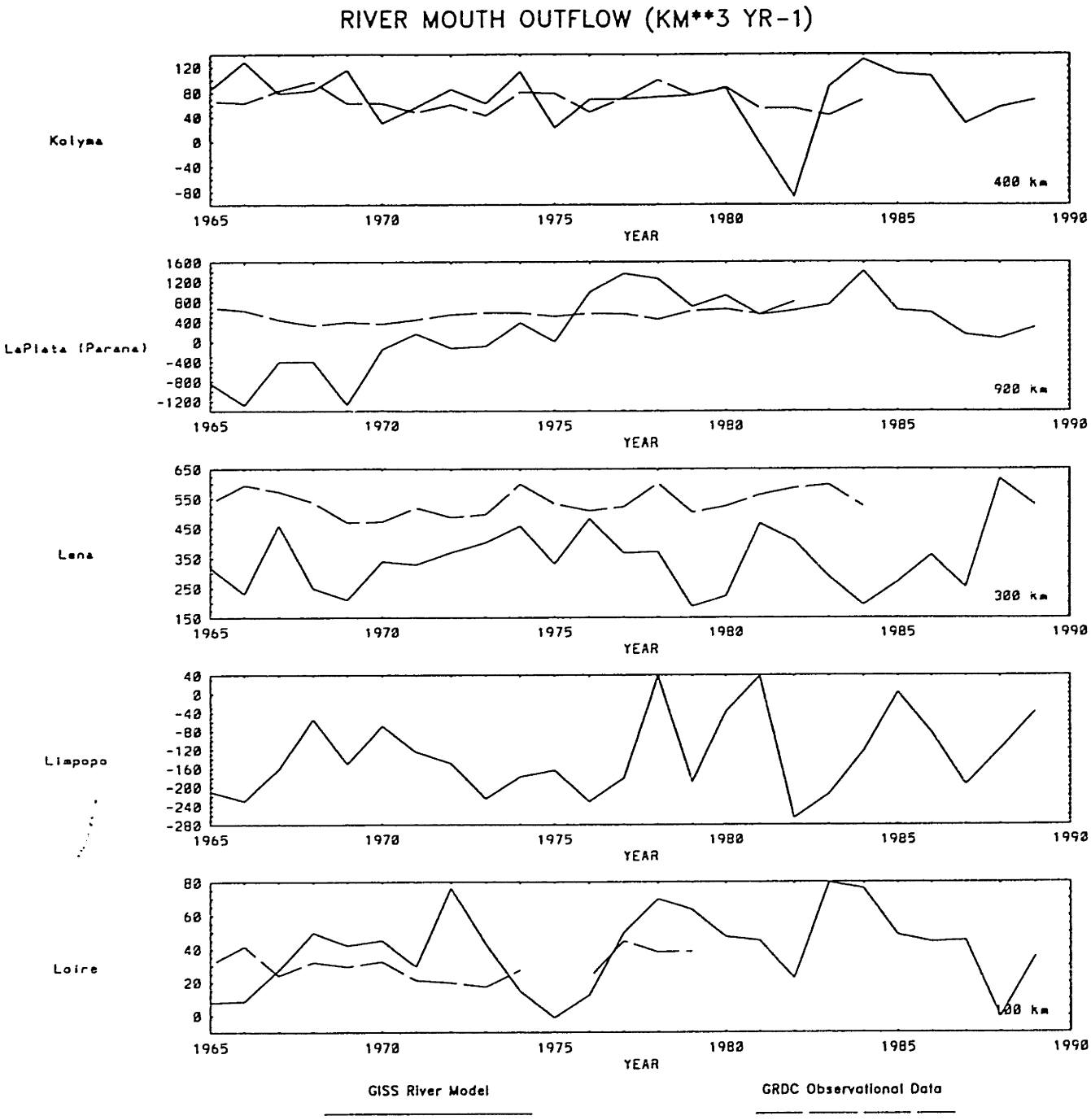
RIVER MOUTH OUTFLOW (KM**3 YR-1)
Kolyma
400 km
LaPlata (Parana)
900 km
Lena
300 km
Limpopo
Loire
100 km
1965
1970
1975
1980
1985
1990
YEAR
GISS River Model
GRDC Observational Data

Figure 22e.

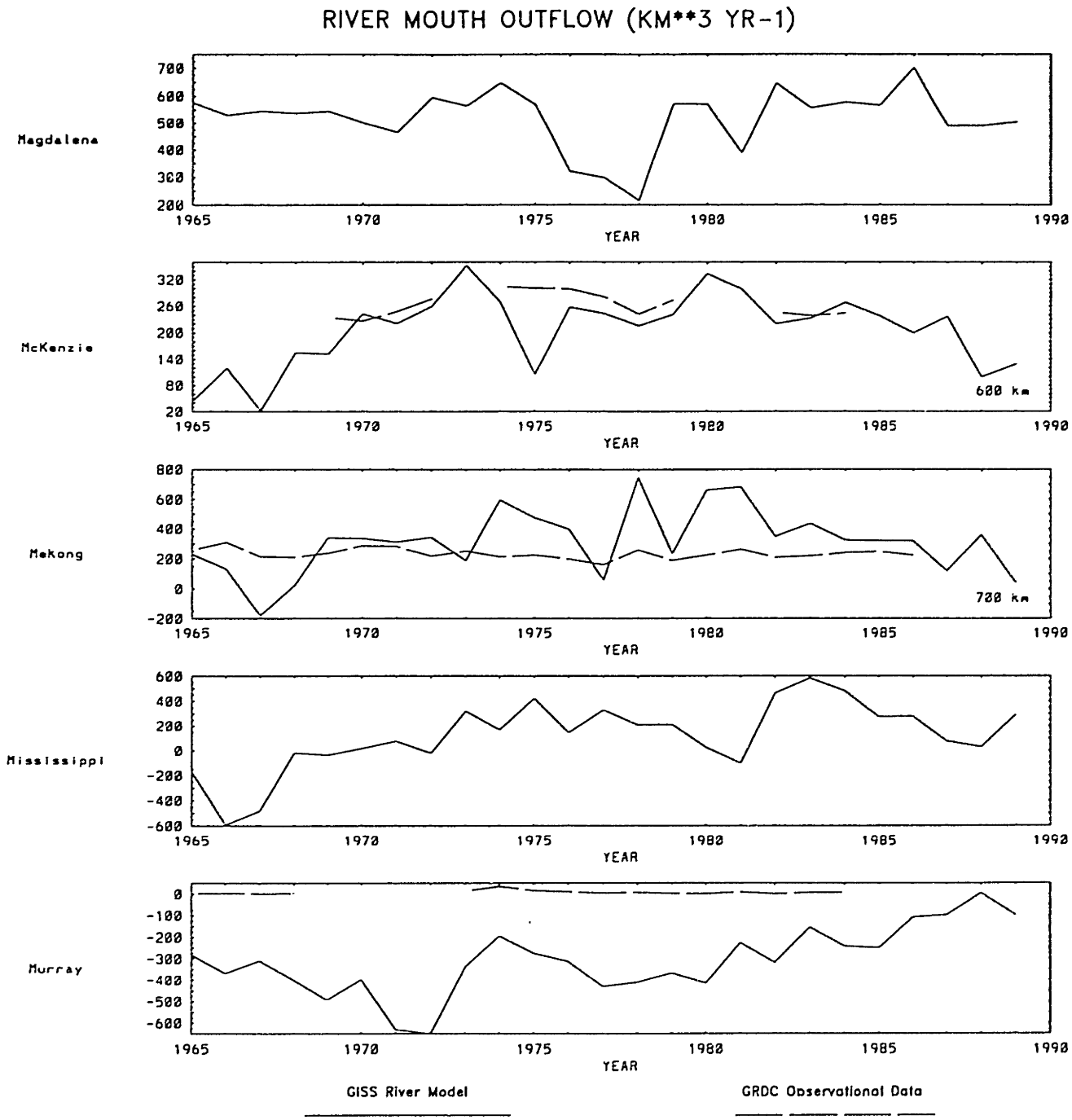
RIVER MOUTH OUTFLOW (KM**3 YR-1)
Magdalena
McKenzie
Mekong
Mississippi
Murray
YEAR
600 km
700 km
GISS River Model
GRDC Observational Data

Figure 22f.

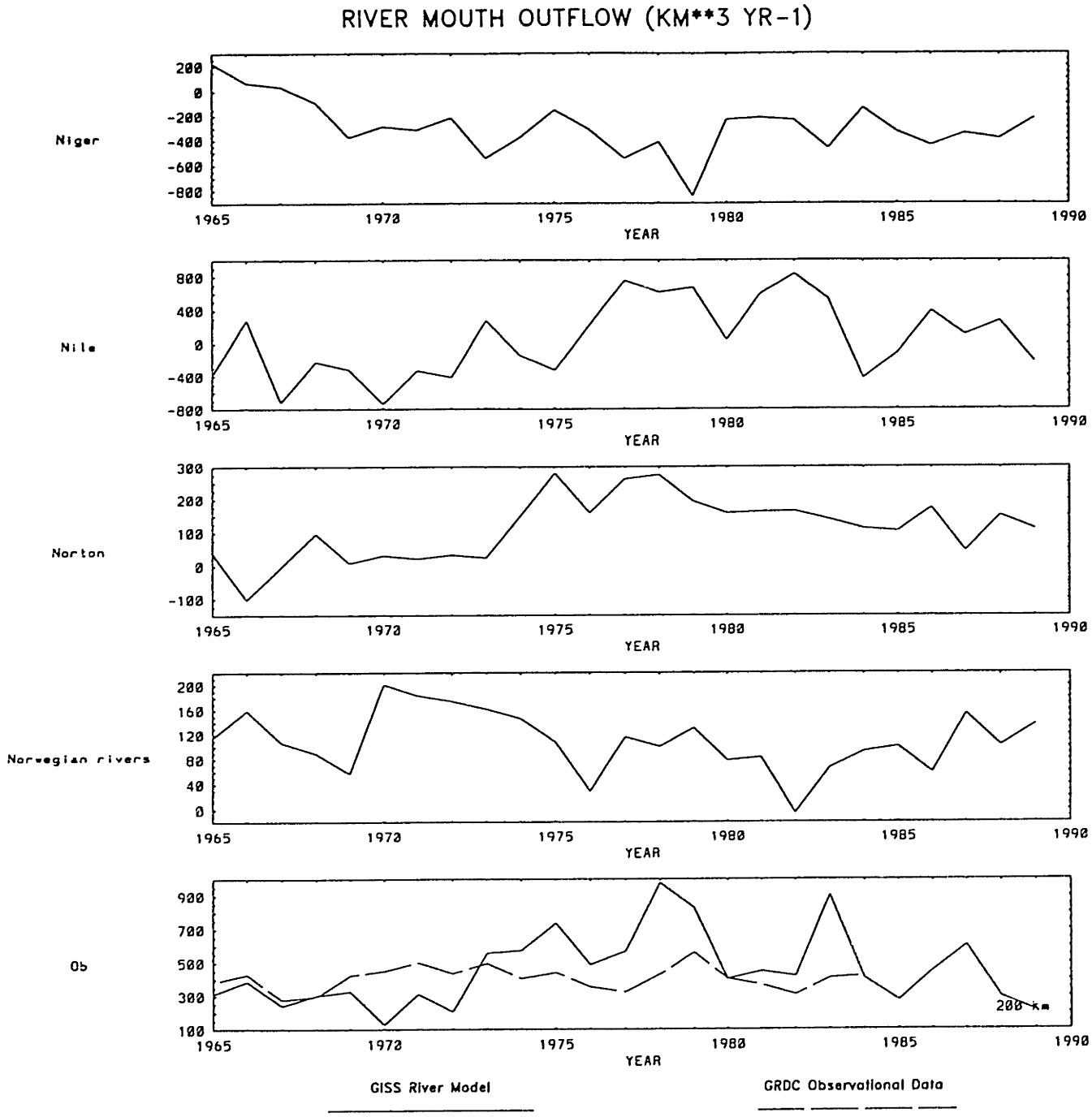
RIVER MOUTH OUTFLOW (KM**3 YR-1)
Niger
200
0
-200
-400
-600
-800
1965
1970
1975
1980
1985
1990
YEAR
Nile
800
400
0
-400
-800
1965
1970
1975
1980
1985
1990
YEAR
Norton
300
200
100
0
-100
1965
1970
1975
1980
1985
1990
YEAR
Norwegian rivers
200
160
120
80
40
0
1965
1970
1975
1980
1985
1990
YEAR
Ob
900
700
500
300
100
200 km
1965
1970
1975
1980
1985
1990
YEAR
GISS River Model
GRDC Observational Data

Figure 22g.

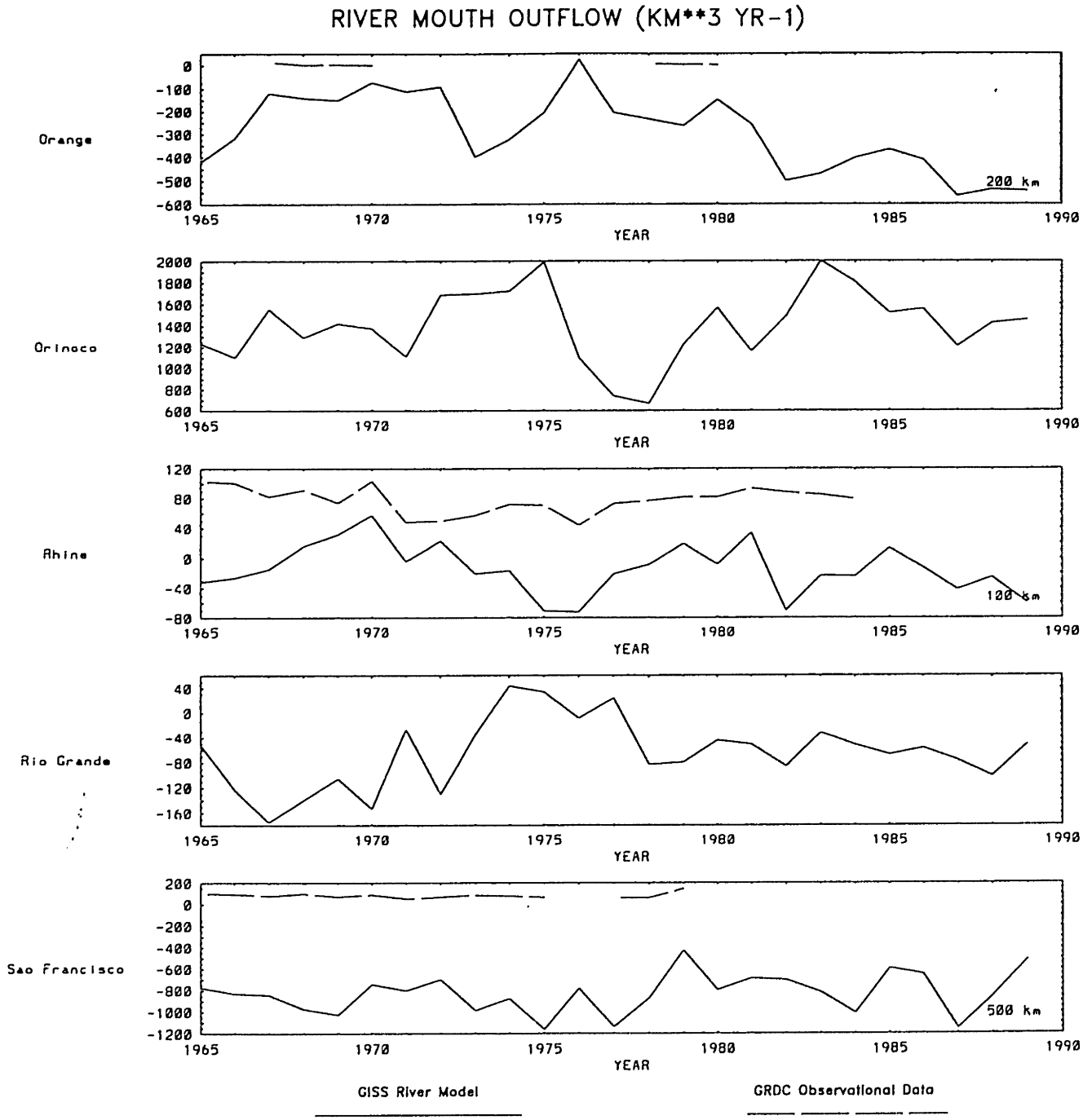
RIVER MOUTH OUTFLOW (KM**3 YR-1)
Orange
0
-100
-200
-300
-400
-500
-600
200 km
1965
1970
1975
1980
1985
1990
YEAR
Orinoco
2000
1800
1600
1400
1200
1000
800
600
YEAR
Rhine
120
80
40
0
-40
-80
100 km
YEAR
Rio Grande
40
0
-40
-80
-120
-160
YEAR
Sao Francisco
200
0
-200
-400
-600
-800
-1000
-1200
500 km
YEAR
GISS River Model
GRDC Observational Data

Figure 22h.

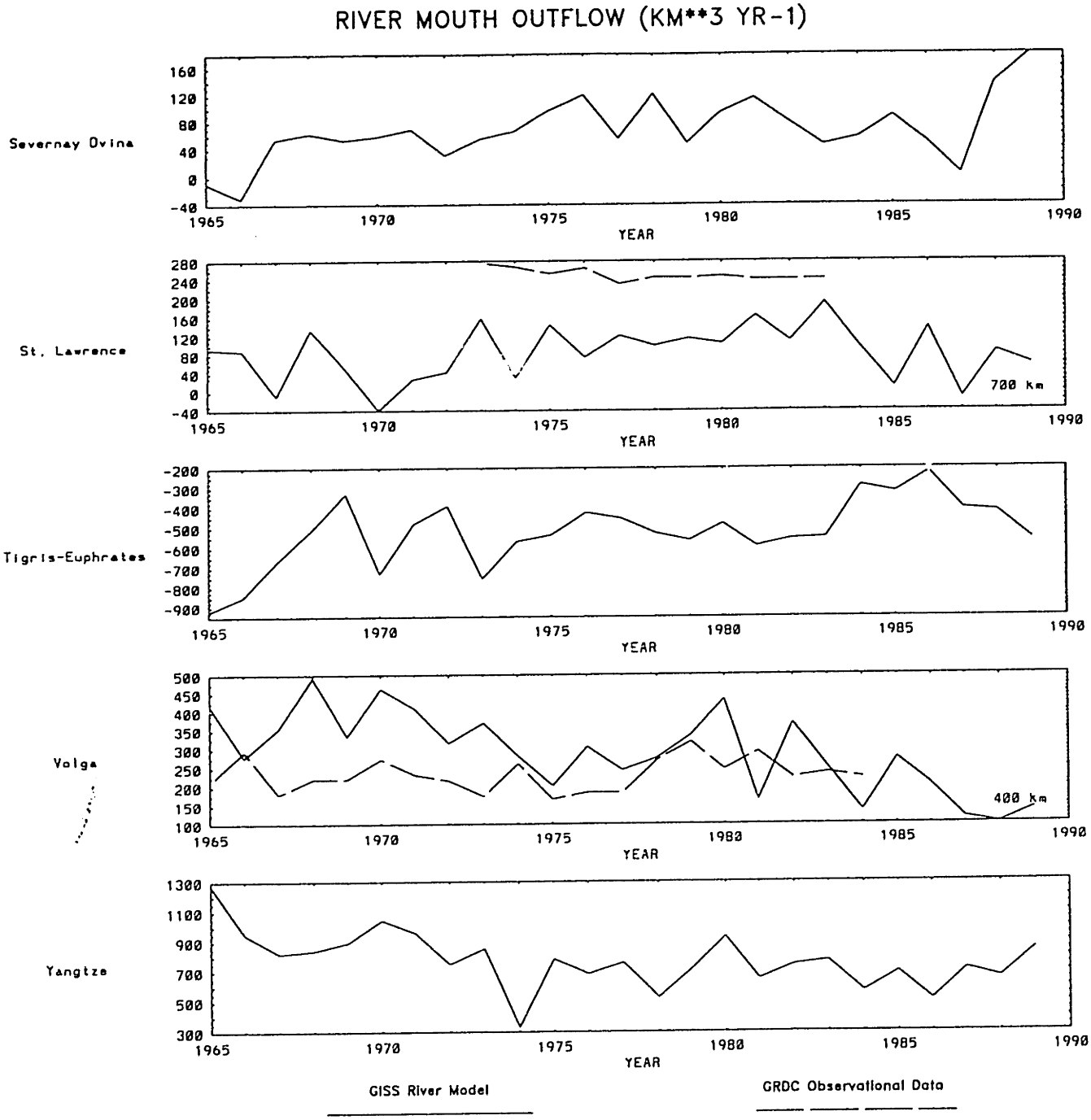
RIVER MOUTH OUTFLOW (KM**3 YR-1)
Severnay Dvina
160
120
80
40
0
-40
1965
1970
1975
1980
1985
1990
YEAR
St. Lawrence
280
240
200
160
120
80
40
0
-40
700 km
YEAR
Tigris-Euphrates
-200
-300
-400
-500
-600
-700
-800
-900
YEAR
Volga
500
450
400
350
300
250
200
150
100
400 km
YEAR
Yangtze
1300
1100
900
700
500
300
YEAR
GISS River Model
GRDC Observational Data

Figure 22i.

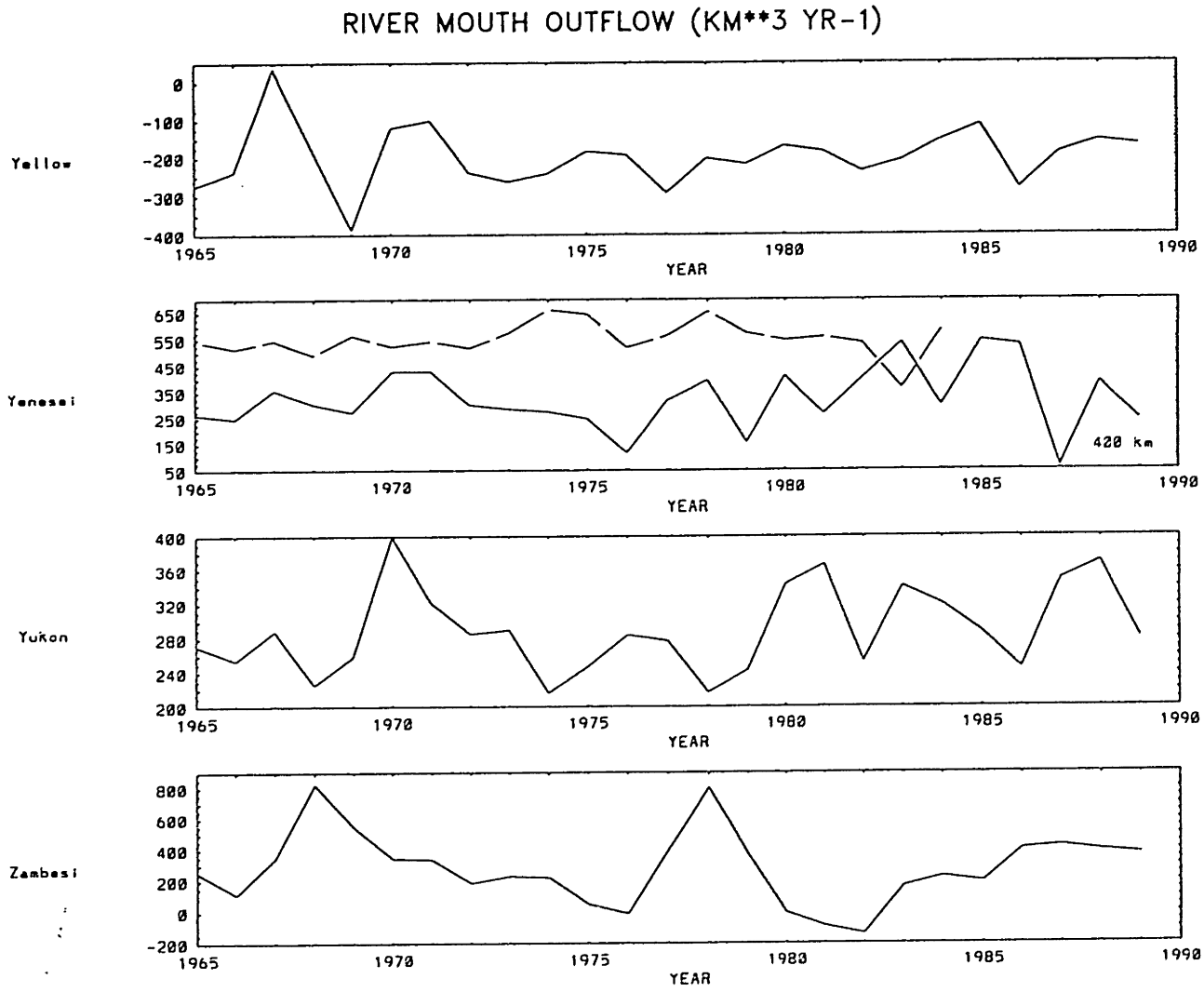
RIVER MOUTH OUTFLOW (KM**3 YR-1)
Yellow
0
-100
-200
-300
-400
1965
1970
1975
1980
1985
1990
YEAR
Yenesei
650
550
450
350
250
150
50
420 km
YEAR
Yukon
400
360
320
280
240
200
YEAR
Zambesi
800
600
400
200
0
-200
YEAR
GISS River Model
GRDC Observational Data

Figure 23.

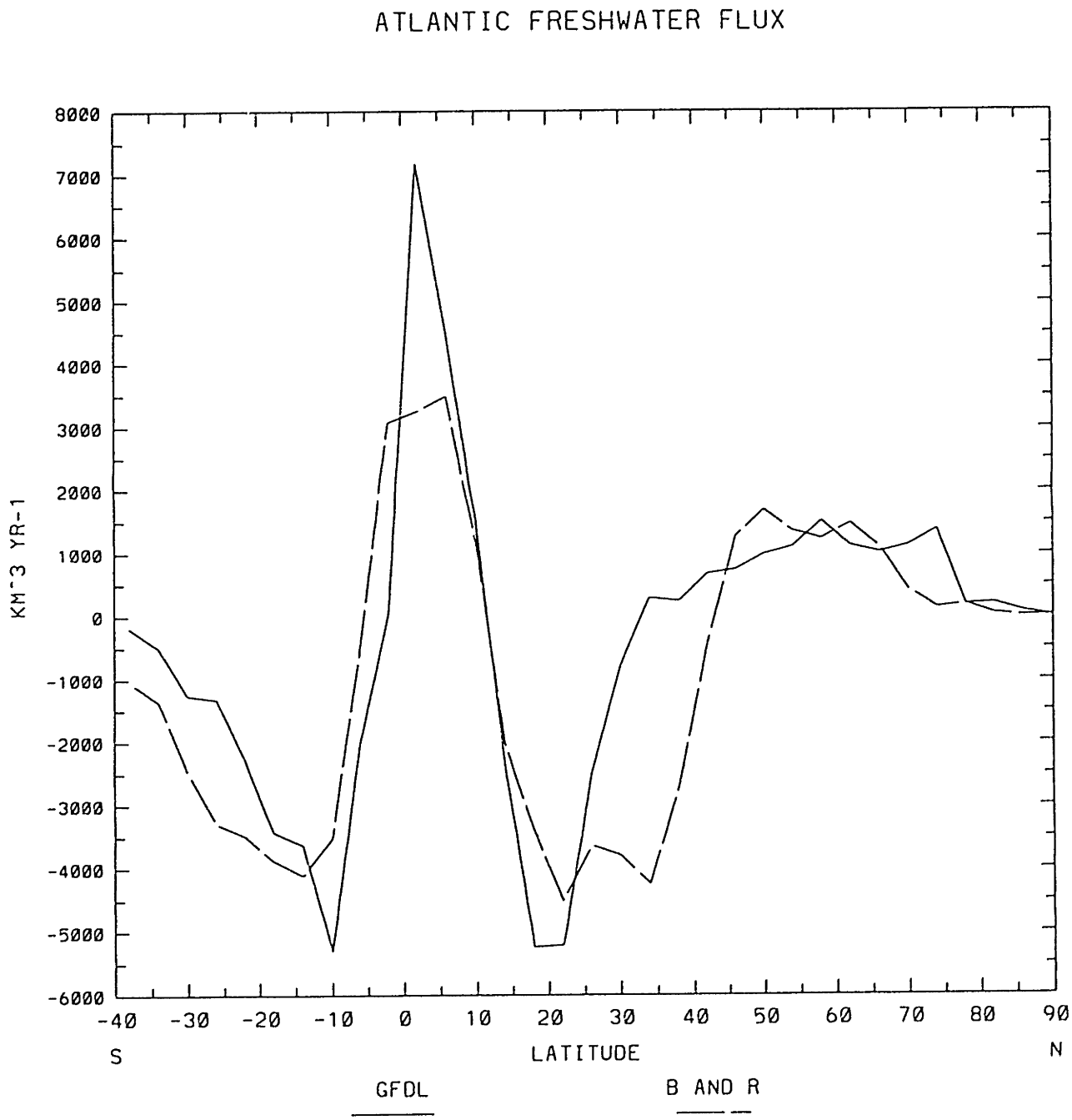
ATLANTIC FRESHWATER FLUX
KM^3 YR-1
8000
7000
6000
5000
4000
3000
2000
1000
0
-1000
-2000
-3000
-4000
-5000
-6000
-40 -30 -20 -10 0 10 20 30 40 50 60 70 80 90
S
LATITUDE
N
GFDL
B AND R

Appendix A: Divergence Calculation

For boxes centered on each gridpoint (i,j), as shown in Fig. A-1, below, the following were defined:

L_S = the length of the southern side of the box.

L_N = the length of the northern side of the box.

L_{EW} = the length of the eastern and western sides of each box.

The mass leaving through the northern edge of the box is:

$F_N = (Q_\phi(i,j) + Q_\phi(i,j+1)) * \frac{L_N}{2}$

and the mass entering through the southern edge of the box is:

$F_S = (Q_\phi(i,j) + Q_\phi(i,j-1)) * \frac{L_S}{2}$

The mass entering through the western edge of the box is:

$F_W = (Q_\lambda(i,j) + Q_\lambda(i+1,j)) * \frac{L_{EW}}{2}$

and the mass leaving through the eastern edge of the box is:

$F_E = (Q_\lambda(i,j) + Q_\lambda(i-1,j)) * \frac{L_{EW}}{2}$

The total mass leaving the box per unit time is:

$M = ((F_N - F_S) + (F_E - F_W))$

To get the flux per unit area, we can divide by the area of the box, which is approximated as:

$A = L_{EW} * \frac{L_S + L_N}{2}$

The divergence is:

M/A

Though the calculation performed here does not take earth's curvature into account, the annual mean divergence field closely resembles that obtained by Peixoto and Oort (1992) for the period 1963-1973. Their results are shown in Fig. A-2, and may be compared with the smoothed annual mean divergence shown in Fig.E-27.

Figure A-2. Annual mean water vapor flux divergence. From Peixoto and Oort (1992). Years included are 1963-1973.

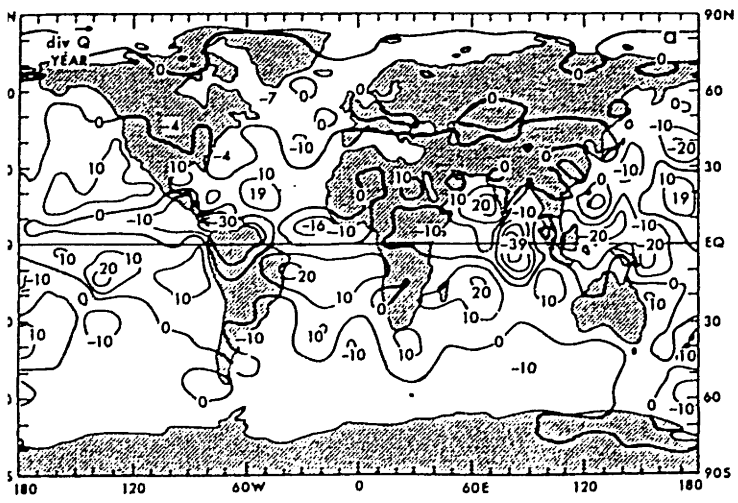

Figure A-1.

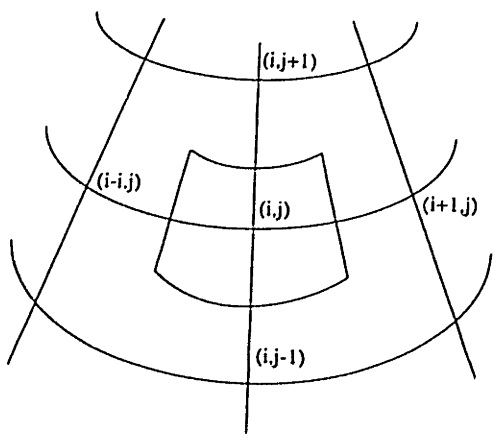

Appendix B: Southern Oscillation Index

The SOI is calculated from Tahiti and Darwin Sea-Level Pressure (SLP) as follows (Chelliah, M., 1990, *J. Climate*, 3, 158-160):

$$SOI(month, year) = \frac{(T(month, year) - D(month, year))}{S} \times 10.$$

where:

T and D are anomalies of Tahiti and Darwin SLP that have been normalized by the standard deviation of the monthly values of the respective index for all months combined for the years 1951 to 1980.

S is the standard deviation of the numerator for all months combined for the years 1951 to 1980.

The factor of 10 is arbitrary and appears in some listings of the SOI. Annual mean SOI was assumed to be a simple average of monthly values. The following data is courtesy of the NCEP Climate Prediction Center and was accessed through the Joint Institute for the Study of the Atmosphere and Ocean (JISAO) Climate Data Archive.

Note that the time period over which the SOI is normalized is different than the period spanned by the GFDL Atmospheric Circulation Tape Library, and the normalization is performed for monthly rather than annual values. Since the purpose of the SOI in this paper is simply to indicate that a particular time series of EOF coefficients is associated with the El Nino oscillation, the rather cavalier normalization is considered adequate.

Annual mean values for the SOI are shown on the following page.

Table B.1: **Southern Oscillation Index (SOI)**

Year	Index
1965	-8
1966	-5
1967	2
1968	1
1969	-6
1970	2
1971	10
1972	-8
1973	5
1974	10
1975	12
1976	0
1977	-10
1978	-3
1979	-1
1980	-3
1981	0
1982	-13
1983	-11
1984	-1
1985	0
1986	-3
1987	-13
1988	7
1989	5

Appendix C: Freshwater Flux Results (sverdrups)

Table C.1: **Atlantic Freshwater Fluxes (sverdrups)**

Latitude	River runoff		Land runoff		Ocean P-E		All	
	Mean	Std. Dev.	Mean	Std. Dev.	Mean	Std. Dev.	Mean	Std. Dev.
90	0.000	0.000	0.000	0.001	0.000	0.000	0.000	0.001
86	0.000	0.000	0.002	0.003	0.000	0.000	0.002	0.003
82	0.000	0.000	0.006	0.003	0.000	0.000	0.006	0.003
78	0.000	0.000	0.006	0.002	0.000	0.001	0.006	0.003
74	0.036	0.007	0.005	0.003	0.003	0.001	0.044	0.009
70	0.009	0.003	0.017	0.003	0.010	0.002	0.036	0.005
66	0.002	0.001	0.014	0.003	0.016	0.003	0.032	0.005
62	0.003	0.002	0.016	0.004	0.016	0.004	0.035	0.007
58	0.010	0.003	0.024	0.006	0.013	0.003	0.048	0.006
54	0.000	0.001	0.019	0.006	0.016	0.002	0.035	0.007
50	0.003	0.002	0.008	0.009	0.021	0.005	0.031	0.011
46	0.001	0.001	0.015	0.009	0.008	0.004	0.023	0.011
42	0.000	0.000	0.015	0.012	0.006	0.005	0.021	0.014
> 40	0.064	0.011	0.108	0.011	0.147	0.028	0.319	0.034
38	0.000	0.000	0.019	0.011	-.012	0.008	0.007	0.014
34	0.000	0.000	0.020	0.013	-.011	0.004	0.009	0.015
30	0.004	0.009	-.010	0.017	-.019	0.008	-.025	0.020
26	-.002	0.002	-.059	0.016	-.018	0.010	-.079	0.016
22	0.000	0.000	-.134	0.018	-.031	0.009	-.165	0.018
18	0.000	0.000	-.115	0.023	-.051	0.011	-.166	0.028
14	0.016	0.003	-.086	0.023	-.005	0.010	-.074	0.023
10	0.045	0.010	0.002	0.017	0.002	0.009	0.048	0.021
6	0.000	0.000	0.064	0.017	0.078	0.016	0.143	0.030
2	0.144	0.033	0.036	0.017	0.048	0.017	0.228	0.046
0 to 40	0.207	0.029	-.018	0.046	-.263	0.067	-.074	0.073
-2	0.000	0.000	-.020	0.021	0.021	0.012	0.001	0.022
-6	-.001	0.020	-.038	0.019	-.025	0.011	-.064	0.025
-10	-.026	0.006	-.086	0.014	-.056	0.012	-.168	0.025
-14	0.000	0.000	-.107	0.019	-.008	0.003	-.115	0.020
-18	0.000	0.000	-.083	0.018	-.026	0.005	-.109	0.020
-22	0.000	0.000	-.035	0.016	-.037	0.006	-.072	0.019
-26	0.000	0.000	-.010	0.020	-.032	0.006	-.042	0.024
-30	-.009	0.005	-.011	0.018	-.020	0.008	-.040	0.021
-34	0.008	0.023	-.017	0.010	-.007	0.004	-.016	0.025
-38	0.000	0.000	-.011	0.009	0.005	0.004	-.006	0.011
-40 to 0	-.029	0.024	-.185	0.028	-.417	0.113	-.630	0.126
-40 to 90	0.242	0.048	-.096	0.046	-.532	0.109	-.386	0.099

Appendix D: Hydrological Datasets

Baumgartner and Reichel

Baumgartner and Reichel (1975) compiled their atlas of runoff and P-E statistics using regional maps from local hydrological or meteorological agencies. Using the hydrological balance equation for long-term means, P-E = runoff, they manually and iteratively balanced the maps. The duration and years covered by the local maps certainly vary, and as this publication appeared about midway through the period covered by the GFDL dataset, there is at most 10 years of overlap between the datasets. Given any decadal variability in river flows, the results of Baumgartner and Reichel may at best be considered an indication of the sign and order of magnitude of discharges. Nonetheless, the dataset is valuable because it represents a measure of hydrological quantities independent of atmospheric observations.

Global Runoff Data Centre (GRDC)

The GRDC, part of the World Meteorological Organization (WMO), maintains a dataset of discharges for the major rivers of the world, based on observations at hydrological stations. A recent GRDC report (1994) presents time series of runoff for the 20 largest rivers; data is available digitally for a number of others. Data from one or more observing stations is catalogued for each river. In preparing time series for comparison with model results for this thesis, care was taken to choose data from the observing station closest to the river mouth. In most cases, the time series from the closest station was as long or longer than series from further stations. Also, stations tended to be several hundred kilometers apart. Since there would have been little benefit from mixing station data to create more complete time series, the GRDC data presented in Figs 22a-22i represent runoff measured at only one station per river.

The annual means derived from GRDC data in Table 4-1 are calculated from time series that vary widely in terms of number of years and the specific years covered. The reader interested in comparing GISS model results with GRDC time series is advised to examine Figs. 22a-22i for the relevant river, to see the period spanned by GRDC observations.

Appendix E: Catalogue of Statistics

Global moisture flux transports and divergence, mass flux divergence, and precipitable water statistics based on the GFDL dataset over the time period 1963-1973 are presented and discussed in the Peixoto and Oort text (1992). The statistics included here, though they represent the longer and slightly shifted time period 1965-1989, do not differ significantly from Peixoto and Oort's results but are included for the sake of completeness.

As an example of the differences that may be expected due to increases in dataset duration, Figures E-1 and E-2 show the standard deviation of the zonally averaged moisture flux transports plotted as a function of the number of years included in the calculation, starting with 1965 and adding consecutive years in turn. The plots indicate that the standard deviation after 10 years is a good approximation to that at 25 years at most latitudes.

In the following calculations, the December/January/February mean was computed using consecutive months. Since January 1964 is the earliest month in the GFDL dataset with global data, December 1964/January-February 1965 is the earliest winter season included (December 1989 is unused). Annual and June/July/August statistics only include months from January 1965 through December 1989. Therefore, DJF, JJA and annual statistics are all based on 25-year time series.

The included figures are:

Zonal water vapor transport, 25-year mean

Fig. E-3 Annual

Fig. E-4 DJF

Fig. E-5 JJA

Zonal water vapor transport, 25-year mean, annual or seasonal zonal mean subtracted from each year (Annual/DJF/JJA)

Fig. E-6 Annual

Fig. E-7 DJF

Fig. E-8 JJA

Zonal water vapor transport, interannual standard deviation

Fig. E-9 Annual

Fig. E-10 DJF

Fig. E-36 Second

Fig. E-37 Third

Meridional moisture flux EOFs and time series

Fig. E-38 First

Fig. E-39 Second

Fig. E-40 Third

Figure E-1.

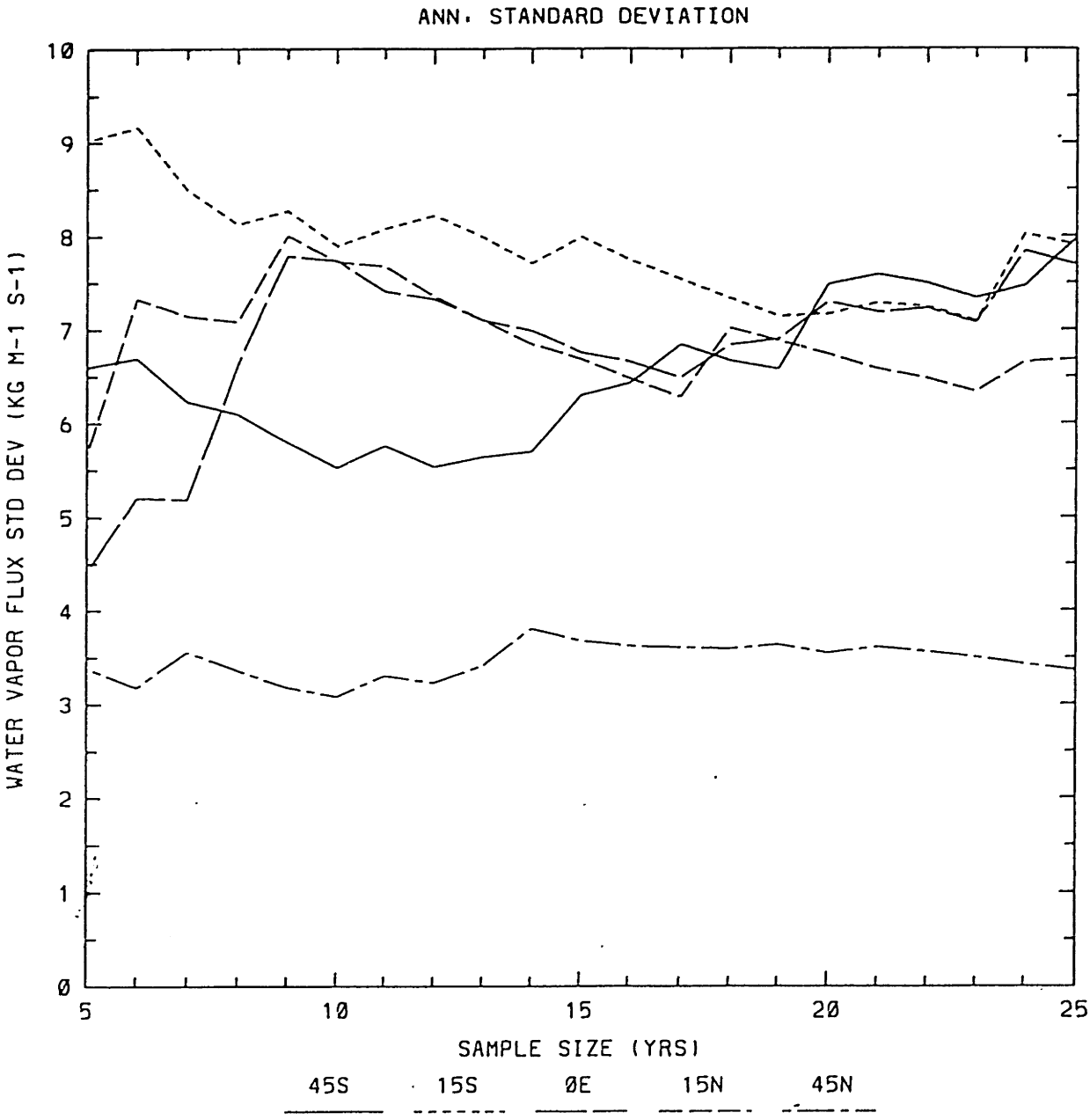
ZONAL WATER VAPOR TRANSPORT
ANN. STANDARD DEVIATION
WATER VAPOR FLUX STD DEV (KG M-1 S-1)
10
9
8
7
6
5
4
3
2
1
0
5
10
15
20
25
SAMPLE SIZE (YRS)
45S
15S
0E
15N
45N

Figure E-2.

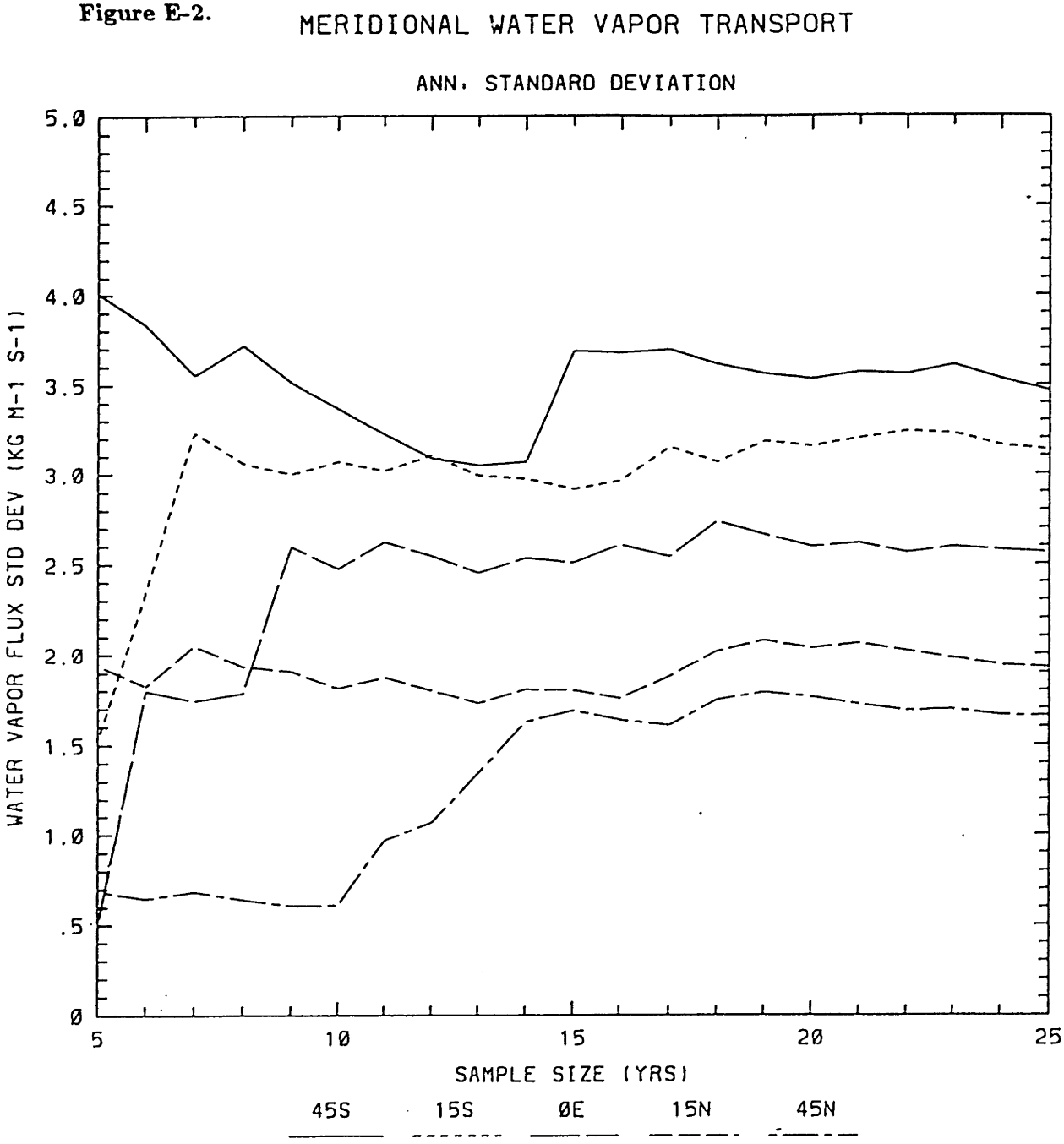
MERIDIONAL WATER VAPOR TRANSPORT
ANN. STANDARD DEVIATION
WATER VAPOR FLUX STD DEV (KG M-1 S-1)
5.0
4.5
4.0
3.5
3.0
2.5
2.0
1.5
1.0
.5
0
5
10
15
20
25
SAMPLE SIZE (YRS)
45S
15S
0E
15N
45N

Figure E-3.

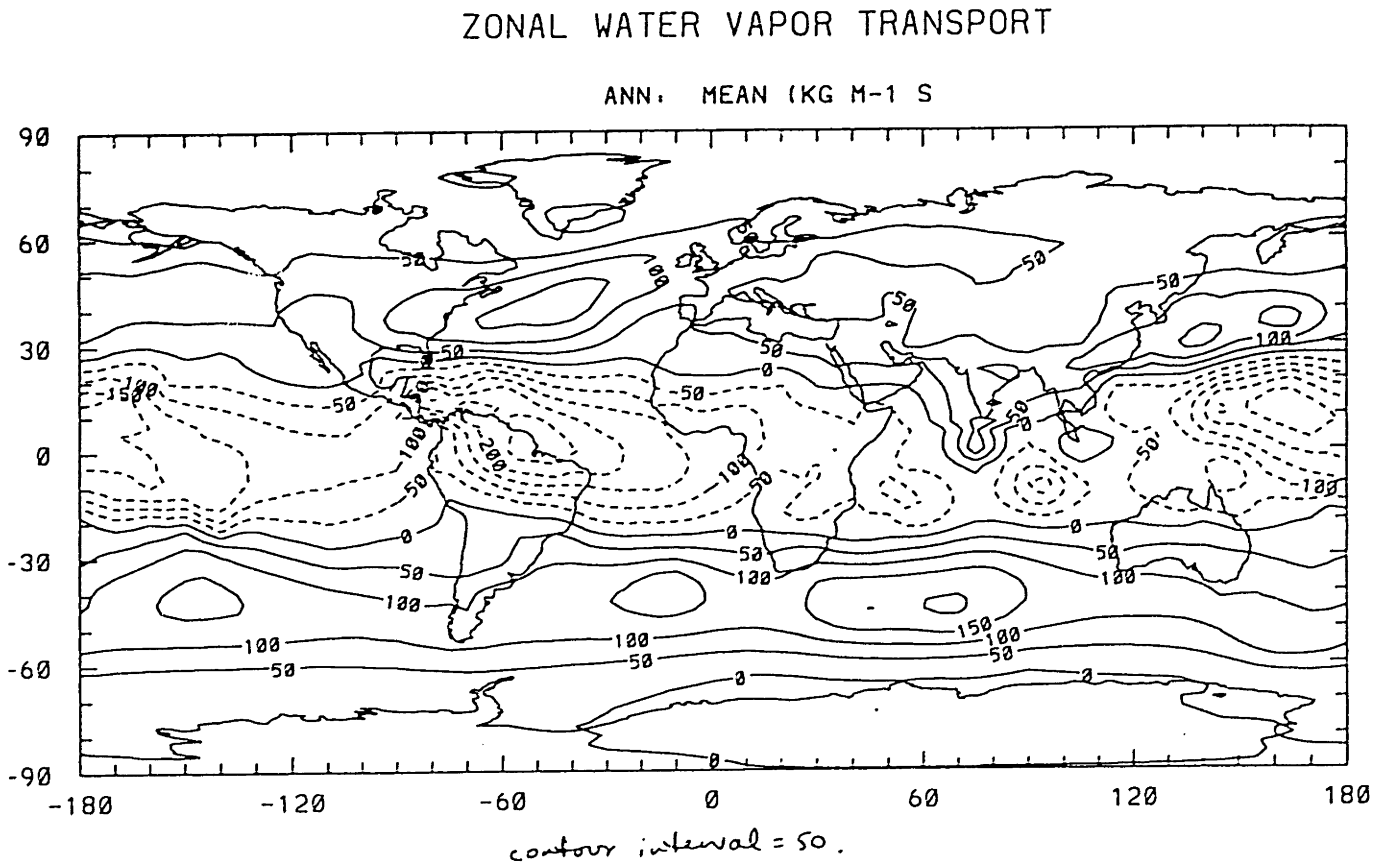
ZONAL WATER VAPOR TRANSPORT
ANN: MEAN (KG M-1 S
90
60
30
0
-30
-60
-90
-180
-120
-60
0
60
120
180
contour interval = 50.

Figure E-4.

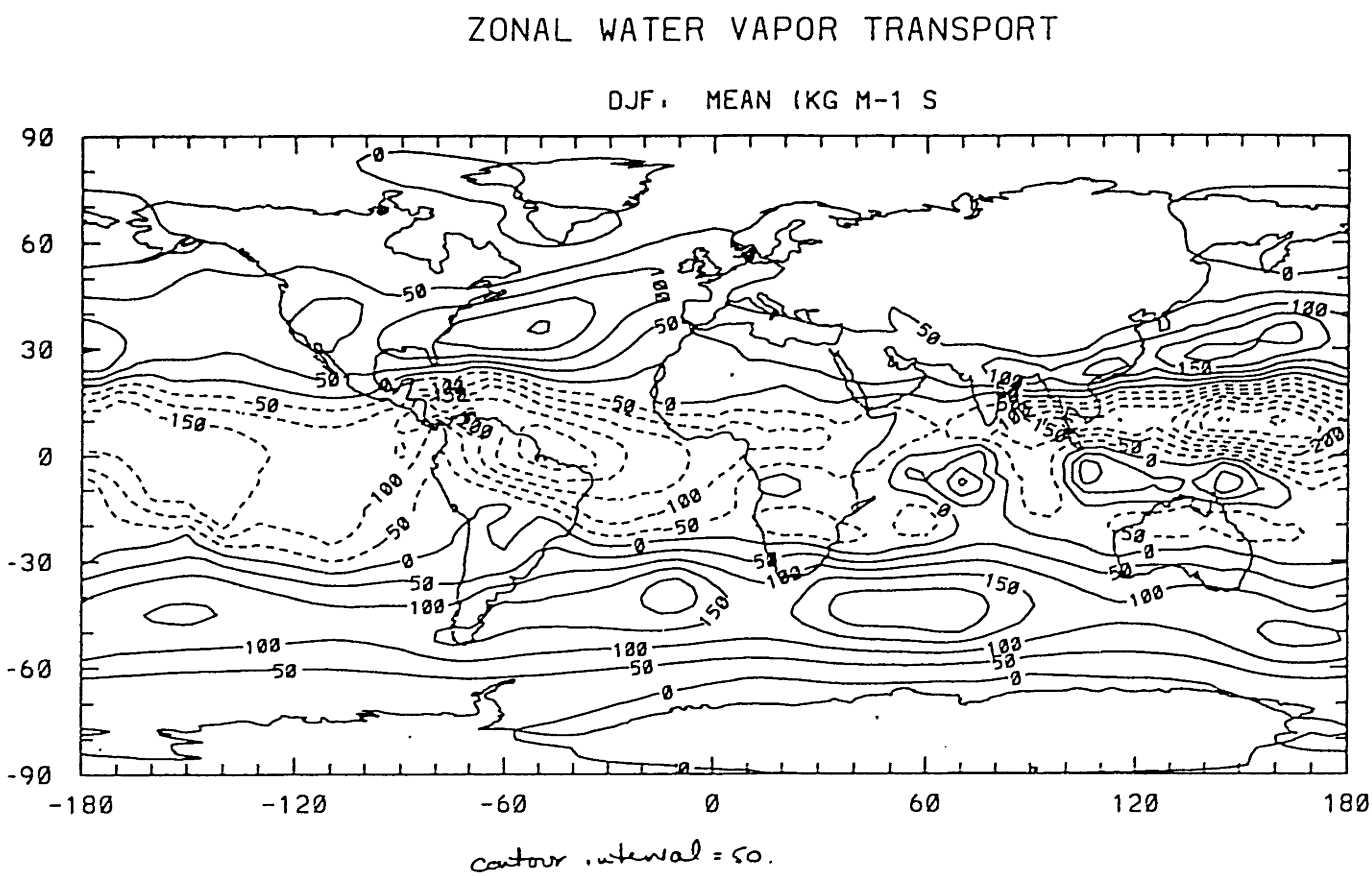
ZONAL WATER VAPOR TRANSPORT
DJF: MEAN (KG M-1 S
90
60
30
0
-30
-60
-90
-180
-120
-60
0
60
120
180
contour interval = 50.

Figure E-5.

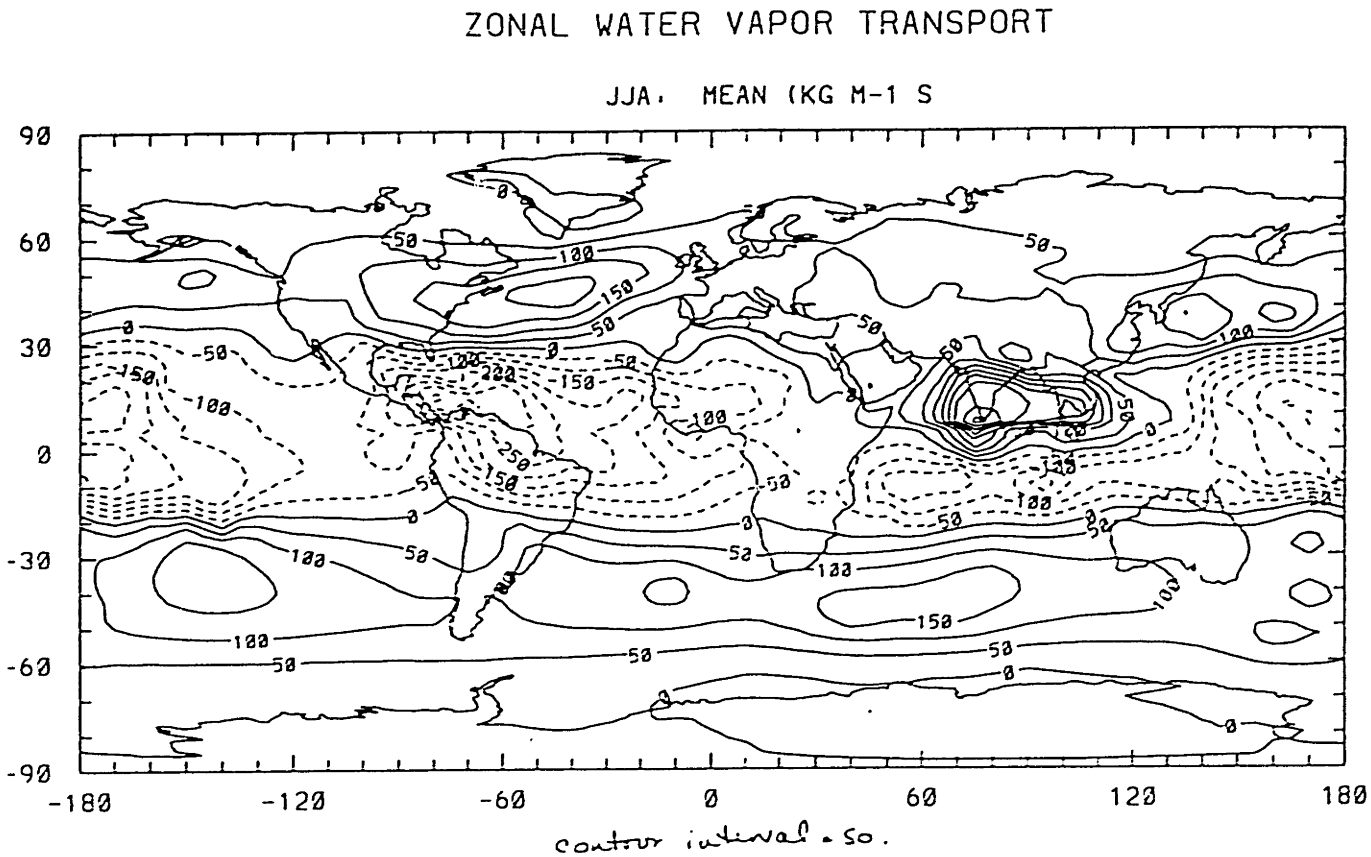
ZONAL WATER VAPOR TRANSPORT
JJA. MEAN (KG M-1 S
90
60
30
0
-30
-60
-90
-180
-120
-60
0
60
120
180
contour interval = 50.

Figure E-6.

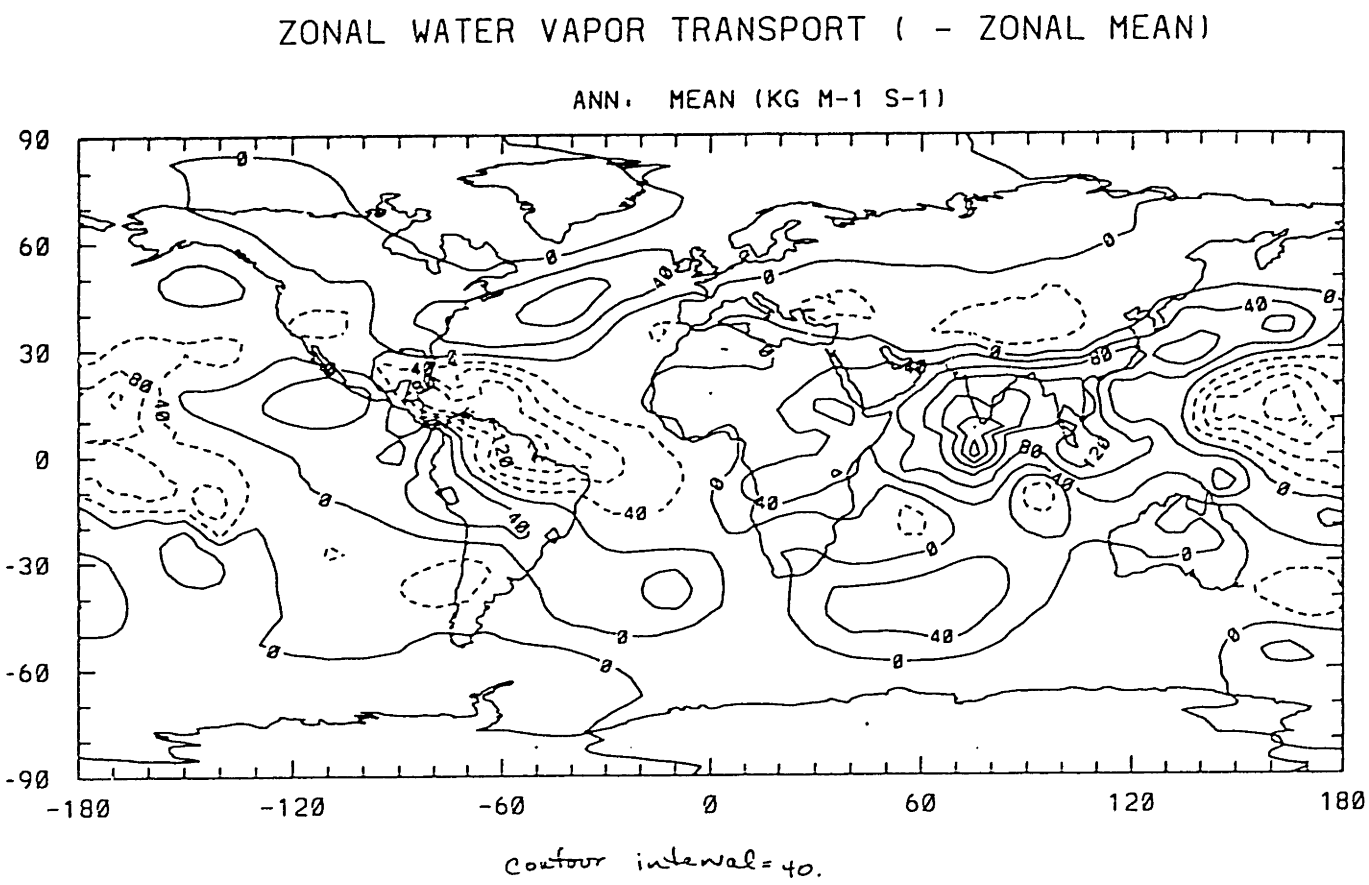
ZONAL WATER VAPOR TRANSPORT (- ZONAL MEAN)
ANN. MEAN (KG M-1 S-1)
90
60
30
0
-30
-60
-90
-180
-120
-60
0
60
120
180
Contour interval = 40.

Figure E-7.

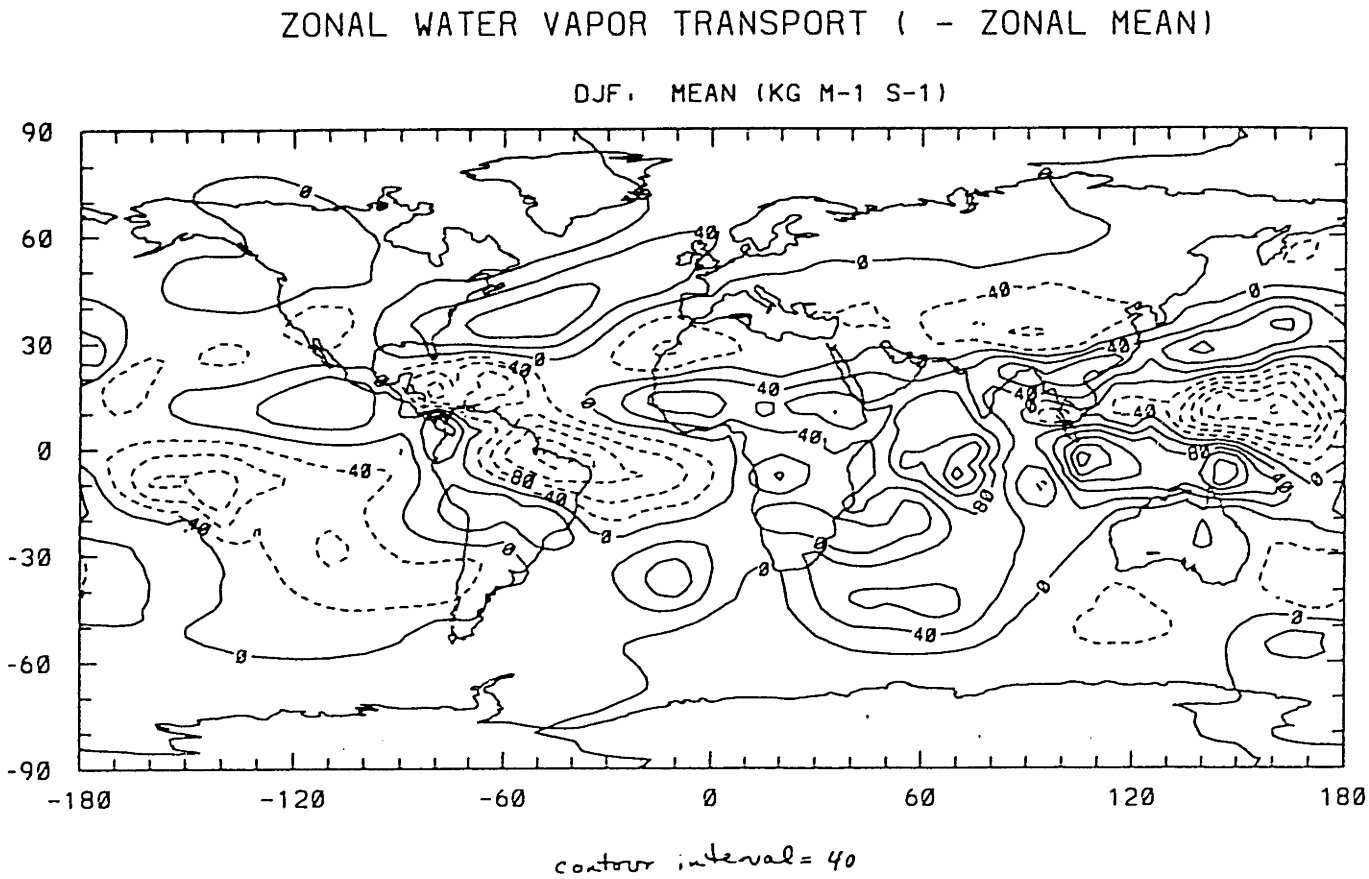
ZONAL WATER VAPOR TRANSPORT (- ZONAL MEAN)
DJF, MEAN (KG M-1 S-1)
90
60
30
0
-30
-60
-90
-180
-120
-60
0
60
120
180
contour interval = 40

Figure E-8.

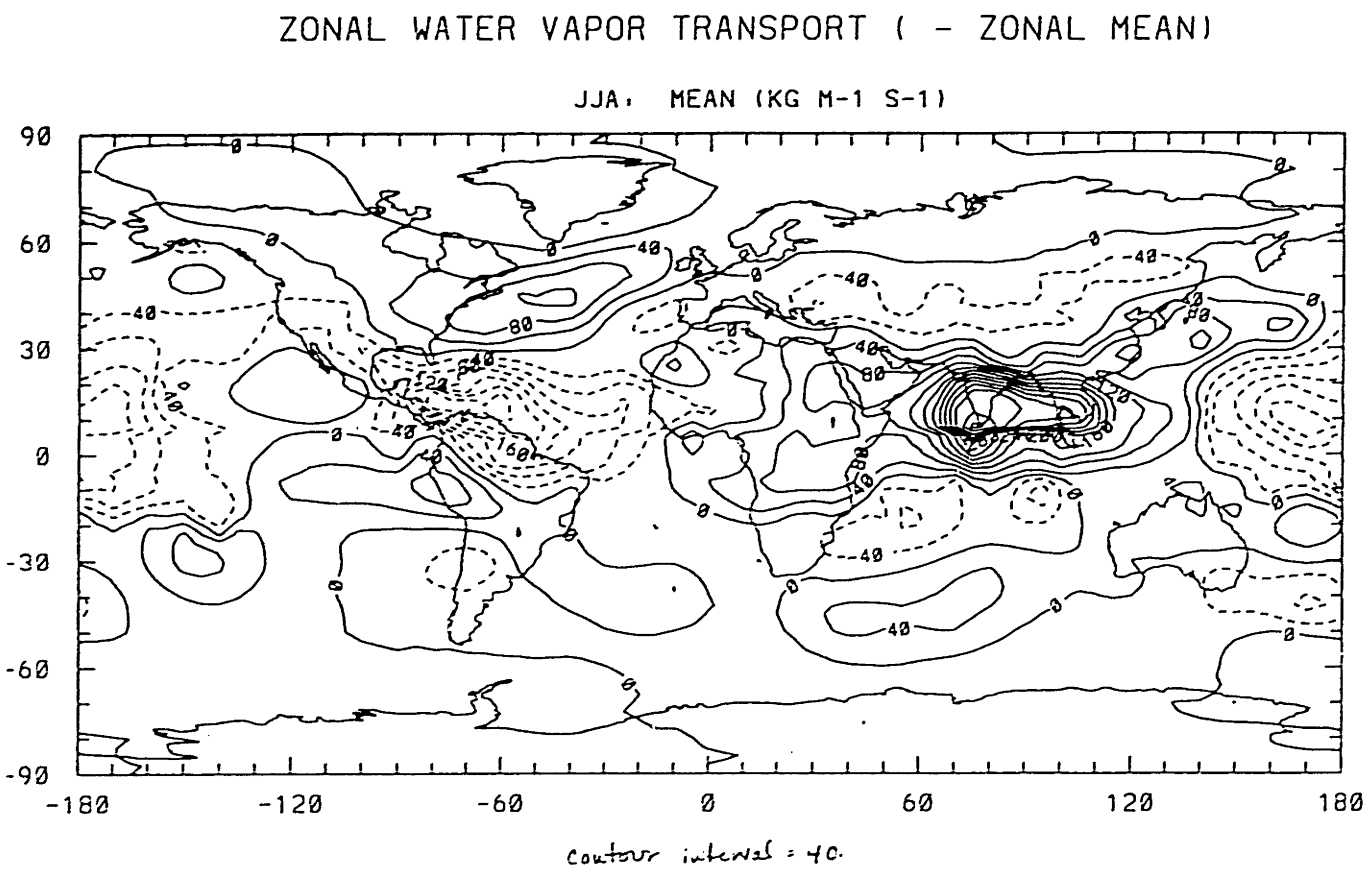
ZONAL WATER VAPOR TRANSPORT (- ZONAL MEAN)
JJA, MEAN (KG M-1 S-1)
90
60
30
0
-30
-60
-90
-180
-120
-60
0
60
120
180
Contour interval = 40.

Figure E-9.

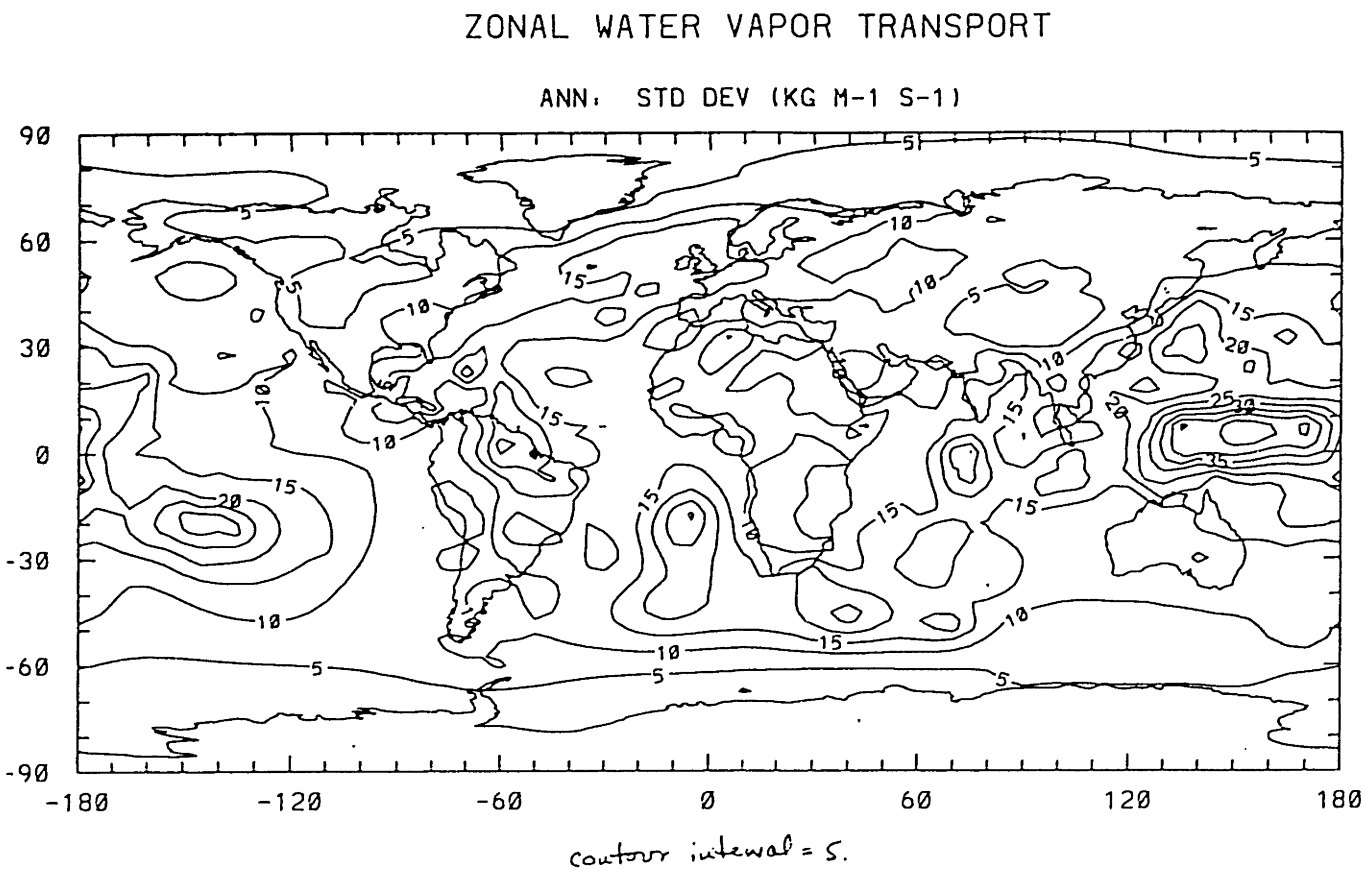
ZONAL WATER VAPOR TRANSPORT
ANN: STD DEV (KG M-1 S-1)
90
60
30
0
-30
-60
-90
-180
-120
-60
0
60
120
180
contour interval = 5.

Figure E-10.

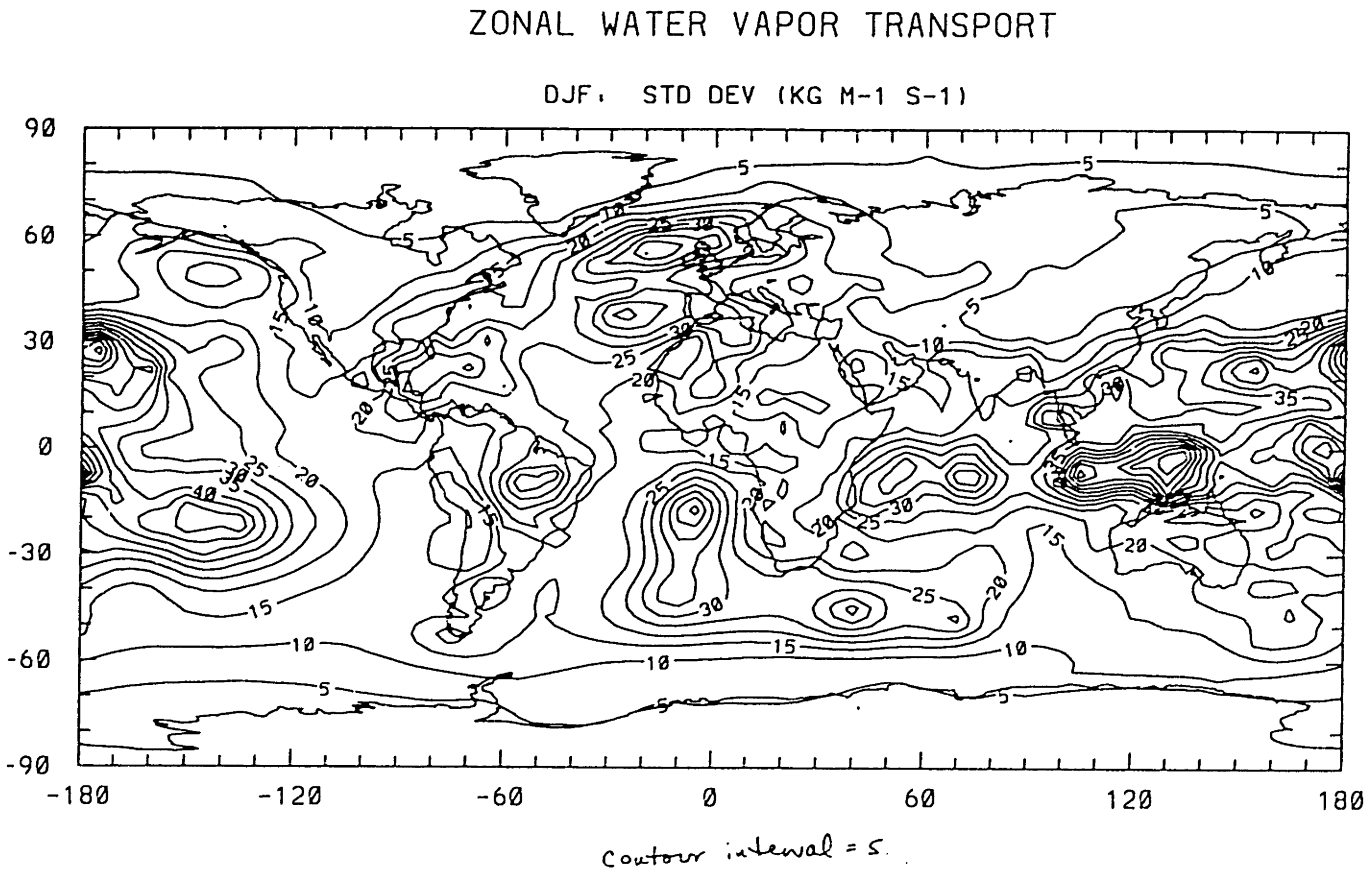
ZONAL WATER VAPOR TRANSPORT
DJF, STD DEV (KG M-1 S-1)
90
60
30
0
-30
-60
-90
-180
-120
-60
0
60
120
180
Contour interval = 5

Figure E-11.

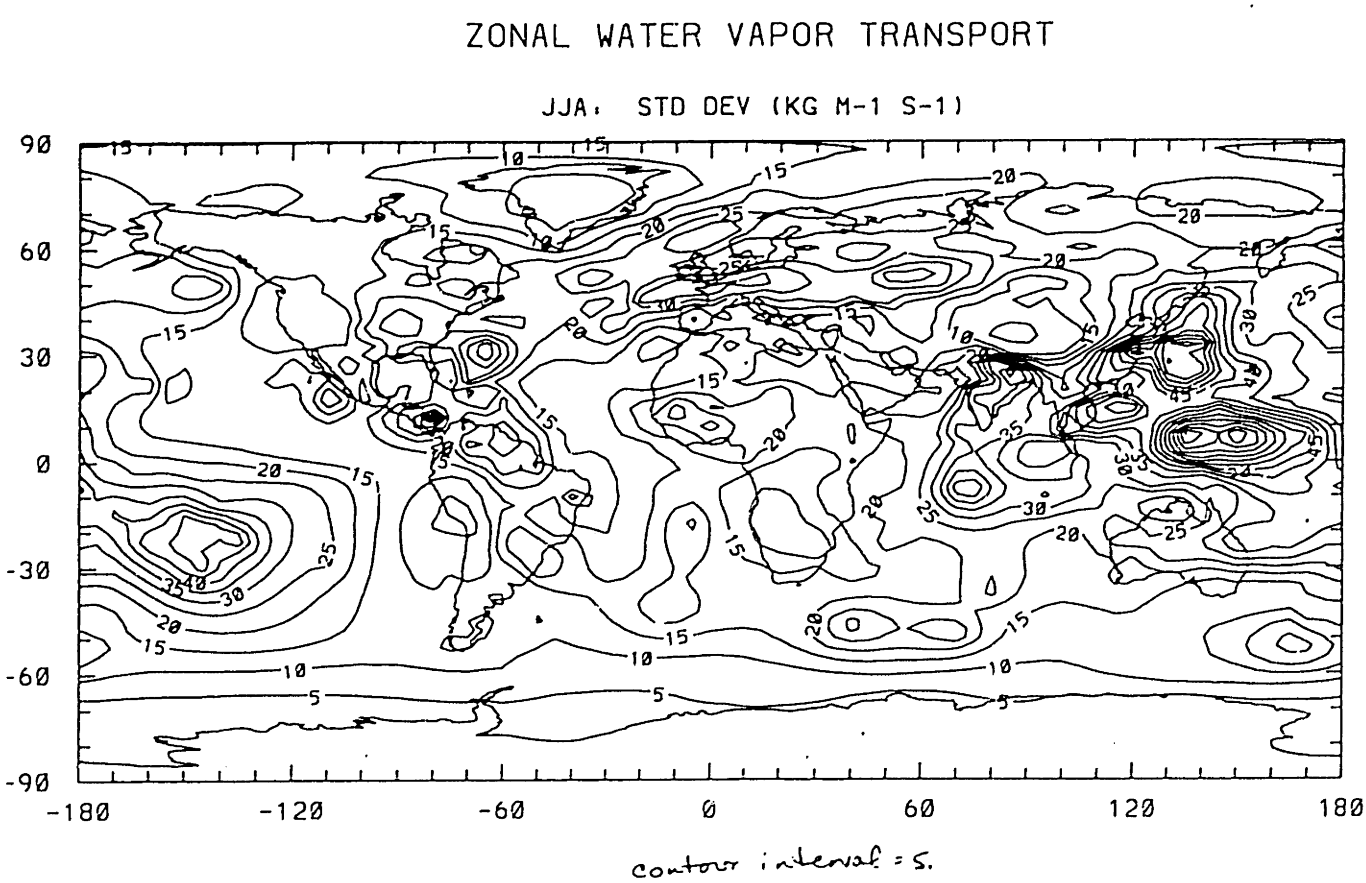
ZONAL WATER VAPOR TRANSPORT
JJA: STD DEV (KG M-1 S-1)
90
60
30
0
-30
-60
-90
-180
-120
-60
0
60
120
180
contour interval = 5.

Figure E-12.

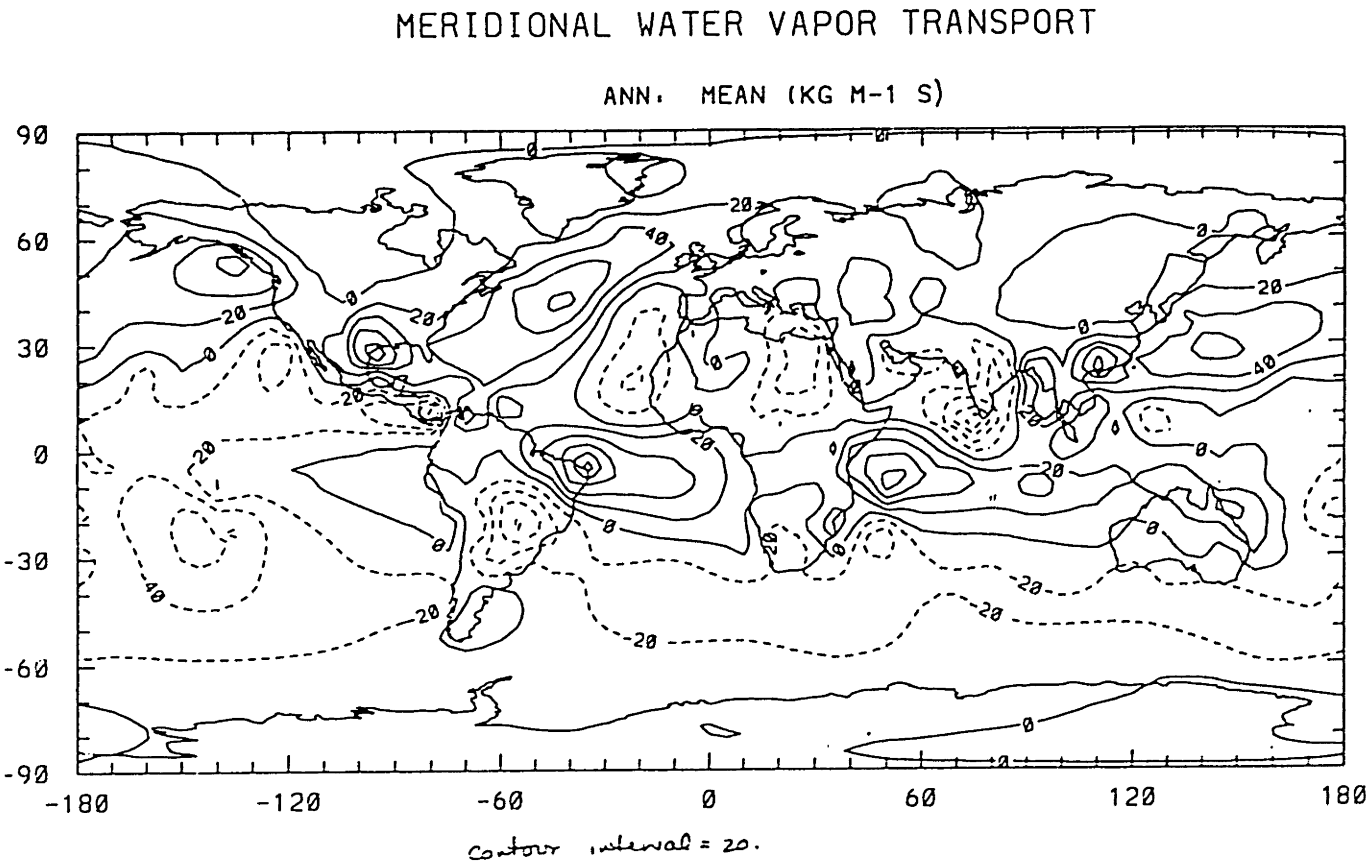
MERIDIONAL WATER VAPOR TRANSPORT
ANN. MEAN (KG M-1 S)
90
60
30
0
-30
-60
-90
-180
-120
-60
0
60
120
180
Contour interval = 20.

Figure E-13.

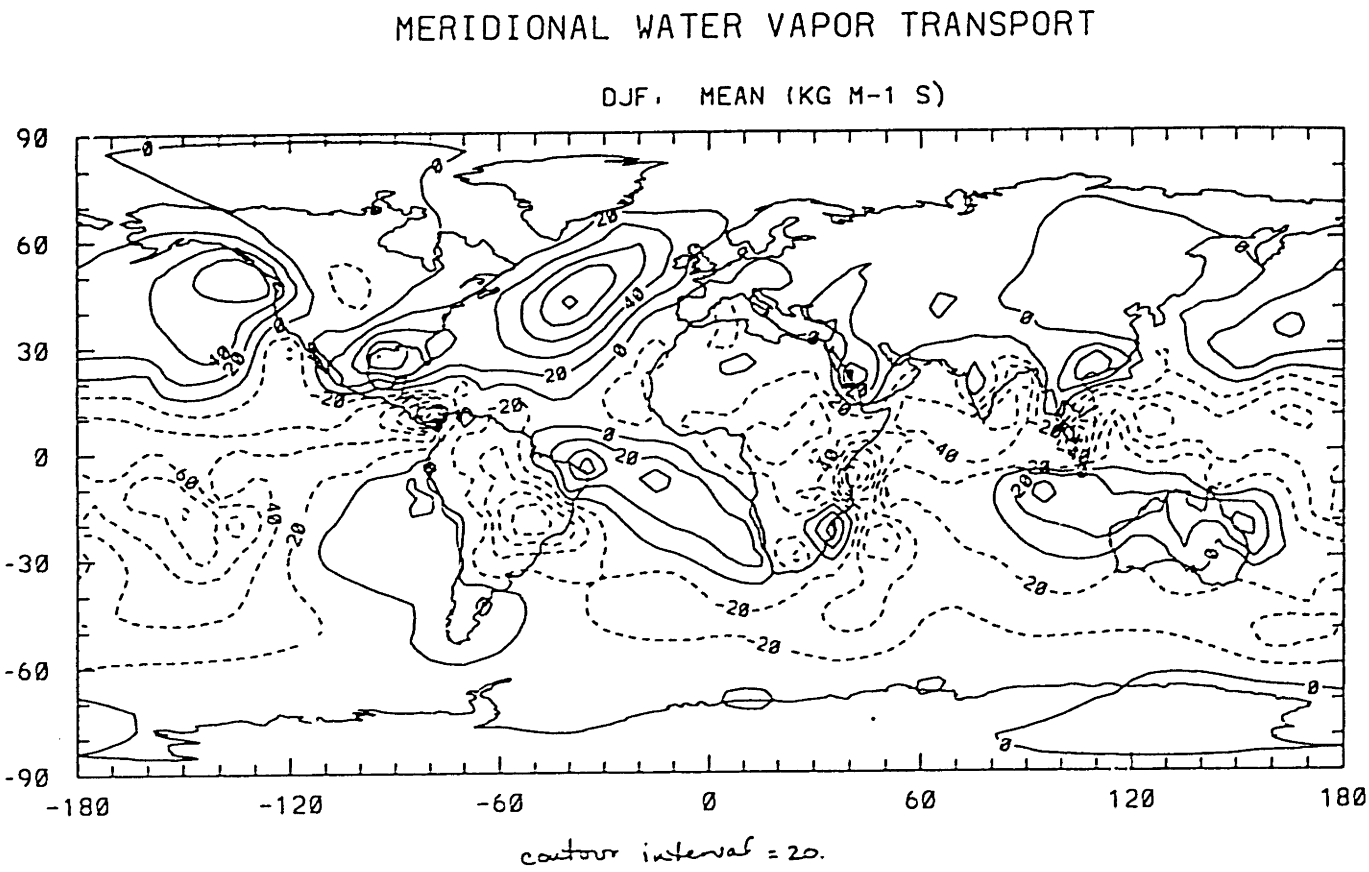
MERIDIONAL WATER VAPOR TRANSPORT
DJF, MEAN (KG M-1 S)
90
60
30
0
-30
-60
-90
-180
-120
-60
0
60
120
180
contour interval = 20.

Figure E-14.

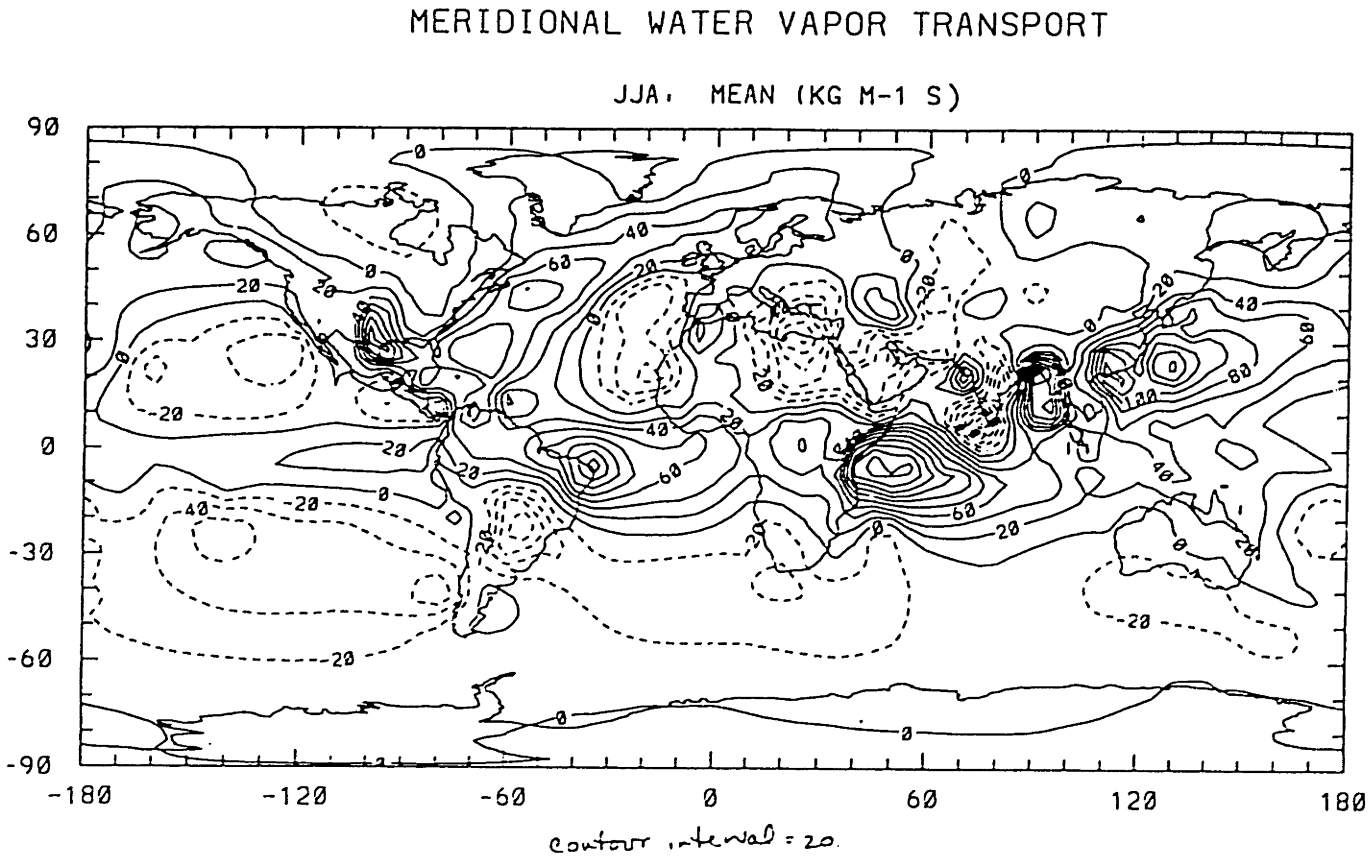
MERIDIONAL WATER VAPOR TRANSPORT
JJA. MEAN (KG M-1 S)
90
60
30
0
-30
-60
-90
-180
-120
-60
0
60
120
180
Contour interval = 20.

Figure E-15.

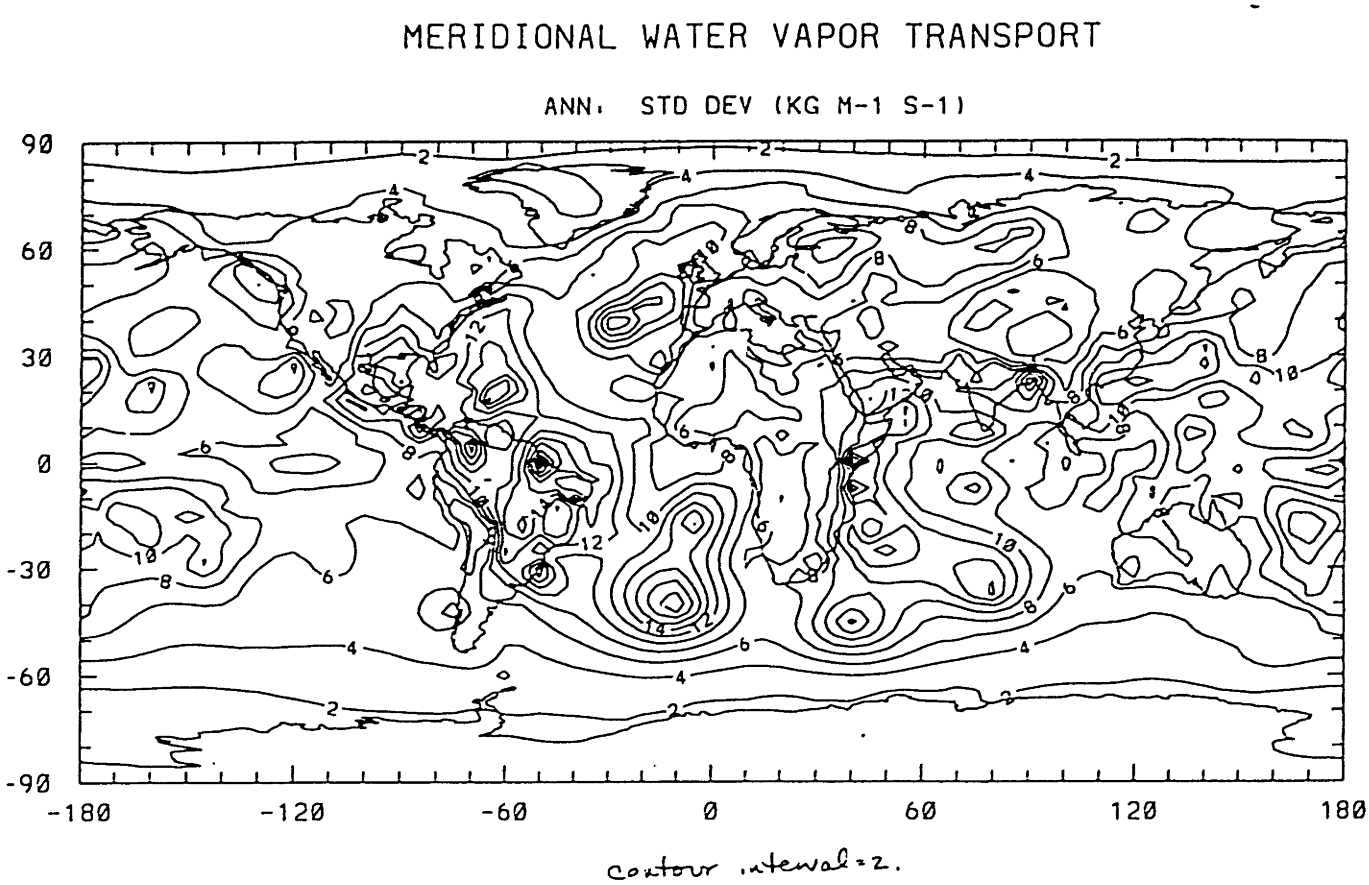
MERIDIONAL WATER VAPOR TRANSPORT
ANN. STD DEV (KG M-1 S-1)
90
60
30
0
-30
-60
-90
-180
-120
-60
0
60
120
180
contour interval=2.

Figure E-16.

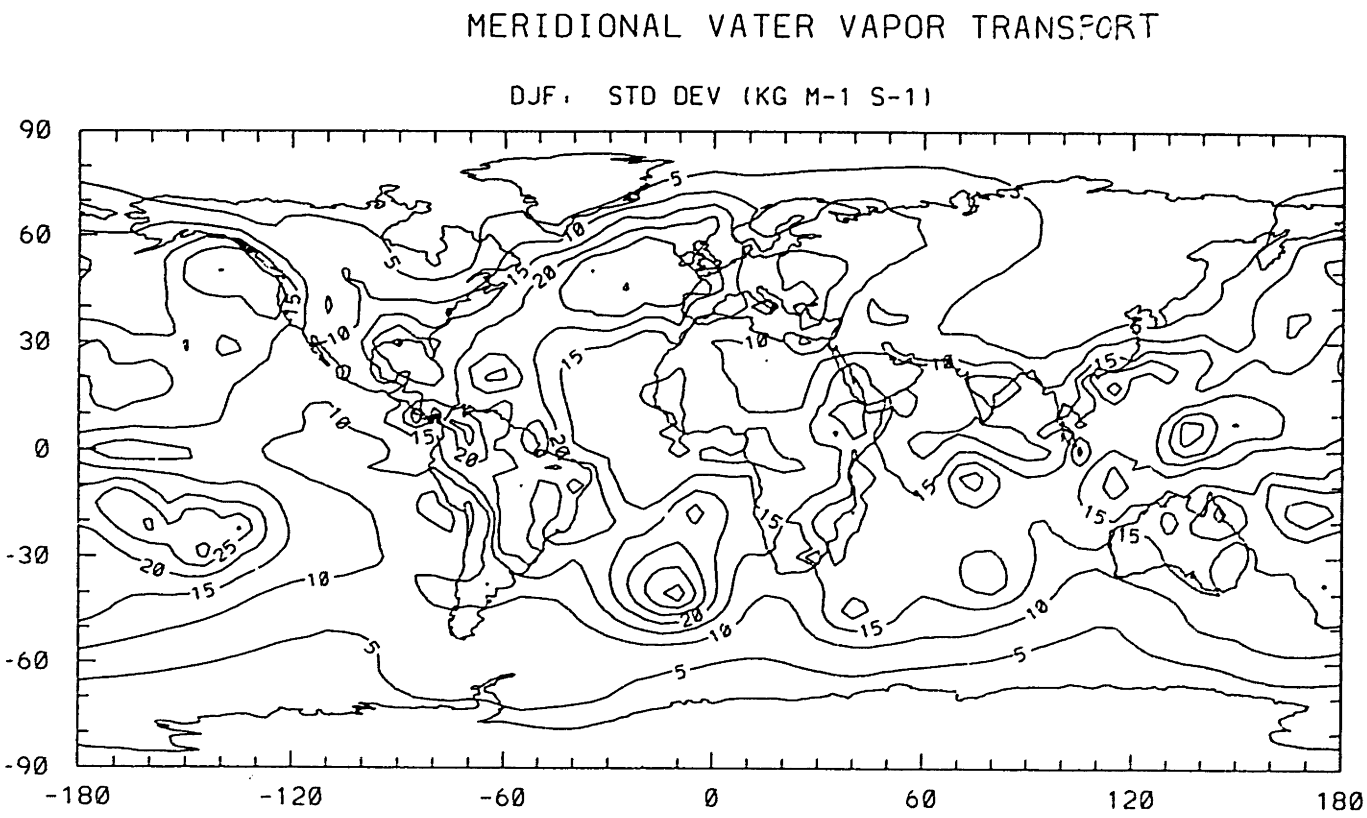
MERIDIONAL VATER VAPOR TRANSPORT
DJF: STD DEV (KG M-1 S-1)
90
60
30
0
-30
-60
-90
-180
-120
-60
0
60
120
180

Figure E-17.

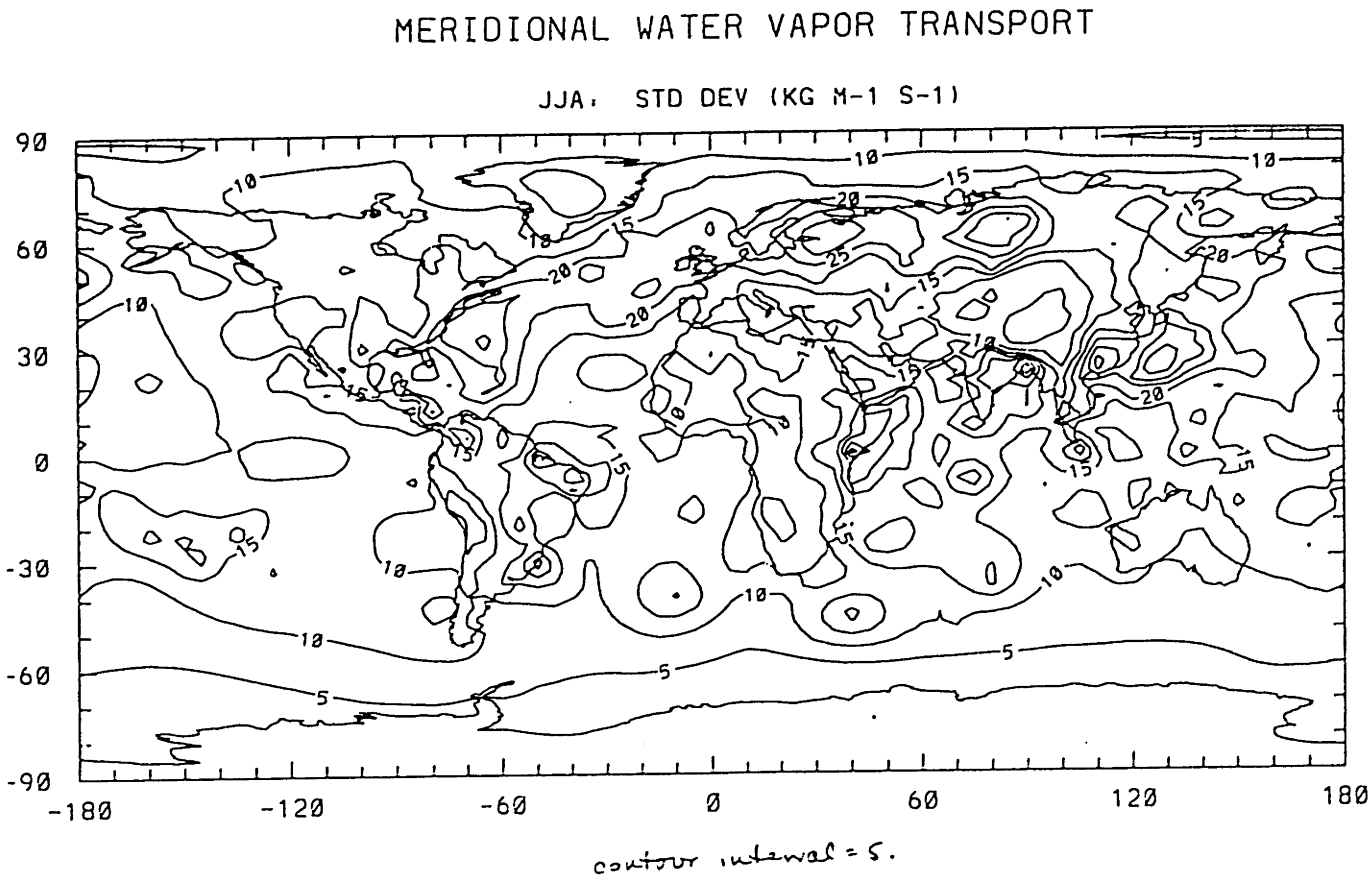
MERIDIONAL WATER VAPOR TRANSPORT
JJA: STD DEV (KG M-1 S-1)
90
60
30
0
-30
-60
-90
-180
-120
-60
0
60
120
180
contour interval = 5.

Figure E-18.

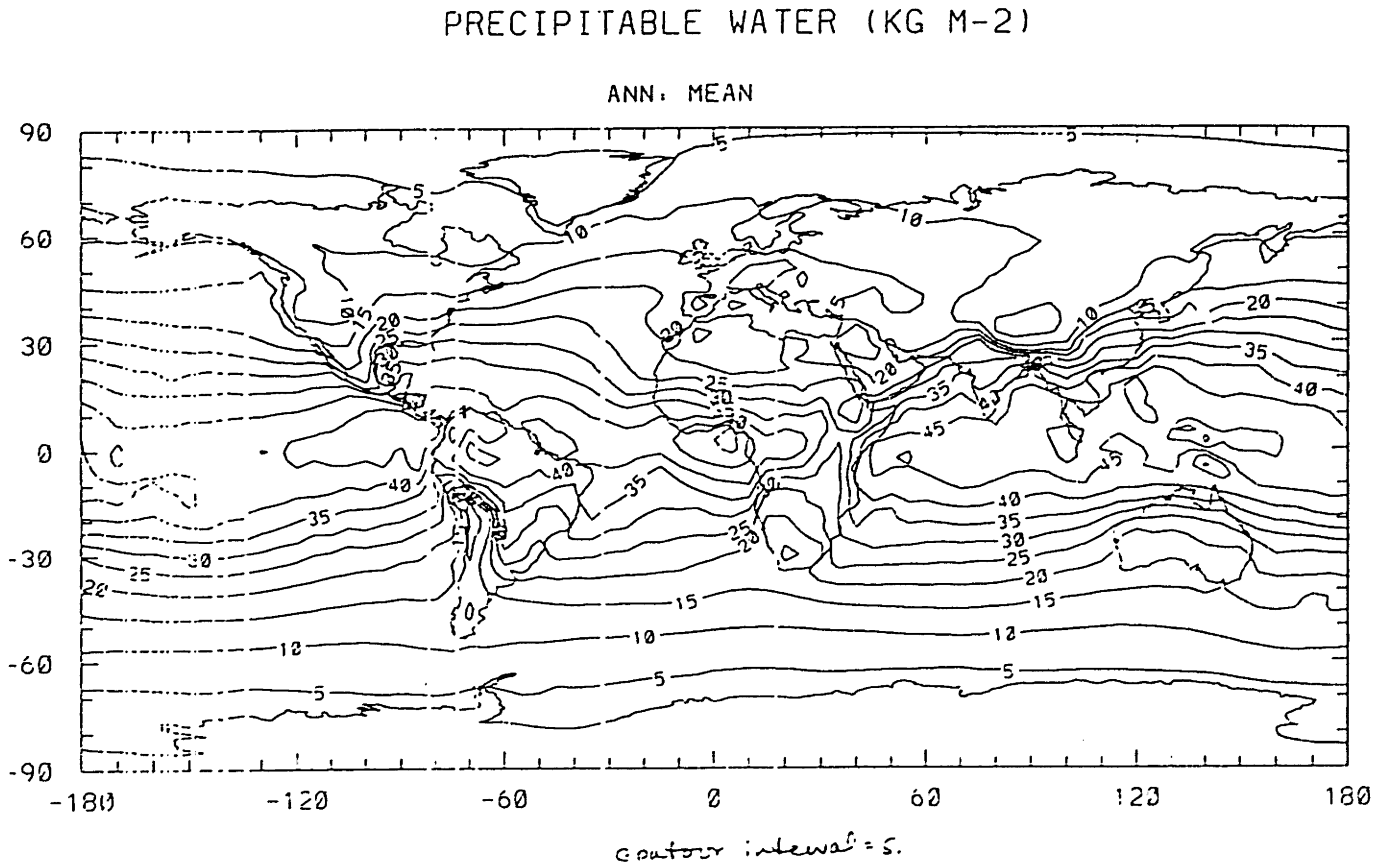
PRECIPITABLE WATER (KG M-2)
ANN: MEAN
90
60
30
0
-30
-60
-90
-180
-120
-60
0
60
120
180
Contour interval = 5.

Figure E-19.

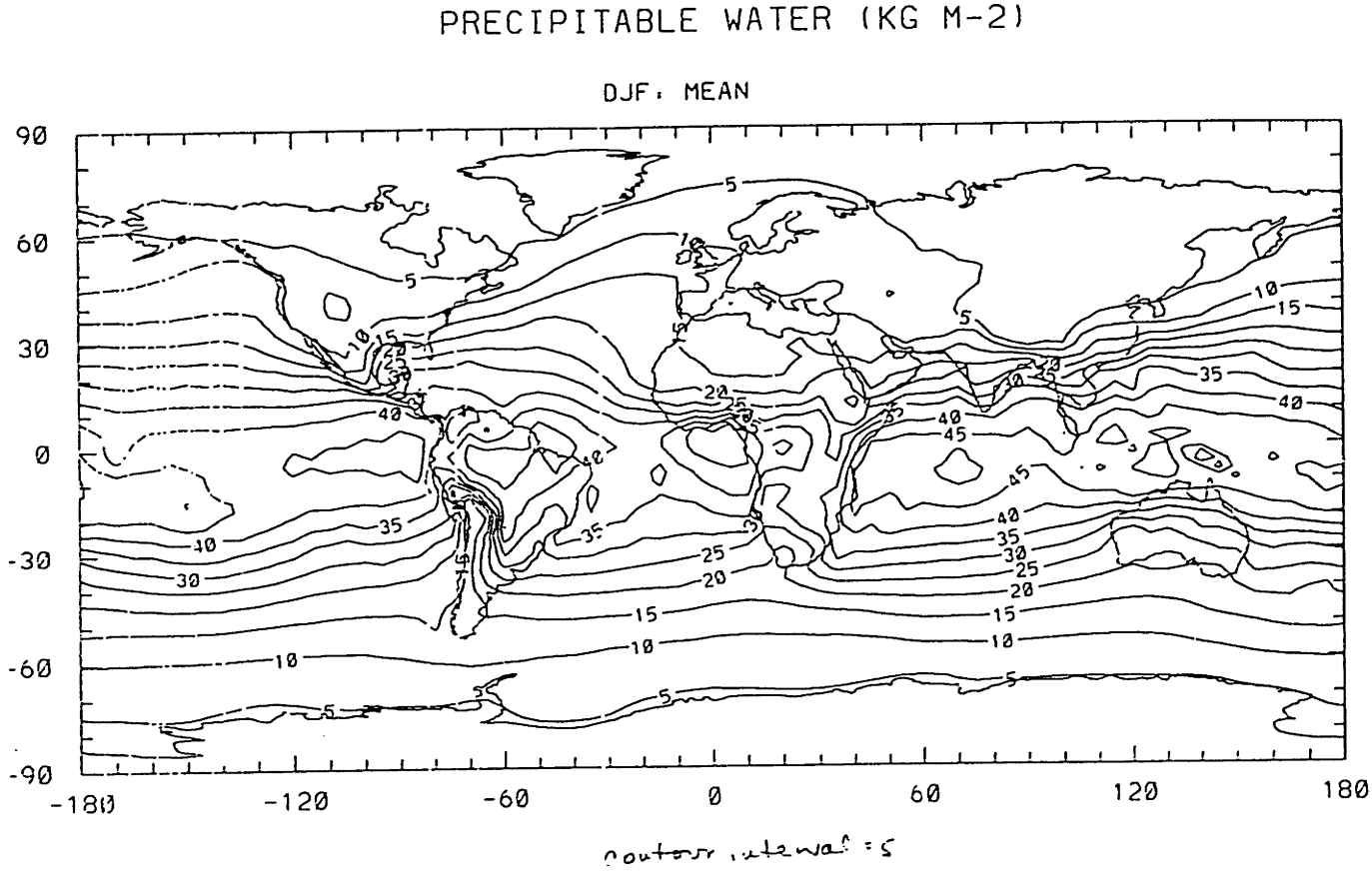
PRECIPITABLE WATER (KG M-2)
DJF: MEAN
90
60
30
0
-30
-60
-90
-180
-120
-60
0
60
120
180
contour interval = 5

Figure E-20.

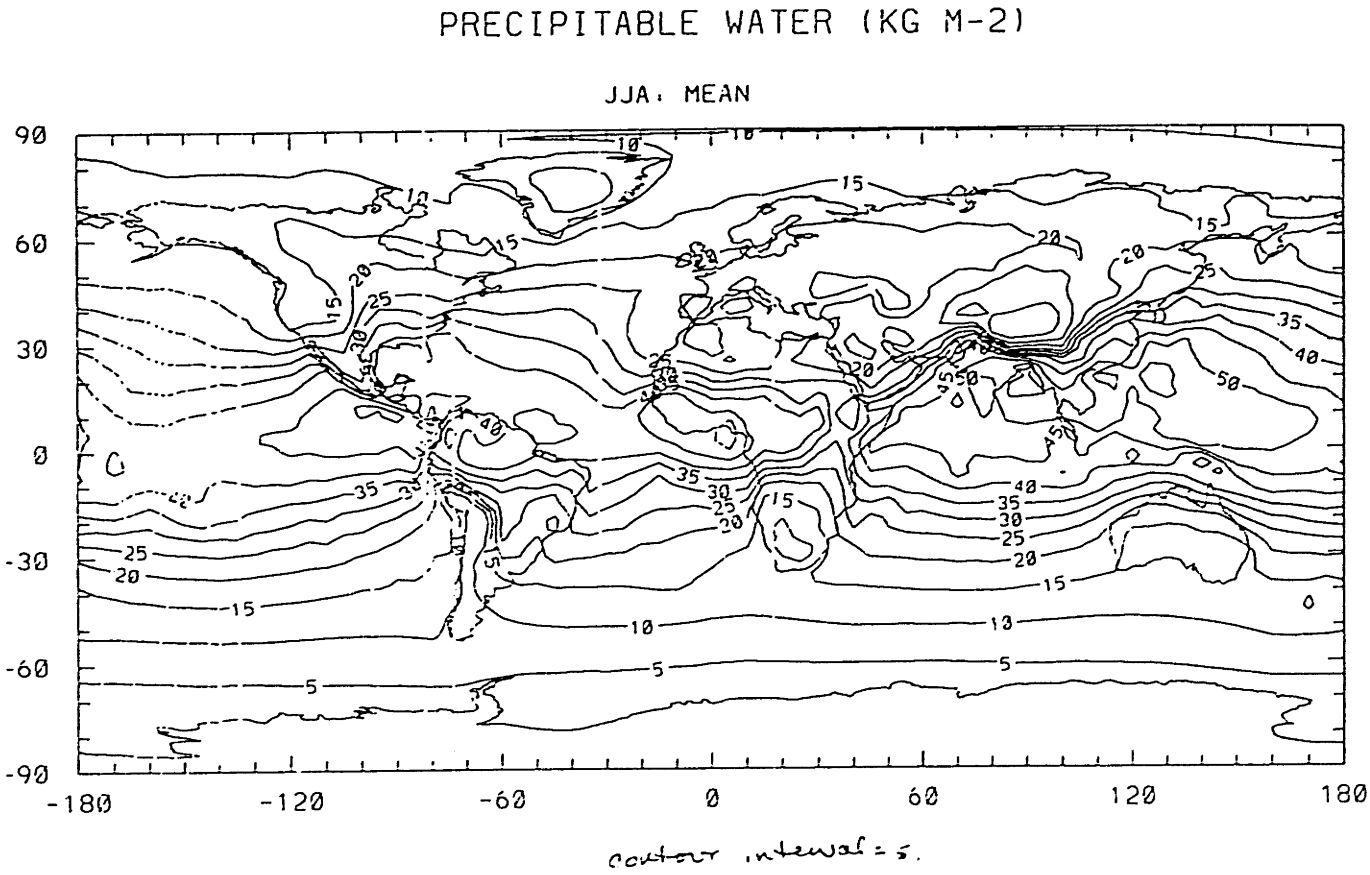
PRECIPITABLE WATER (KG M-2)
JJA: MEAN
90
60
30
0
-30
-60
-90
-180
-120
-60
0
60
120
180
contour interval = 5.

Figure E-21.

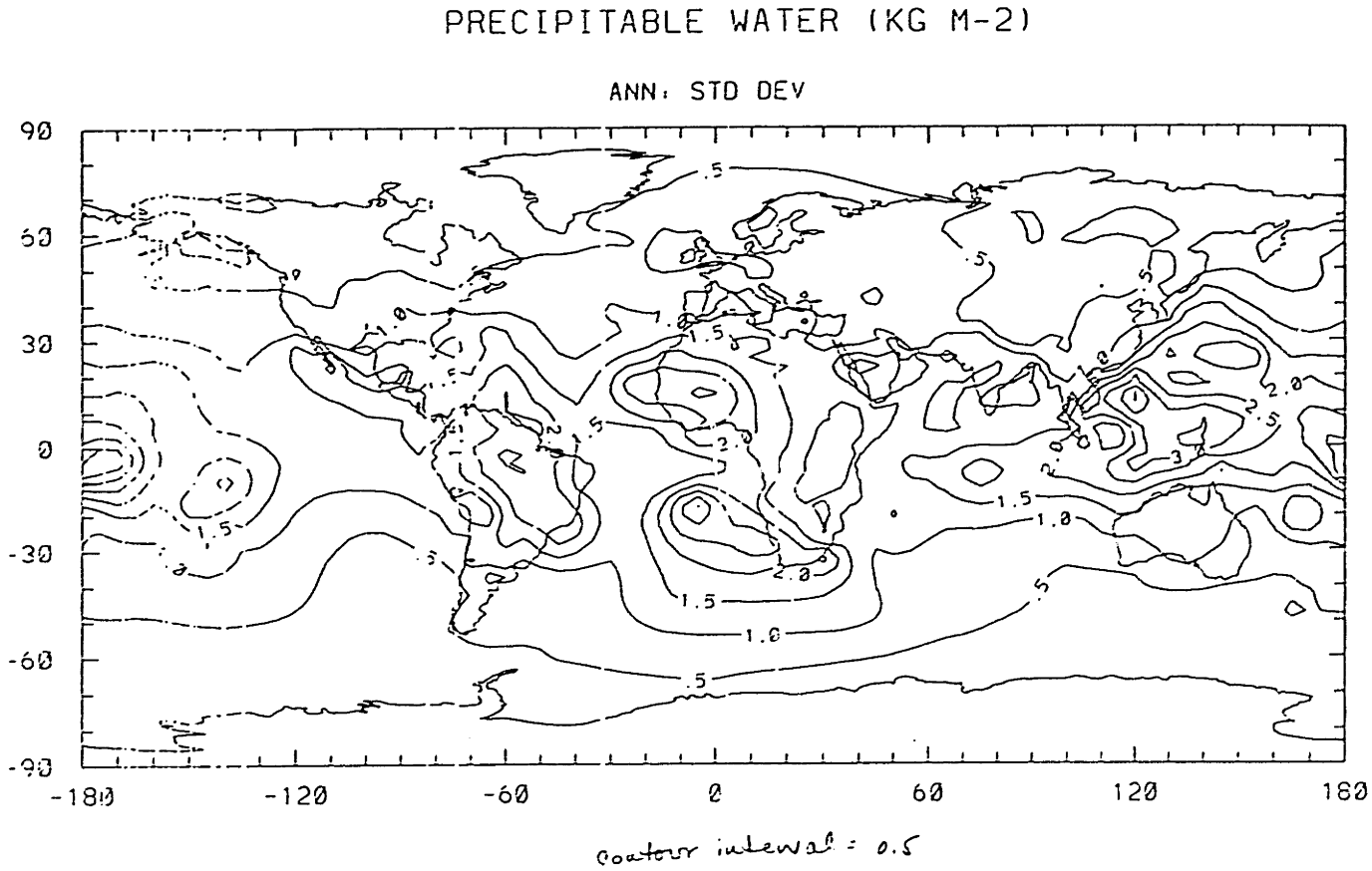
PRECIPITABLE WATER (KG M-2)
ANN: STD DEV
90
60
30
0
-30
-60
-90
-180
-120
-60
0
60
120
180
Contour interval = 0.5

Figure E-22.

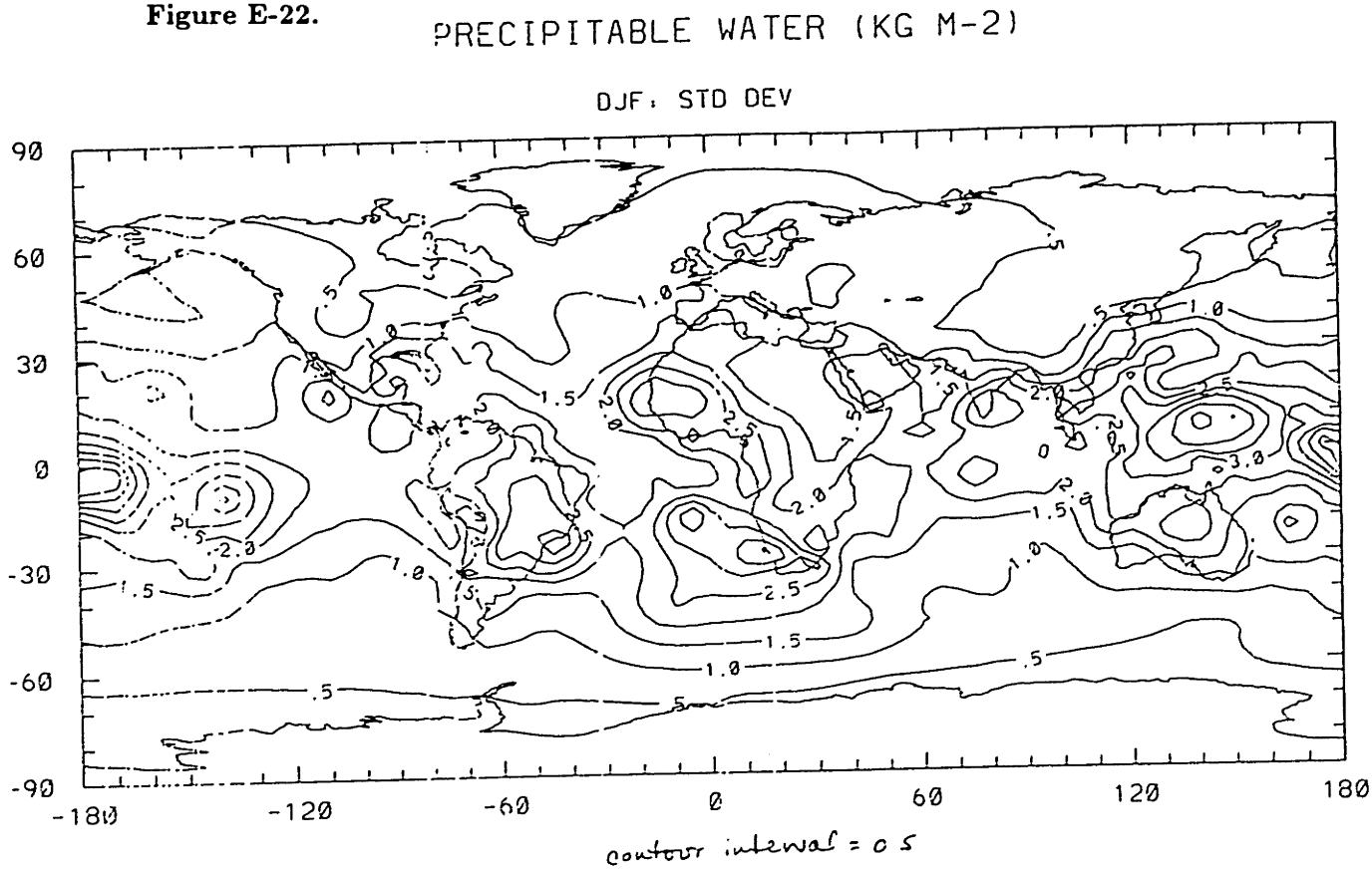
PRECIPITABLE WATER (KG M-2)
DJF: STD DEV
90
60
30
0
-30
-60
-90
-180
-120
-60
0
60
120
180
contour interval = 0.5

Figure E-23.

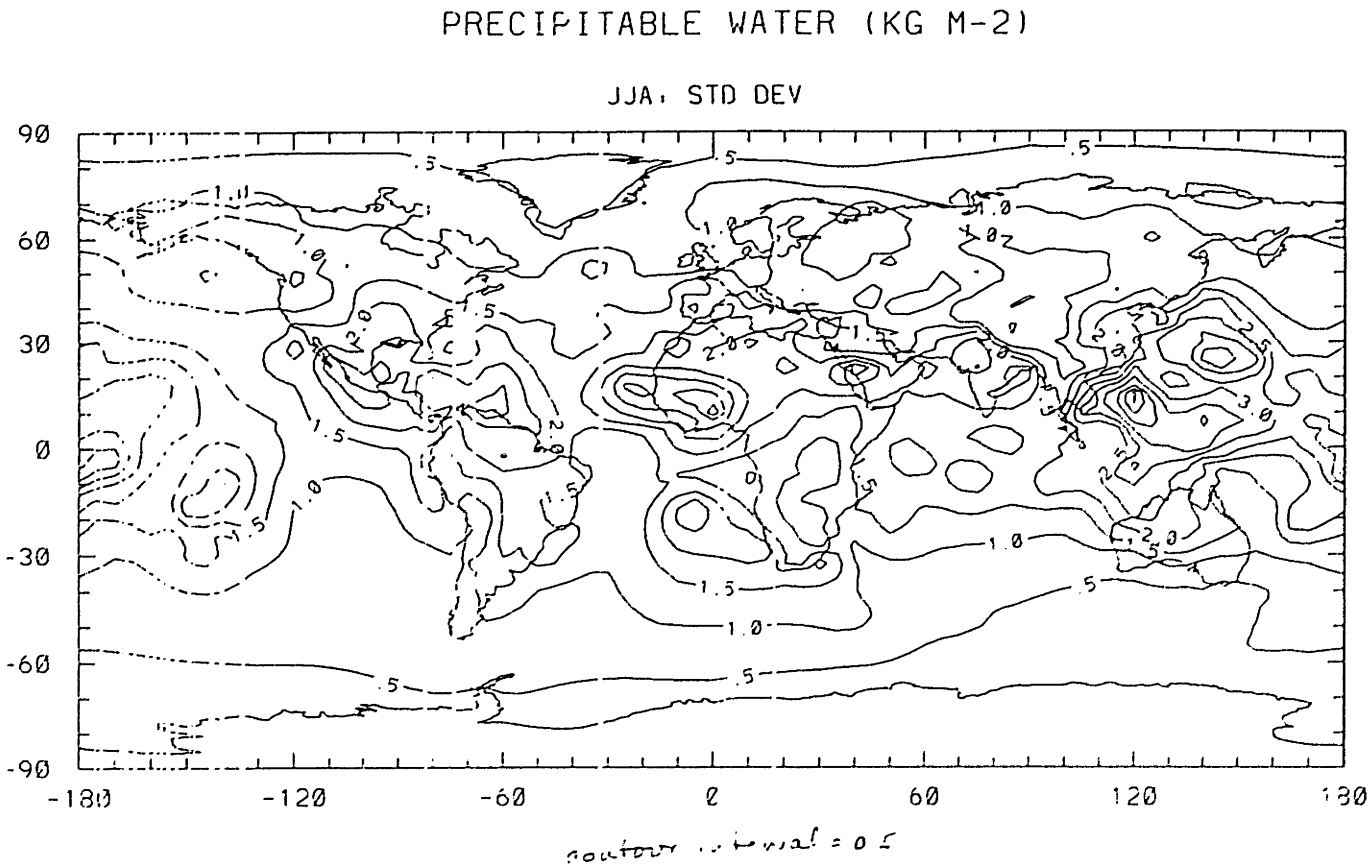
PRECIPITABLE WATER (KG M-2)
JJA, STD DEV
90
60
30
0
-30
-60
-90
-180
-120
-60
0
60
120
180
contour interval = 0.5

Figure E-24.

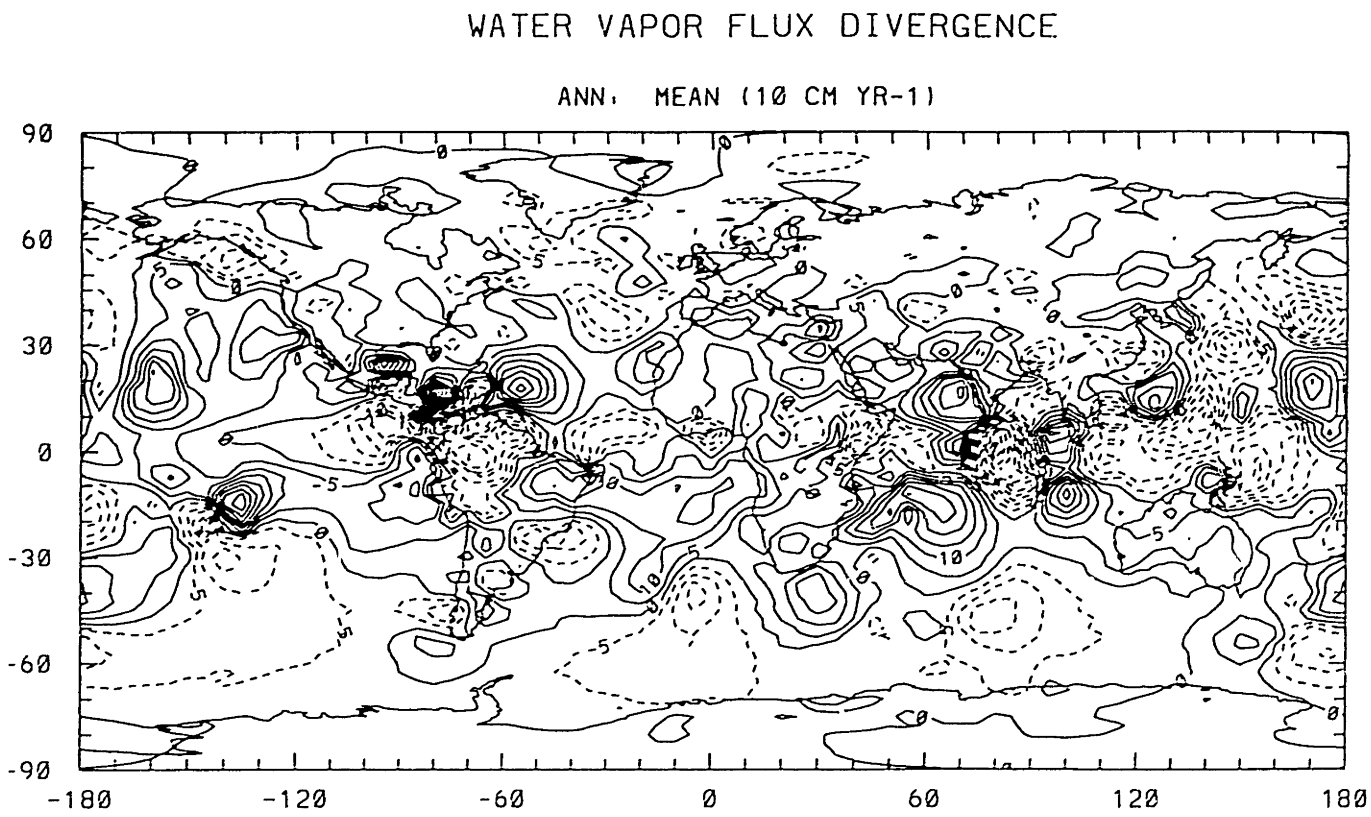
WATER VAPOR FLUX DIVERGENCE
ANN. MEAN (10 CM YR-1)
90
60
30
0
-30
-60
-90
-180
-120
-60
0
60
120
180
Contour interval = 5.
unsmoothed

Figure E-25.

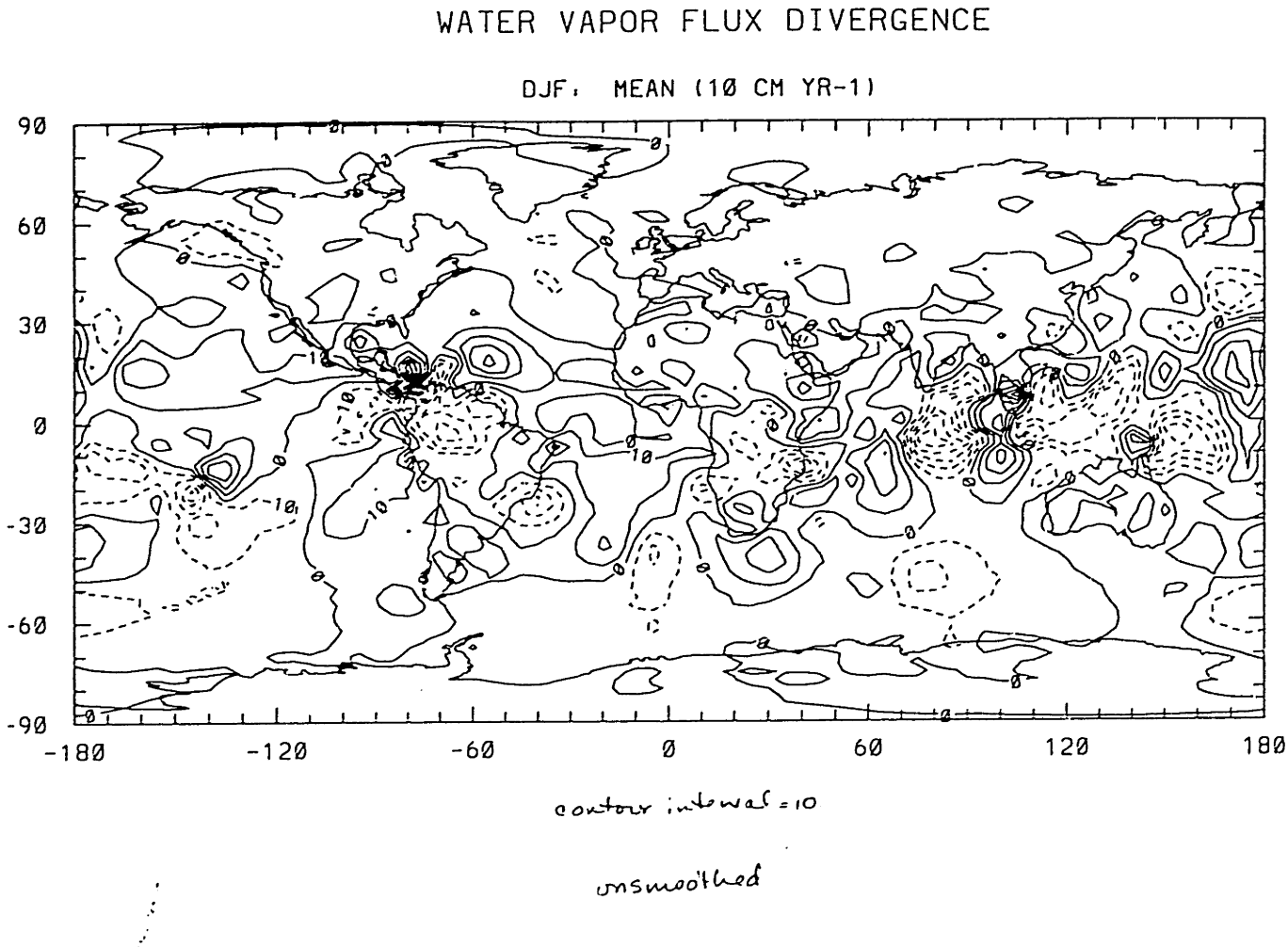
WATER VAPOR FLUX DIVERGENCE
DJF: MEAN (10 CM YR-1)
90
60
30
0
-30
-60
-90
-180
-120
-60
0
60
120
180
contour interval = 10
unsmoothed

Figure E-39.

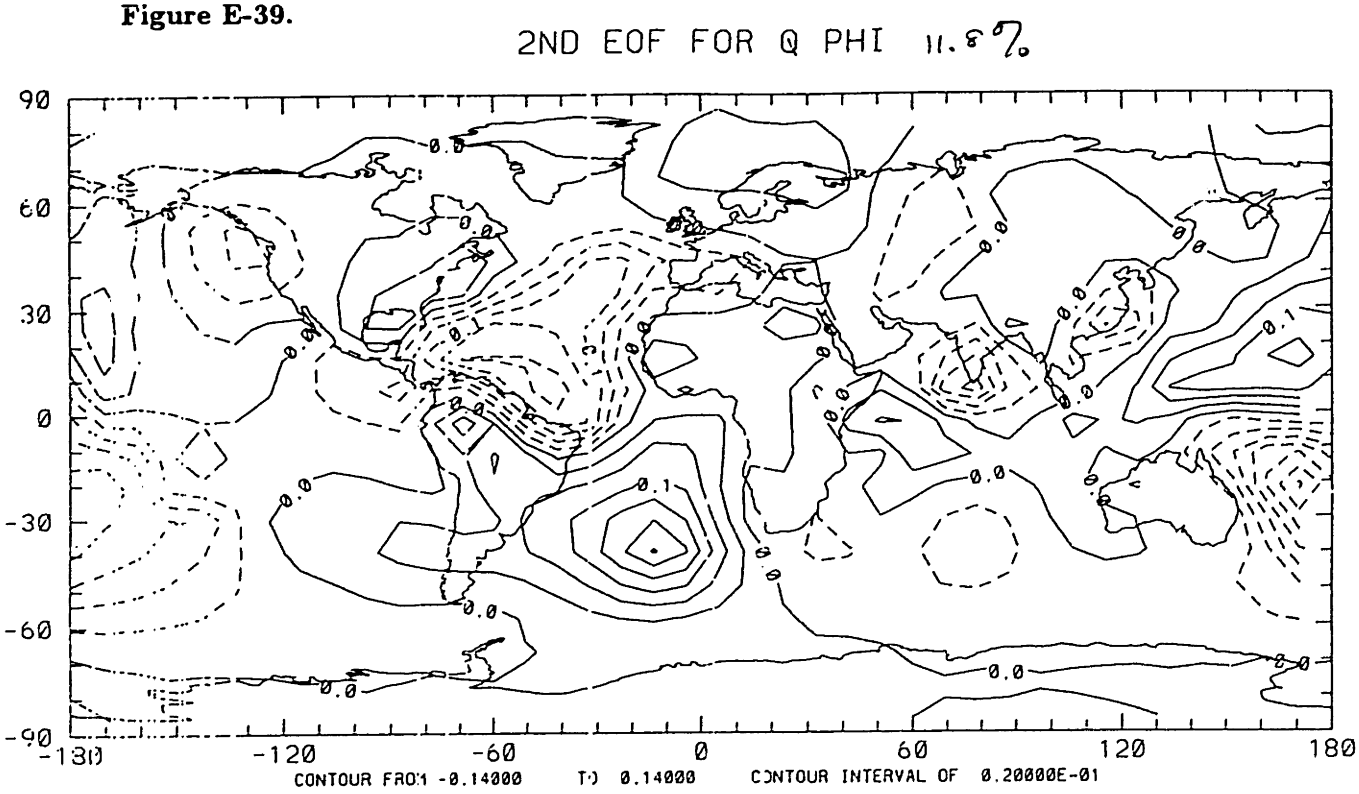
2ND EOF FOR Q PHI 11.8%
90
60
30
0
-30
-60
-90
-180
-120
-60
0
60
120
180
CONTOUR FROM -0.14000 TO 0.14000 CONTOUR INTERVAL OF 0.20000E-01

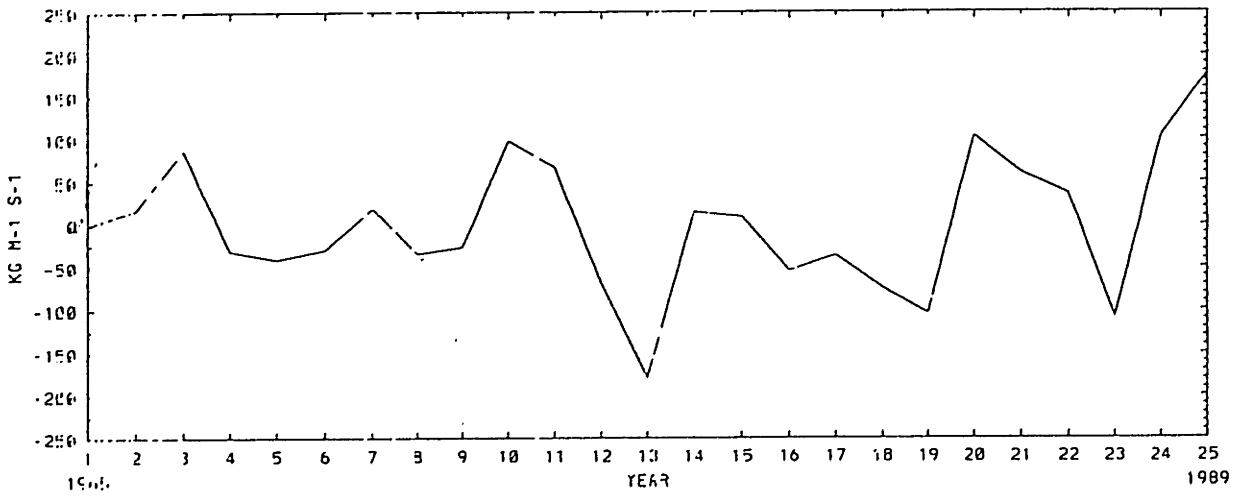
KG M-1 S-1
-50
-100
-150
-200
-250
1 2 3 4 5 6 7 8 9 10 11 12 13 14 15 16 17 18 19 20 21 22 23 24 25
YEAR
1989

Figure E-40.

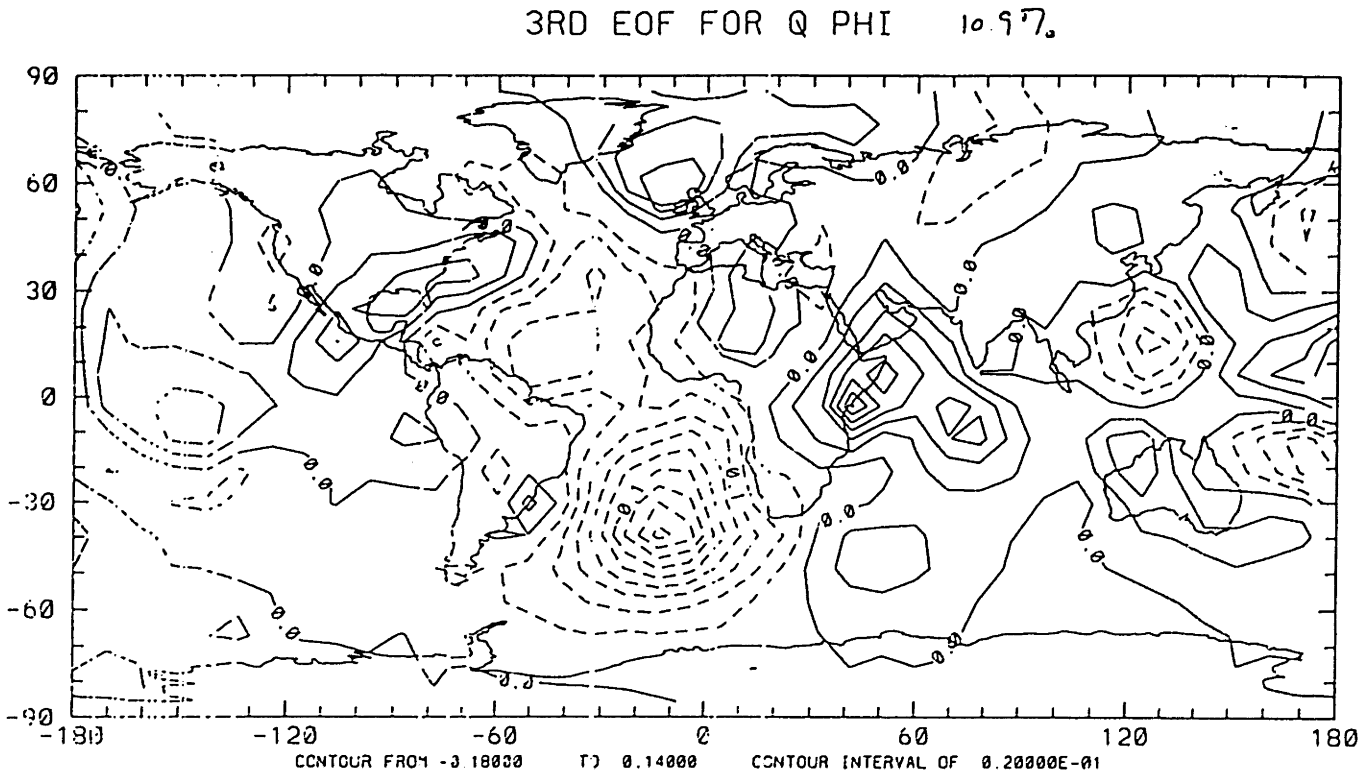
3RD EOF FOR Q PHI 10.9%
90
60
30
0
-30
-60
-90
-180
-120
-60
0
60
120
180
CONTOUR FROM -3.18000 TO 0.14000 CONTOUR INTERVAL OF 0.20000E-01

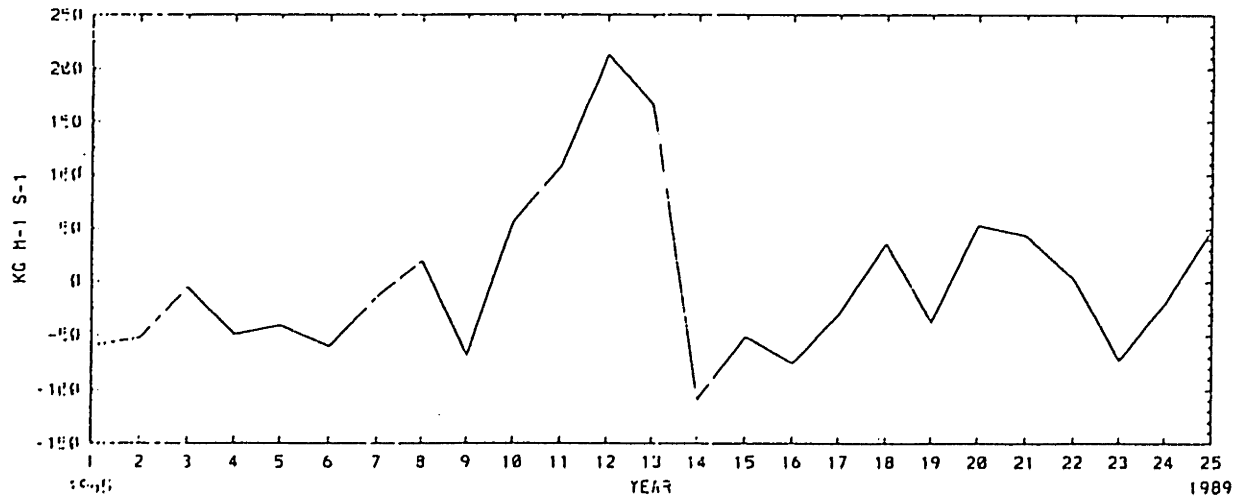
KG M-1 S-1
250
200
150
100
50
0
-50
-100
-150
1 2 3 4 5 6 7 8 9 10 11 12 13 14 15 16 17 18 19 20 21 22 23 24 25
YEAR
1989

REFERENCES

Baumgartner, A. and E. Reichel, 1975: The world water balance: mean annual global, continental and maritime precipitation, evaporation and run-off. Elsevier Scientific Pub. Co.

Broecker, W. S., T. H. Peng, J. Jouzel, and G. Russell, 1990: The magnitude of global fresh-water transports of importance to ocean circulation. *Climate Dyn.*, **4**: 73-79.

Bryan, F. and A. Oort, 1984: Seasonal variation of the global water balance based on aerological data. *J. Geoph. Res*, **89**:11,717-11,730.

Chen, T. C., J. Pfaendtner, and S. P. Weng, 1994: Aspects of the hydrological cycle of the ocean-atmosphere system. *J. Phys. Ocean.*, **24**: 1827-1833.

Dickson, R. R., and J. Brown, 1994: The production of North Atlantic Deep Water: sources, rates and pathways. *J. Geoph. Res.*, **99**:C6,12,319-12,341.

Elliot, W. P. and D. J. Gaffen, 1991: On the utility of radiosonde humidity archives for climate studies. *Bull Amer. Meteor. Soc.*, **72**:10 1507-1520.

Gaffen, D. J., T. P. Barnett, and W. P. Elliott, 1991: Space and time scales of global tropospheric moisture. *J. Climate*, **4**: 989-1008.

Gill, A. E., 1982: Atmosphere-Ocean Dynamics. Academics Press, 597.

GRDC, 1994: Hydrological Regimes of the 20 Largest Rivers of the World: A Compilation of the GRDC Database. Report No. 5. Global Runoff Data Centre, Federal Institute of Hydrology, 9.

Green, J. R. and D. Margerison, 1977: Statistical Treatment of Experimental Data. Elsevier Publishing, 296.

Hansen, J., 1987: Global trends of measured surface air temperature. *J. Geophys. Res.*, **92**: 13,345-13,372.

Karl, T. R., A. J. Koscielny and H. F. Diaz, 1982: Potential errors in the application of principal component (eigenvector) analysis to geophysical data. *J. Appl. Meteor.*, **21**: 1183-1186.

Larsen, R. J., and M.L.Marx, 1981: An Introduction to Mathematical Statistics and Applications. Prentice Hall, 425-428.

Levitus, S., 1982: Climatological atlas of the world ocean, NOAA Prof. Paper *13*.

Marotzke, J., and J. Willebrand, 1991: Multiple equilibria of the global thermohaline circulation. *J. Phys. Oceanogr.*, **21**: 1372-1385.

North, G. R., T. L. Bell, R. F. Cahalan, and F. J. Moeng, 1982: Sampling errors in the estimation of empirical orthogonal functions. *Mon. Wea. Rev.*, **110**: 699-706.

Oki, T., K. Musaki, K. Masuda and H. Matsuyama, 1993: Global runoff estimation by atmospheric

water balance using ECMWF dataset. *Macroscale Modeling of the Hydrosphere*, IAHS Publ. no. 214.

Oort, A. H., 1978: Adequacy of the rawinsonde network for global circulation studies tested through numerical model output. *Mon. Wea. Rev.*, **106**, 174-195.

Parker, D. E., and D. I. Cox, 1995: Towards a consistent climatological rawinsonde data-base. *Intl. Journ. of Climatology*, **15**: 473-496.

Peixoto, J. P., and A. H. Oort, 1992: Physics of Climate. American Institute of Physics, 70-90.

Preisendorfer, R. W., and T. P. Barnett, 1977: Significance tests for empirical orthogonal functions. *Fifth Conf. Probability and Statistics*, Las Vegas, Amer. Meteor. Soc., 167-172.

Salstein, D. A., R. Rosen and J. P. Peixoto, 1983: Modes of variability in annual hemispheric water vapor and transport fields. *J. Atmos. Sci.*, **40**: 788-803.

Sokolovskii, D. L. 1968: River Runoff: Theory and Analysis. Israel Program for Scientific Translations, 283-284.

Sun, De-Zheng and A.H. Oort, 1995: Humidity-Temperature Relationships in the Tropical Troposphere. *J. Climate*, **8**: 1974-1987.

Zauker, F., and W. S. Broecker, 1992: The influence of atmospheric moisture transport on the fresh water balance of the Atlantic drainage basin: general circulation model simulations and observations. *J. Geoph. Res.*, **97**: 2765-2773.

Zauker, F., T. M. Stocker and W. S. Broecker, 1994: Atmospheric freshwater fluxes and their effect on the global thermohaline circulation. *J. Geoph. Res.*, **99**:C6, 12,443-12,457.